Pulsed laser deposition of superconducting Sr_2RuO_4 thin-films and the role of crystallographic defects

Carla María Palomares García

Wolfson College, University of Cambridge

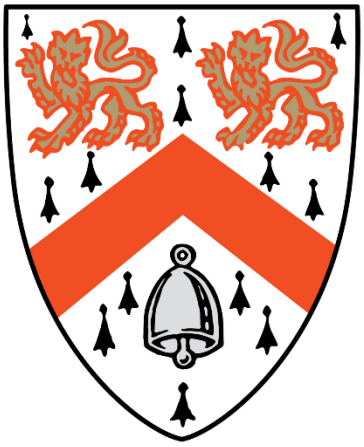

This thesis is submitted for the

Degree of Doctor of Philosophy

May 2020

This thesis is the result of my own work and includes nothing which is the outcome of work done in collaboration except as declared in the Preface and specified in the text. It is not substantially the same as any that I have submitted, or, is being concurrently submitted for a degree or diploma or other qualification at the University of Cambridge or any other University or similar institution except as declared in the Preface and specified in the text. I further state that no substantial part of my thesis has already been submitted, or, is being concurrently submitted for any such degree, diploma or other qualification at the University of Cambridge or any other University or similar institution except as declared in the Preface and specified in the text. It does not exceed the prescribed word limit for the relevant Degree Committee.

Carla María Palomares García

May 2020

Cambridge, UK

Pulsed laser deposition of superconducting Sr_2RuO_4 thin-films and the role of crystallographic defects

Sr_2RuO_4 (SRO_{214}) is a prototypical unconventional superconductor. However, since the discovery of superconductivity a quarter of a century ago, the symmetry of the bulk and surface superconducting states in single-crystal SRO_{214} remains highly controversial. Solving this problem is impeded by the fact that superconducting SRO_{214} is extremely challenging to achieve in thin-films as structural defects and impurities sensitively annihilate the superconducting state. Despite a handful of successful results on the growth of superconducting SRO_{214} thin-films by molecular beam epitaxy (MBE), reproducible growth by pulsed laser deposition (PLD) remains extremely challenging. In this thesis, we developed a protocol for the reliable growth of superconducting SRO_{214} thin-films by pulsed laser deposition and identify the type of structural defects that are responsible for destroying superconductivity.

We have systematically investigated the structure-electrical-properties relationship of epitaxial SRO_{214} thin-films grown by PLD on $(LaAlO_3)_{0.3}(Sr_2TaAlO_6)_{0.7}$ (LSAT). Growth parameters including temperature, substrate and target composition have been varied to understand their influence on the microstructure and electrical properties of SRO_{214}. We also investigated the presence of impurities and crystallographic defects using X-ray diffraction techniques in conjunction with electron microscopy to identify the underlying microstructural features that suppress superconductivity in SRO_{214} thin-films.

We demonstrate that, careful control of the starting material is essential to achieve superconductivity. By replacing the conventional SRO_{214} polycrystalline target with a single crystal of $Sr_3Ru_2O_7$ (SRO_{327}), we succeed in growing reproducible, high quality, superconducting SRO_{214} thin-films. By varying the SRO_{214} thickness, we observe the absence of superconductivity in films thinner than 50 nm (grown using a pulse frequency of 2 Hz). The suppression of superconductivity in thinner films is found to correlate to in-plane misorientation and mosaic twist, caused by in-plane screw dislocations that form close to the SRO_{214}/LSAT interface.

In conclusion, this work provides the first reliable pulsed laser deposition protocol for superconducting SRO_{214} thin-films. The results are of immediate interest to the superconducting and magnetism communities and form the foundation for a whole new spectrum of proximity experiments involving unconventional superconducting symmetries.

Carla María Palomares García

Dedicated to my parents, my brother

and to my soulmate Edgaras

Acknowledgements

I would like to express my gratitude to my supervisor Professor Jason Robinson, who gave me this amazing opportunity and tirelessly guided, advised and encouraged me all the way through the research project with immense optimism, teaching me that everything can be learnt.

My appreciation also extends to the colleagues who have been following the project closer and actively participated in the review of the scientific article since their contribution was essential. My special appreciation goes to Angelo Di Bernardo, for mentoring me step-by-step during my PhD, taking great care and making the difficult times in the laboratory enjoyable. Mary Vickers, for the assistance, suggestions, and for teaching me about X-ray diffraction with a big smile, full of energy and enthusiasm. Graham Kimbell for the great support during the thesis, feedback and fruitful scientific discussions. Fabien Massabuau for contributing with TEM measurements and sharing his knowledge with immense joy.

From my research visit to Kyoto University (Japan), I am grateful to Professor Maeno and his team for generously sharing their knowledge, especially to Yasui Yuuki, who greatly contributed on the first steps of this research helping with the thin film fabrication and characterization, Takuto Miyoshi, Shingo Yonezawa, and also to Keiko Takamiya for her warm welcome in Japan. As well, to Ivan Kostilev, Mohamed Oudah, Chanchal Sow and Igor Markovic for making my trip to Japan an adventure. From my research visit to IBS-CESS (Republic of Korea), I would like to thank Professor Tae Won Noh, my trainers and colleagues Bongju Kim, Han-gyeol Lee, Jinkwon Kim for making this study possible, and to Eun-Kyo Ko for the help in the laboratory and the great time we spent together enjoying the Korean culture. Also, to my colleagues Saikat Das and Lingfei Wang.

To my colleagues at the Department of Materials Science in Cambridge, for the good times in the laboratory, tea times and trips together, because without you it would not have been the same: Anand Srivastava, Bashi (Bhaskaran Nair), Ben Stoddart-Stones, Bence Börcsök, Chang-Min Lee, Harry Bradshaw, James Devine, John Feighan, Juliet Thompson, Lana Lee, Lauren McKenzie-Sell, Linde Olde, Ravi Raninga, Salvatore Mesoraca, Samer Kurdi, Thomas Higgs, Willheim Hüttenes, and postdocs: Enric Stern, Guilliaume Nataf, Jonathan Calahorra, Juan M. Bermúdez, Sachio Komori, Shabaz Anwar, Tuhin Subhra, Weiwei Li. Also to Jimmy Campbell, Noel Glaenzer, Fermando Roberto and Fabio Di Gioacchino. Especially, I would like to thank Nadia Stelmashenko for her great support in- and outside the laboratory.

I would like to acknowledge the financial support provided by the EPSRC and the Oxide Superspin Network as well as the academic insights provided by their members, particularly to Antonio Vecchione and Paola Gentile.

To my parents and brother, my soulmate Edgaras Šmigelskis and friends; Mario Amado and family, Catalina Taltavull, Lucas, Maria Frías, Luis Olangua and Jane Dukes; for the unconditional support, listening and giving me always words of encouragement.

To the great researchers and friends that I met on the way and greatly influenced my career path: Prof. Alfredo Álvarez and Dr J. M. Ceballos and Prof. Jose Luis Vicent, with whom my curiosity about superconductivity started, Dr Alberto Palomares, Dr Miguel Tardío, Prof. Juan Enrique Muñoz Santiuste, Dr Ricardo Domínguez Reyes, Dr Pilar Leret, Dr Julián Jiménez Reinosa, Dr Aída Serrano, Dr Alberto Moure, Isabel Salmeán, Carlos Fernández and Prof. Akira Fujiwara, thank you for inspiring and motivating me to do research.

For the viva, I would like to extend my appreciation to Prof. Caterina Ducati and Dr Anna Palau for their valuable feedback and comments on my research.

This thesis is written in memory of my friend Celso Mesón, a reference who I always look up to, whose curious mind made him achieve great outcomes. You will be always an inspiration.

Table of Contents

List of Figures

List of Tables

Nomenclature

List of Greek symbols

α	Heater angle in PLD system
β	Rotation angle of PLD target
Δ	Energy gap
ε	Strain (homogeneous)
θ	Theta angle in X-ray diffraction
λ	X-ray wavelength
λ_{GL}	Ginzburg-Landau penetration depth
μ_0	Vacuum permeability
$\mu\varepsilon$	Microstrain (or inhomogeneous strain)
ξ	Superconducting coherence length
ρ	Resistivity
ρ_0	Residual resistivity
σ_i	Spin pairing symmetry
$\chi(k_1, k_2)$	Orbital wavefunction
χ	Diamagnetic susceptibility
χ_{offset}	Chi angle in X-ray diffraction
ψ	Superconducting order parameter
ω	Omega angle in X-ray diffraction
$\hbar$	Reduced Plank constant
υ_F	Electron velocity at the Fermi surface
τ	Electron scattering time
Φ	Angle between crystallographic planes
Φ	Superconductor flux quantum

List of Roman symbols

a	In-plane lattice parameter of SRO_{214}
b	In-plane lattice parameter of SRO_{214}
$\vec{b}$	Burgers vector
C	Out-of-plane lattice parameter of SRO_{214}
D	Interplanar distance

e	Electron charge
$\vec{g}$	Diffracted beam vector
h	Plank constant
H_c	Superconducting critical field
H_{c1}	Superconducting upper critical field
H_{c2}	Superconducting lower critical field
I_c	Superconducting critical current
K	Crystallite shape factor in Scherrer equation
k_i	Orbital pairing symmetry
l	Electron mean free path
L	Orbital angular momentum
m	Magnetic moment
m_e	Electron mass
n_s	Density of electrons
P	Pressure
ppm	Part per million
R	Resistance
S	Total spin
S	Modulus of the scattering vector
T	Temperature
t	Thickness
T_c	Superconducting critical temperature
T_{Curie}	Curie transition Temperature
$\vec{u}$	Dislocation line vector
V_1	Speed of the seed
V_2	Speed of the feed
m	Slope in a linear equation

List of Abbreviations

AFM	Atomic force microscopy
BCS	Bardeen-Cooper-Schrieffer theory
EDX	Energy-dispersive X-ray spectroscopy
FWHM	Full width half maximum
FZ	Floating zone method
GL	Ginzburg Landau

ICDD	International centre for diffraction data
IPA	Isopropyl alcohol
LSAT	$(LaAlO_3)_{0.3}(Sr_2TaAlO_6)_{0.7}$
MBE	Molecular beam epitaxy
NMR	Nuclear magnetic resonance
OSS	Oxide Superspin
PD	Pressure x Distance law
PLD	Pulsed laser deposition
RHEED	Reflection high-energy electron diffraction
RLM	Reciprocal lattice maps
RLP	Reciprocal lattice points
RRR	Residual resistivity ratio
SEM	Scanning electron microscopy
SPIN	Superconducting and other innovative materials and device institute
SRO_{113}	$SrRuO_3$
SRO_{214}	Sr_2RuO_4
SRO_{327}	$Sr_3Ru_2O_7$
SRTO	$Sr_2Ru_{0.98}Ti_{0.02}O_4$
STO_{214}	Sr_2TiO_4
TEM	Transmission electron microscopy
TRS	Time-reversal symmetry
UHV	Ultra-high vacuum
VSM-SQUID	Vibrating sample magnetometer - Superconducting quantum interference device
XRD	X-ray diffraction
YBCO	$YBa_2Cu_3O_7$
μSR	Muon spin relaxation

Introduction

The discovery of superconductivity in Sr_2RuO_4 (SRO_{214})[1] brought about extensive research[2–5] aimed at understanding the nature of the superconducting state including the underlying superconducting symmetry. SRO_{214} and oxide high-temperature superconductors or cuprates are broadly defined as being unconventional superconductors. However, despite the similarities that SRO_{214} shares with the cuprates, it has a dramatically lower critical temperature (≈ 1.5 K)[6]. Additionally, SRO_{214} is likely to have a p-wave symmetry, close to the superfluid[7] He^3, with the Cooper pairs in a spin-triplet state with parallel aligned spins.

Unlike spin-singlet supercurrents associated with s-wave superconductors such as Nb or Al, spin-triplet supercurrents carry a net spin in addition to charge. Large efforts have been undertaken to artificially generate spin-triplet Cooper pairs from spin-singlet superconductors via proximity effects[8]. The fact that SRO_{214} is an intrinsic spin-triplet superconductor makes it an attractive material for potential applications in quantum-based spintronic devices. However, research into applications is at a very early stage with (significant) questions on the basic science SRO_{214} still unanswered.

Before starting this thesis, the majority of studies on the superconducting symmetry of SRO_{214} were limited to single crystal-based devices, which are restricted by dimension, the presence of impurities or defects that suppress the superconducting transition[6,9], and reproducibility issues[10]. To develop a full understanding of the superconducting properties of SRO_{214}, it is essential to be able to fabricate devices based on thin-films.

The fabrication of superconducting thin-films of SRO_{214} has remained a major challenge since the discovery of superconductivity in single crystals over twenty years ago. The main difficulty is based on the requirement to deposit ultra-high quality thin-films with no traces of impurities or structural defects that easily annihilate the superconducting state.

This Ph.D. research project aims to provide the scientific community with a reliable method to grow superconducting SRO_{214} thin-films by pulsed laser deposition. In this thesis, I outline a reproducible growth protocol for thin-film SRO_{214} that enables device fabrication for further studies, which will help disentangle the superconducting properties of this material and lead to the discovery of new science.

The work has been carried out with the support of the international network “Oxide Superspin” or OSS, created to explore unconventional superconductivity, and the outputs are

the result of a close collaboration between myself and Professor Jason Robinson with Professor Yoshiteru Maeno at Kyoto University (Japan), Professor Tae Won Noh at the Seoul National University (Republic of Korea) and Professor Antonio Vecchione from Consiglio Nazionale delle Ricerche, SPIN (Italy).

This Ph.D. thesis is structured into the following 5 chapters:

- **Chapter 1**: Introduction of the fundamentals of superconductivity, followed by a description of SRO_{214} and a literature review highlighting experiments to understand the superconducting properties and research on the fabrication of thin-films.

- **Chapter 2**: Provides descriptions of the techniques and methods applied to grow and characterize the electrical and structural properties of SRO_{214} thin-films in this thesis.

- **Chapter 3**: First results on the optimization of the growth of metallic SRO_{214} thin-films by pulsed laser deposition system (PLD).

- **Chapter 4**: PLD optimisation of superconducting SRO_{214} thin-films by ablation from a single-crystalline target and the use of low angle miscut LSAT substrates.

- **Chapter 5:** Thickness-dependence of superconductivity in SRO_{214} thin-films and investigation of potential impurities and crystallographic defects that suppress superconductivity. Identification of in-plane mosaic twist as the key defect responsible for the suppression of superconductivity in SRO_{214}.

The outcomes of this research project are published in the reference below, which is included at the end of this thesis in the section **Appendix**.

Garcia, C. M. P. *et al*. Pair suppression caused by mosaic-twist defects in superconducting Sr_2RuO_4 thin-films prepared using pulsed laser deposition. Communication Materials **1**, 23 (2020) (Nature Publishing Group).

Chapter 1

Literature review

1.1 Principles of superconductivity

A superconducting material is characterized by having zero electrical resistance when cooled down below a critical temperature, T_c. In 1911, H. K. Onnes[11] discovered the first superconductor when lowering the temperature of a Hg wire below 4.2 K and observed a significant drop in resistance (down to the system sensitivity). Since then, there have been large efforts to understand superconductivity and find new superconducting materials. In 1986 a new family of superconductors with a T_c above 77 K (boiling point of liquid N_2) was discovered. These were named "High-T_c superconductors" or "cuprates" because their crystallographic structures are based on CuO, and they rapidly became of interest for technological applications in electricity transmission, power storage or medicine.

Despite over a century of research on superconductivity, we still cannot predict which materials could potentially show a superconducting transition and fabricate them by design. However, it is known that it is possible to modify the electronic properties of some materials and induce superconductivity with pressure[12–14].

In addition to the critical temperature, superconducting materials are limited by a critical field, H_c, and critical current, I_c. When the T_c, H_c, or I_c are exceeded, the normal state is recovered (**Figure 1.1a**). The superconducting state is defined by the Meissner effect, in which the material becomes a perfect diamagnet expelling a magnetic field. There are two types of

superconductors depending on how the transition from the normal state to the superconducting state occurs based on H_c: "type I" have a direct transition, and the Meissner effect can be directly observed below H_c; in contrast, "type II" have a mixed state between the normal and superconducting states, which is determined by two different critical fields, $H_{c1,}$ and H_{c2}, known as the upper and lower critical fields, respectively. The mixed state is characterized by vortices with metallic core where the magnetic field can penetrate, and by superconducting regions in their surroundings where a magnetic field is expelled (**Figure 1.1b**).

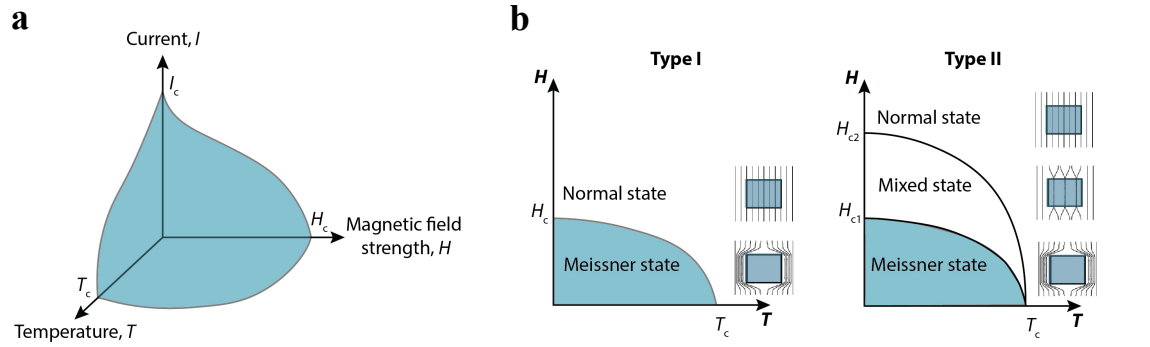

Figure 1.1 Critical parameters of superconductors. **a,** Schematic plots showing the superconducting space (inside the blue volume) delimited by the critical values of temperature, current and magnetic field. **b,** Magnetic field versus temperature diagram for type I and II superconductors, with a schematic diagram of the magnetic field interaction with the superconductor.

1.1.1 Bardeen-Cooper-Schrieffer theory

The microscopic theory of superconductivity was developed by Bardeen, Cooper, and Schrieffer, often named the "BCS theory of superconductivity", to explain "conventional" superconductors, but not the High-T_c materials which are "unconventional" superconductors (described later).

In the BCS theory, pairs of electrons near the Fermi surface form a bound state of "Cooper pairs" which interact via phonons: when an electron drifts through the crystal at zero temperature it briefly displaces an ion that will generate a phonon when returning to its original position. When this phonon interacts with a second electron, it lowers its energy through the deformation created. The second electron then emits a phonon that interacts with the first electron, thus creating a connection that brings two the electrons to a lower energy state (**Figure 1.2a,b**). This lower energy state compared to two unpaired electrons creates an energy gap, Δ, between the superconducting and the normal state, corresponding to the binding energy of the Cooper pair.[15]

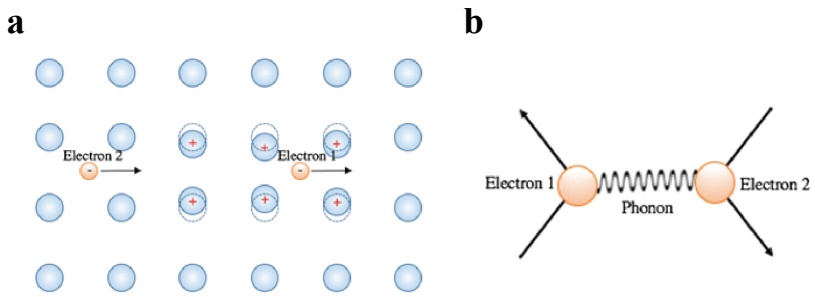

Figure 1.2 Electron interaction via phonons. a, Schematic illustration showing the displacement of the crystal lattice due to passing electrons within a superconductor. **b,** Feynman diagram of a Cooper pair.

1.1.2 Ginzburg Landau parameters

The Ginzburg-Landau (GL) theory provides a thermodynamic point of view of the superconducting phase transition. It suggests that superconductors, like ferromagnets, have an ordered phase with a symmetry change below T_c (or equivalently T_{Curie} in a ferromagnet). They proposed the existence of an order parameter, ψ, that defines the superconducting state in the same way that magnetization defines the order parameter for a ferromagnet, in which a spontaneous moment occurs below the Curie temperature, T_{Curie}. Below T_c, ψ is zero.[16]

From the GL theory, two important parameters describe superconductivity near T_c:

- the Coherence length, ξ_{GL}, which corresponds to the distance from the surface at which ψ recovers bulk values (**Figure 1.3a**) and can be calculated following the equation:

$$\xi_{GL}(T) = \left(\frac{\hbar^2}{2m_e|a(T)|}\right)^{1/2} \qquad \textbf{1.1}$$

  where a is a temperature-dependent coefficient proportional to $(T - T_c)/T_c$, $2m_e$ is the total mass of a Cooper pair and $\hbar$ is the reduced plank constant ($\hbar = h/2\pi$).

- The penetration depth, λ_{GL}, is the distance from the surface where an external magnetic field decays exponentially (**Figure 1.3b**) and it is given by:

$$\lambda_{GL} = \left(\frac{m_e}{\mu_0 n_s e^2}\right) \qquad \textbf{1.2}$$

  where n_s is the density of electrons that belongs to the Cooper pair, e is the electron charge, and μ_0 corresponds to the vacuum permeability.

The connection between GL and BCS theory was demonstrated by Gor'kov, showing that ψ corresponds to Δ and $|\psi^2| = n_s$ to the density of BCS Cooper pairs. The ratio $k = \lambda/\xi$ is known as the GL parameter and divides superconductors in type I for those with $0 < k < 1\sqrt{2}$, and type II for $k > \sqrt{2}$.

Additionally, there is another parameter relevant for the superconductivity of some materials in the presence of impurities known as the mean free path, l, which is defined as the average distance without collisions of electrons (**Figure 1.3c**) and it is given by:

$$l = v_F \tau \qquad \textbf{1.3}$$

where v_F is the electron band velocity at the Fermi surface, and τ is the electron scattering time.

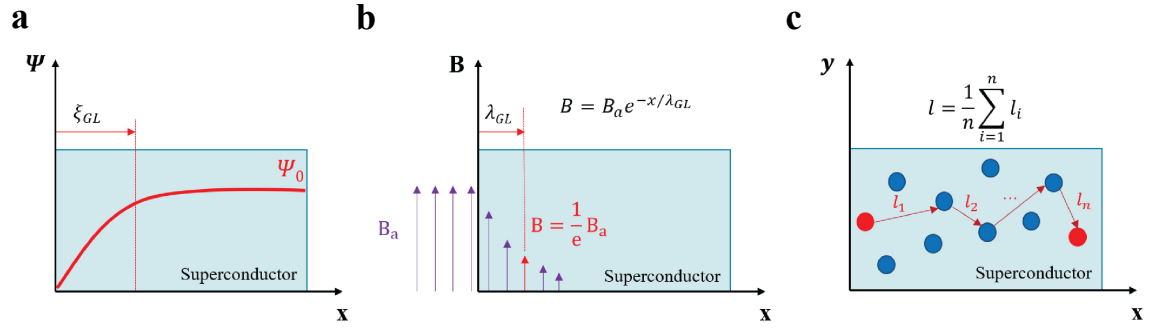

Figure 1.3 Schematic representations of the characteristic properties of superconductors. a,b, Ginzburg-Landau parameters: superconducting coherence length (**a**) and penetration depth (**b**). **c,** Mean free path.

1.1.3 Unconventional superconductivity

In Cooper pairs, the order parameter, ψ, is given by the contribution of the orbital pairing symmetry (k_i) and the spin (σ_i):

$$|\psi\rangle = \chi(k_1, k_2)|\sigma_1, \sigma_2\rangle \qquad \textbf{1.4}$$

According to the spin of the electrons of the Cooper pair, the pairing can be in a spin-singlet state, when the total spin is S = 0, or a spin-triplet state when the total spin is S = 1. Additionally, since electrons are fermions, they have to fulfil the anticommuting property of the Pauli exclusion principle. Therefore, the antisymmetric spin-singlet state (S = 0) has to be complemented by a symmetric orbital wavefunction (χ); this is an orbital angular momentum: L = 0 (s-wave), L = 2 (d-wave), etc. Whereas the symmetric spin singlet (S = 1) has to be accompanied by an antisymmetric orbital wavefunction, with L = 1 (p-wave), L = 3 (f-wave), etc (see **Table 1.1**).[17]

We use the term "conventional" to refer to the superconductors with s-wave pairing symmetry that have an isotropic energy gap in momentum space. They are called "conventional" because the electron interaction is well described by the BCS theory and the first superconductors discovered during the first 60 years belong to this group.

In contrast, the discovery of superfluidity in He^3 in 1974[18] with a p-wave symmetry that could not be described by BCS theory, marked the beginning of "unconventional" superconductivity. The term "unconventional" is used for any non-s-wave superconductor

described by an anisotropic energy gap in momentum space. One of the key characteristics is its sensitivity to impurities since successive electron scattering averages the superconducting gap, leading to a suppression of the superconductivity (**Figure 1.4**).

Table 1.1 Classification of superconductors attending to their pairing symmetry.

Name	Momentum, κ			Spin state, σ	Examples
	Orbital angular momentum, L		Parity of spatial part		
Conventional	0	Even	s-wave	Singlet	Nb
Unconventional	1	Odd	p-wave	Triplet	UPt_3 Sr_2RuO_4
	2	Even	d-wave	Singlet	YBa_2Cu_3O

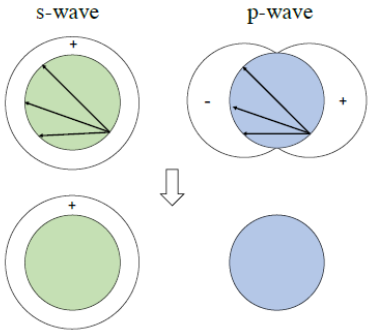

Figure 1.4 Effect of the elastic scattering in the superconducting order parameter. Representation of the superconducting gap in the momentum space located around the Fermi surface (green/blue) when elastic scattering (arrows) occur in an isotropic s-wave (conventional) and an anisotropic p-wave (unconventional) superconductor. (Adapted from[19]).

1.1.4 Triplet pairing

Virtually all known superconductors (conventional and unconventional) have a spin-singlet pairing state. There are only a few known examples of spin-triplet superconductors, including superfluid He^3, the uranium-based compounds UPt_3 and UGe_2, and potentially Sr_2RuO_4 (SRO_{214}).

Additionally, there is research focused on engineering spin-triplet Cooper pairs using spin-singlet superconductors. This is possible due to the long-range proximity effect that occurs at the interface between an s-wave superconductor and a ferromagnet (S/F). In the case of S/F junctions, long-range (spin-aligned) triplet pairs are created and injected into the ferromagnet when there is an inhomogeneous magnetization state at the S/F interfaces such as a domain

wall or misaligned magnetic moments. In the absence of an inhomogeneity, short-range spin triplets are created but these rapidly decay in the ferromagnet over a length scale of a few nanometres matching the decay envelope of singlet pairs (**Figure 1.5**)[8,20].

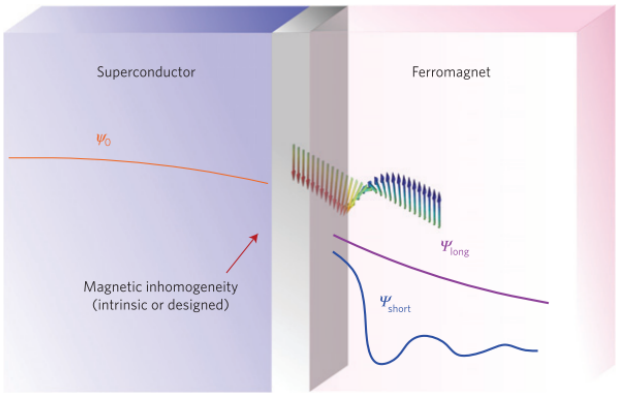

Figure 1.5 Schematic illustration of the long (short) range spin-triplet formation from a superconductor/ferromagnet (S/F) heterostructure with (without) a magnetic inhomogeneity. In the schematic, $\boldsymbol{\psi_0}$ represents the spin-singlet current from a conventional superconductor, $\boldsymbol{\psi}_{\text{long}}$ the long-range spin-triplet current and $\boldsymbol{\psi}_{\text{short}}$, the short-range spin-triplet current. (From[8]).

1.2 Strontium ruthenate bulk

Since the discovery of its superconductivity in 1994 by Prof. Maeno *et al.*[1], strontium ruthenate (Sr_2RuO_4) has been the subject of numerous studies trying to explain its unconventional properties[3,4,17,19,21,22]. Because of the superconducting transition sensitivity to impurities and defects, high-quality single crystals in the clean limit ($l >> \xi$) have been achieved in the last 20 years to be used as samples for further studies[23]. However, there is still lack a complete understanding of its superconducting state and some of the most recent experiments are inconclusive or contradictory[5].

In the upcoming sections, the normal- and superconducting-state properties of Sr_2RuO_4 will be introduced, which we refer to as SRO_{214} for simplification, and a summary about what it is known until today regarding its unconventional properties.

1.2.1 Normal-state properties

These properties are obtained above the superconducting transition, T_c, or above the upper magnetic field, H_{c2} in single crystals grown by the floating zone method (described in detail in **Chapter 3**).

The crystal structure corresponds to a body-centred tetragonal unit cell of the K_2NiF_4-type structure, consisting of alternating layers of the rocking salt SrO and the perovskite $SrRuO_3$.

There is no phase transition associated with temperature and the lattice parameters do not suffer large variations (see **Table 1.2**).

Table 1.2 Lattice parameters in- and -out-of-plane of SRO_{214} single crystals measured at different temperatures. Data from powder diffraction from PDF 01-082-1096 (ICDD, 2016)[24].

	10 K	**300 K**
$a = b$ (Å)	3.8635(8)	3.8730(3)
c (Å)	12.7155(4)	12.7323(9)

SRO_{214} is a layered perovskite, similar to the high-temperature superconductors, where the Cu layers are replaced by RuO_2 planes. In the Ruddlesden-Popper series, expressed as $Sr_{n+1}Ru_nO_{3n+1}$, SRO_{214} has one layer of RuO_2 planes (n = 1) and it is a paramagnet with spin fluctuations, whereas higher values in n lead to an increased ferromagnetic behaviour. For instance, SRO_{327} (n = 2) has a ferromagnetic transition below 70 K and under pressure[25], and SRO_{113} ($n \rightarrow \infty$) is ferromagnetic[26] below 160 K.

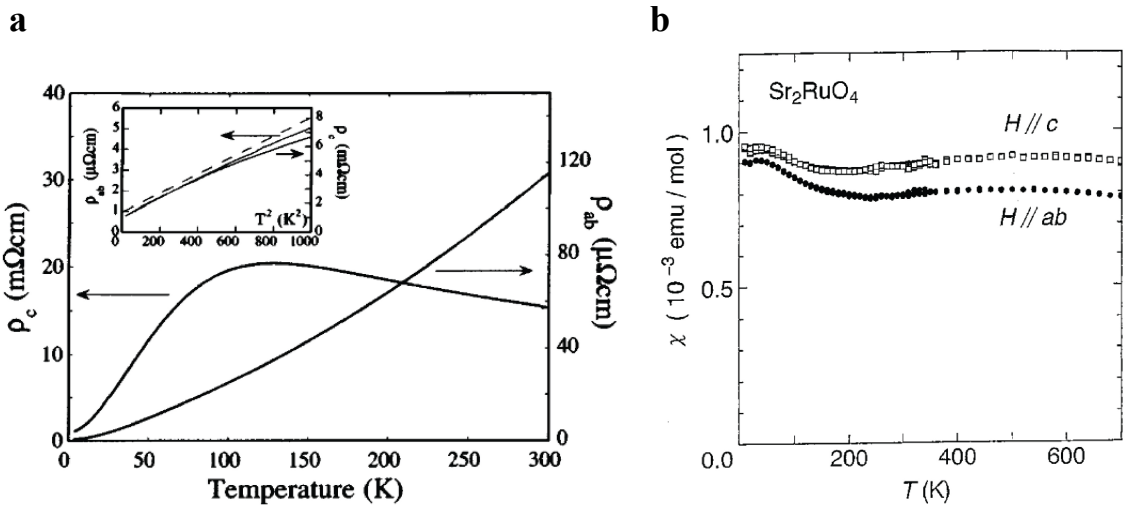

Figure 1.6 Normal state resistivity and susceptibility characteristics of SRO_{214}. a, Resistivity versus temperature in- (ρ_{ab}) and out-of-plane (ρ_c) with the inset the T^2 response at low T (dotted line). **b,** Susceptibility versus temperature with an in- ($H \parallel ab$) and out-of-plane ($H \parallel c$) applied field of 1 T. (From [19]).

Regarding the electrical properties at high temperature ($T > 4$ K), the resistivity dependence with the temperature is anisotropic depending on the direction of current with the RuO_2 planes. The in-plane resistivity, ρ_{ab}, is metallic down to T_c and the out-of-plane resistivity, ρ_c, initially increases when cooling down the crystals from room temperature, and when it reaches a maximum at 130 K starts decreasing. Below 20 K, both signals follow a T^2 dependence. The resistivity ratio (ρ_{ab}/ρ_c), ranges from 220 (290 K) to 850 (2 K) (**Figure 1.6a**).

However, despite the anisotropy reported on the electrical properties, the magnetic susceptibility, χ, is isotropic regardless of the direction of the applied field up to 1 T (**Figure 1.6b**).

1.2.2 Superconducting-state properties

Superconductivity in single crystals was first reported by Maeno *et al.*[1] with a T_c at 0.93 K without the requirement for carrier doping. However, with further development of the growth conditions, crystals approaching the clean limit ($l >> \xi$) have an increased T_c of up to 1.5 K.[6]

Large similarities have been found with high-T_c superconductors i.e. the nearly equal crystallographic structure to $La_{2-x}Ba_xCuO_4$ or being oxides with conduction occurring in partially filled d-band (Sr or Cu). However, there is a clear difference in the T_c between these materials since SRO_{214} has a low superconducting transition in comparison, which is associated with a low residual resistivity, making it closer to superfluid He^3.

The resistivity of SRO_{214} shows anisotropy at low temperature ($T < 4$ K) depending on the direction of the applied current (in-, ρ_{ab}, or out-of-plane, ρ_c) with a difference of three orders of magnitude (see **Figure 1.7a**). The a.c. susceptibility measurement, χ, shows a strong diamagnetic signal associated with the Meissner effect below 1 K when a magnetic field is applied parallel to the *c*-axis (see **Figure 1.7b**)[1]. The main GL parameters are summarized in (**Table 1.3**).

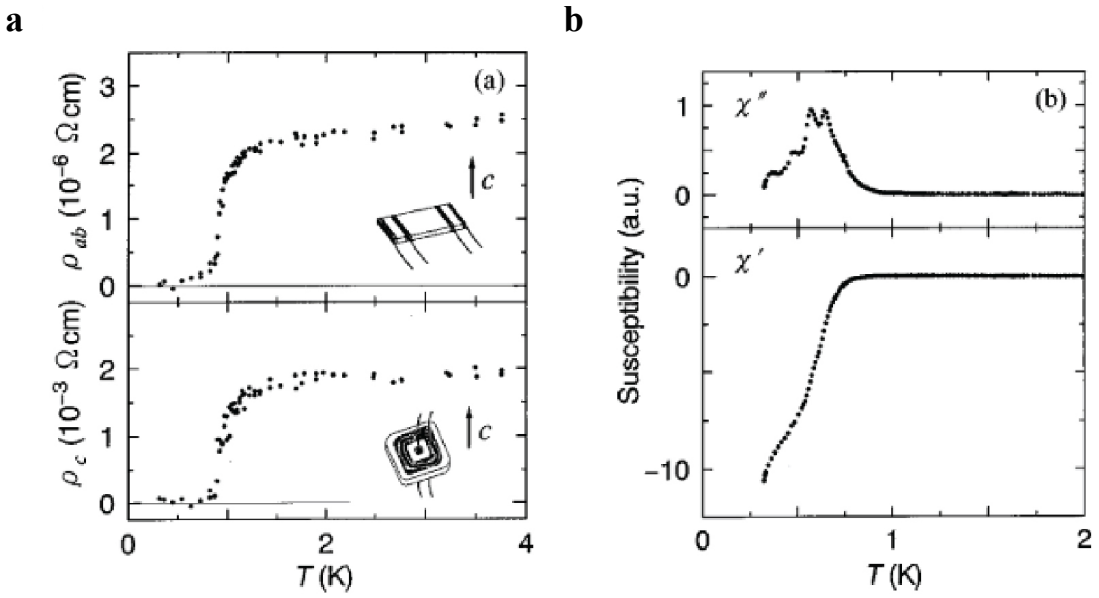

Figure 1.7 Electrical and magnetic characterization of an SRO_{214} single crystal at low temperature. a, Resistivity as a function of temperature in- (top plot) and out-of-plane (bottom plot) indicating the configuration of the electrodes (inset). **b,** The a.c susceptibility as a function of temperature with an applied out-of-plane field of 0.67 Oe at 1 Hz, separating the imaginary component, χ'', (top plot) from the real component, χ', (bottom plot). (From [1]).

Table 1.3 Superconducting Ginzburg-Landau parameters experimentally obtained from SRO_{214} single crystals. (From [19]).

Description	Abbreviation		In-plane (*ab*)	Out-of-plane (*c*)
Critical temperature	T_c (K)	1.5		
Upper critical field	$\mu_0 Hc_2$ (T)	-	1.5	0.075
Lower critical field	$\mu_0 Hc$ (T)	0.023	-	-
Coherence length	$\xi(0)$ (Å)	-	660	33
Penetration depth	$\lambda(0)$ (Å)		1900	3.0×10^4
Ginzburg–Landau parameter	$\kappa(0) = \lambda/\xi$	-	2.6	46
Anisotropy parameter	$\xi_{ab}(0)/\xi_c(0)$	20	-	-

1.2.3 Superconducting pairing symmetry

Similar to the high-T_c superconductors (such as YBCO), some studies support that SRO_{214} belongs to the group of unconventional superconductors since its phase in the momentum space is anisotropic.

In an unconventional superconductor, sufficient electron scattering cancels out the order parameter and leads to the complete suppression of the superconductivity[6]. The sensitivity found on the T_c of SRO_{214} crystals to magnetic and non-magnetic impurities that act as pair-breakers scatterers points at an unconventional pairing symmetry and sets the limit to observe superconductivity when the electron mean free path falls below the superconducting coherence length[6] (see **Chapter 5**).

Some direct experiments that support the chiral p-wave symmetry (even parity) are based on the time-reversal symmetry, TRS, breaking below T_c from the increase of the muon spin relaxation, μSR, rate[27], the observation of polar Kerr rotation[28] from magneto-optic measurements at low T or the temperature dependence of the specific heat coeficient[29]. Additional results that support the spin-triplet pairing state are extracted from nuclear magnetic resonance, NMR, Knight shift[30,31] (inelastic neutron scattering), and polarized neutron scattering[32], which measure a constant spin susceptibility in all directions (in- and out-of-plane[33]) of SRO_{214} below T_c. However, the invariability of the susceptibility rejects the possibility of chiral p-wave symmetry.

Contrary to an initial publication previously referred, there is a very recent report on NMR that shows a decay in the Knight shift measurements when lower excitation power is applied[34]. This is also supported by recent polarized neutron scattering measurements[35] which also contradicts previous results and supports a d-wave or helical p-wave symmetry on SRO_{214}.

Understanding the pairing symmetry of SRO_{214} will help to the development of unconventional superconductivity, finding new materials and looking for its applications.

1.2.4 Proximity effects

Experimental results indicate that SRO_{214} is an intrinsic triplet superconductor. The fact that SRO_{214} may have a triplet pairing symmetry suggests that the current carries a net spin and so, it could transfer spin-information without heat losses, becoming an ideal candidate for applications in spin-based superconducting memory devices with the additional advantage over normal state spintronics through superconducting phase coherence[8]. However, given the complications in the determination of its order parameter, we still rely on experiments involving phase-sensitive measurements, such as Josephson junctions, and theoretical predictions[36] to provide answers and complete the puzzle of the superconductivity on SRO_{214}.

For instance, an experiment involving the proximity effect in the F/S heterostructure SRO_{113}/SRO_{214} proves the possibility of injecting a triplet current without the aid of a magnetic inhomogeneity layer over 15 nm, simplifying the device structure[37]. Additionally, Josephson junctions have been fabricated to investigate the proximity effect between conventional and unconventional superconductors to study their symmetry incompatibility. Some tunnelling studies using SRO_{214} single crystals (odd parity) have been done on Josephson junctions including Pb[10,38], Sn, or Nb[39,40] (even parity). All the experiments were limited by the presence of impurities, Ru inclusions, and a poor interface, so no clear evidence could be extracted as a whole. Additionally, a study by scanning tunnelling microscopy reported a surface reconstruction of SRO_{214} crystals with insulating behaviour after cleaving[41] (**Figure 1.8**), which makes it more challenging to analyse the results obtained from bulk based devices.

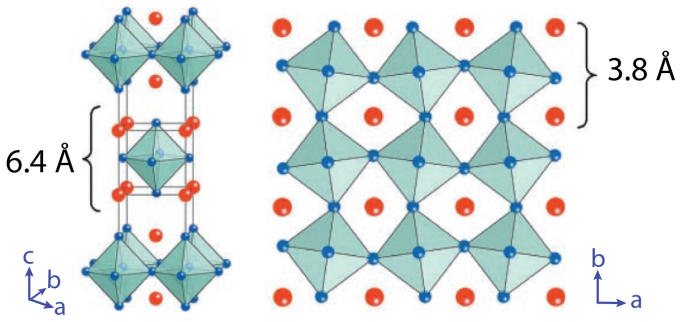

Figure 1.8 Schematic illustration of the rotation of the RuO_2 layer on the surface of Sr_2RuO_4 single crystals post cleaving. (From[41]).

Reproducible interfaces and junctions are needed. The pioneering phase-sensitive experiments in the cuprates were performed on thin-film based devices. However, achieving

this goal with SRO_{214} is far more complex since there is a lack of reproducibility on the production of superconducting SRO_{214} thin-films.

1.3 Strontium ruthenate thin-films

1.3.1 Pulsed laser deposition

Metallic Sr_2RuO_4 (SRO_{214}) thin-films were first reported in 1998 by Scholm *et al.*[42] using pulsed laser deposition (PLD). They deposit *c*-axis oriented SRO_{214} thin-films on different substrates, including (0 0 1) $(LaAlO_3)_{0.3}(Sr_2TaAlO_6)_{0.7}$ (LSAT), (1 0 0) $SrTiO_3$, (1 0 0) $LaAlO_3$, and (1 1 0) $NdGaO_3$; and *a*-axis oriented on (1 0 0) $LaSrGaO_4$ and (1 0 0) $LaSrAlO_4$, from the ablation of a high purity (99.98 %) SRO_{214} polycrystalline target. However, none of the samples showed superconductivity, which they attributed to structural defects through the broadening of X-ray diffraction peaks.

It was not until 2010 when Krockenberger *et al.*[43] improved previous results and reported the first evidence for superconductivity in SRO_{214} thin-films on (0 0 1) LSAT substrates; also from the ablation of a polycrystalline and stoichiometric SRO_{214} target. They recorded an onset critical temperature ($T_{c\text{-onset}}$) of 0.9 K, below the bulk T_c (≈ 1.5 K), and with a transition broadening of 500 mK (**Figure 1.9a**), which is wider than on single crystals (< 100 mK). Compared to previous attempts, they succeeded in finding the right deposition *T* (920˚C) to achieve stable SRO_{214} in the narrow growth widow, but with no reproducibility.

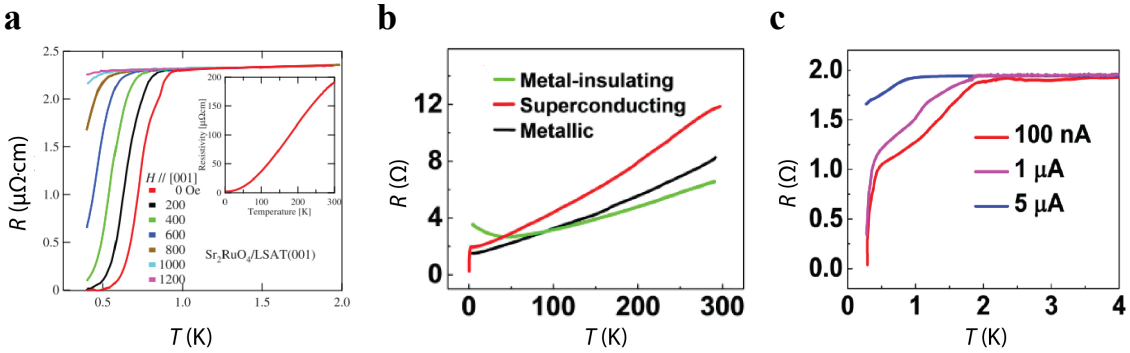

Figure 1.9 Electric transport characteristics of SRO_{214} superconducting thin-films deposited by pulsed laser deposition. a, Resistivity dependence with temperature with an out of plane field applied (0 - 1200 Oe) (From [43]). **b-c,** Resistance versus temperature curve. In (**b**) the green, black and red curves represent thin-films deposited from a stoichiometric target, 5% and 15% of Ru excess respectively. In (**c**) the curves represent the current dependence on the superconducting transition when using a target with 15% excess of Ru (From [44]).

In 2016 J. Cao *et al.*[44] succeded on the growth of a few superconducting thin-films on (0 0 1) LSAT substrate. They tested the effect of using a polycrystalline target with a 15% excess of Ru and reported increased residual resistivity ratio *(RRR* = 6.3 versus 1.8) and

superconductivity on the films compared to the stoichiometric target. However, besides the increased T_c onset reported (1.9 K) the superconductivity was reduced to localized regions and with a broad transition (1.6 K) (**Figure 1.9b-c**). They attribute the lack of homogeneity on the electrical properties of the thin-film to the presence of stacking faults that might have created micro-strained regions with increased T_c.

1.3.2 Molecular beam epitaxy

Over the past couple of years, the growth of SRO_{214} thin-films has become of interest for researchers again, and a few groups are working on the growth-optimization using molecular beam epitaxy (MBE).

In 2017, Marshall *et al.*[45] reported the MBE growth of SRO_{214} thin-films on (0 0 1) LSAT substrates, but they did not report any superconducting transition. Uchida *et al.*[46] achieved the first successful superconducting thin-films by MBE using LSAT substrates and observed enhanced electrical properties when the Ru/Sr flux ratio was enhanced (0.48 - 0.53). Their best films reached a *RRR* of 30 and a T_c onset of 1.1 K, with a sharp transition (0.3 K) (**Figure 1.10**).

In the most recent publication from Nair *et al.*[47], they achieved superconductivity on MBE deposited SRO_{214} thin-films on (1 1 0) $NdGaO_3$, showing an enhanced T_c onset of up to 1.8 K. They attributed the enhancement of the T_c to strained induced from the mismatch with the substrate (**Figure 1.11**). Additionally, they reported the growth conditions required for the thermodynamic growth window of SRO_{214} (oxygen pressure, temperature, and Ru/Sr flux ratio).

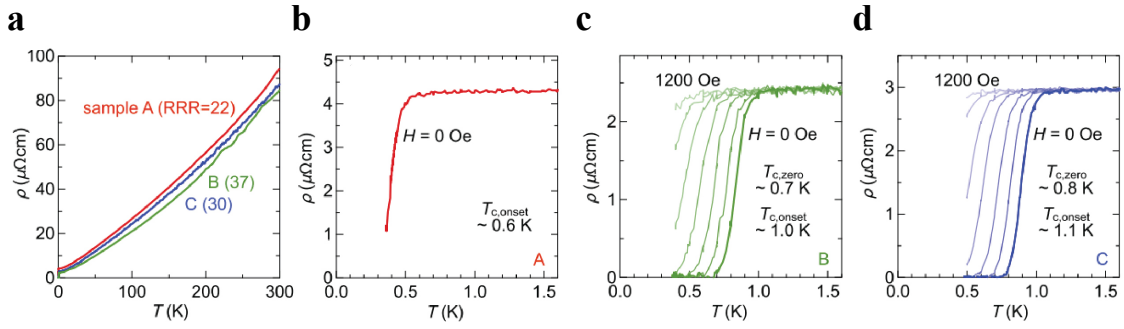

Figure 1.10 Electric transport characteristic of SRO_{214} superconducting thin-films deposited by molecular beam epitaxy. a-c, Resistivity versus temperature for samples deposited with a Ru/Sr flux ratio of 0.48 (**b**-red curve), 0.50 (**c**-green curve) and 0.53 (**d**-blue curve). (From [45]).

As observed, the last 3 years have been very active in the research towards the development of superconducting thin-films due to the large interest. One of the latest publications by Uchida *et al.*[48] went a step further and fabricated the first Josephson junction SRO_{214}/SRO_{214} on a thin-film grown by MBE; a weak link micropatterned. Regarding the superconducting symmetry of

SRO_{214}, their results show the unlikely possibility of SRO_{214} having a chiral-p-wave symmetry and encourages more theoretical studies based on the experimental data.

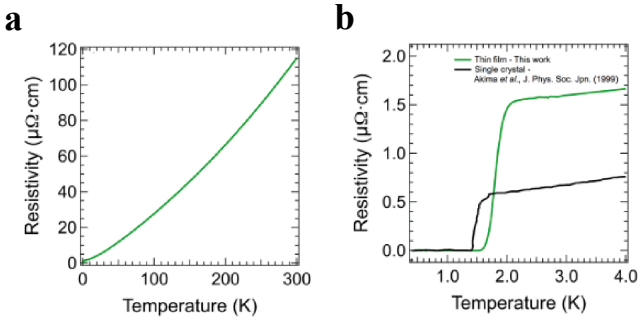

Figure 1.11 Electrical characterization of an SRO_{214} thin-film deposited by molecular beam epitaxy on a $NdGaO_3$ substrate. a-b, Resistivity versus temperature characteristic down to low temperature, from room temperature (**a**) and 4 K including the comparison with SRO_{214}-single crystal (**b**). (From [47]).

1.4 Overview of the challenges

The following major issues need are addressed in this thesis:

- The high demand for superconducting SRO_{214} thin-films to overcome the challenges associated with bulk-based experiments and to bring clarity to the ambiguity around the symmetry of this unconventional superconductor.

- The lack of reproducible superconducting SRO_{214} thin-films grown by pulsed laser deposition (PLD). Compared to molecular beam epitaxy (MBE), PLD growth of thin-films is more challenging based on the dynamic nature of the process and the large combination of parameters that can be tuned during growth (total pressure, backing pressure, substrate temperature, substrate-target distance, laser energy fluence, laser frequency, etc). We believe that PLD can provide more versatility on future steps when fabricating thin-film-based devices since multilayer structures can be easily deposited by changing the target and without breaking vacuum inside the PLD chamber. Therefore, in this thesis, a systematic procedure for the growth of reproducible superconducting SRO_{214} by PLD is provided.

- Extreme sensitivity to impurities and defects, which due to its unconventional properties, rapidly suppresses the superconductivity of the thin-films. This problem is addressed by studying the substrates and targets used and providing an in-depth analysis of the structural properties by X-ray diffraction complemented with transmission electron microscopy techniques. From the study, we identified the in-plane mosaic twist, as the main structural defect responsible for the suppression of superconductivity.

Chapter 2

Experimental methods

2.1 Thin-film fabrication

2.1.1 Pulsed laser deposition

Pulsed laser deposition (PLD) is a physical vapour deposition technique used for the growth of thin-films and in particular oxides. PLD involves the removal of material from a solid target with a pulsed laser with high energy density (300 – 1200 mJ), in which the ablation creates a plasma column that transfers the stoichiometric material onto the surface of a substrate. The growth occurs in vacuum conditions or an inert gas, and with the addition of reactive gasses, new compounds that differ from the target stoichiometry can be formed (**Figure 2.1**).[49,50]

The ablation of the target requires the excitation of the ablated volume to temperatures above that required for evaporation. The laser pulses must be short, with a high energy density to maximize its absorption by the target material. This is achieved by using a laser in the ultraviolet range, provided by excimer lasers or solid-state lasers Nd:YAG with the frequency-tripled or quadrupled. For multi-component targets, the ablation is nonuniform if the energy is not high enough, so it is desirable to work at sufficiently high fluences (energy by area of the laser spot measured in $J \cdot cm^{-2}$) to vaporize all the species and achieve the exact transfer of the target stoichiometry. In contrast, if the kinetic energy of the ablated atoms is too high (100 eV), it will result in the bombardment of the substrate with highly energetic species impinging the surface with interstitial defects, creating compressive strain in the growing film.

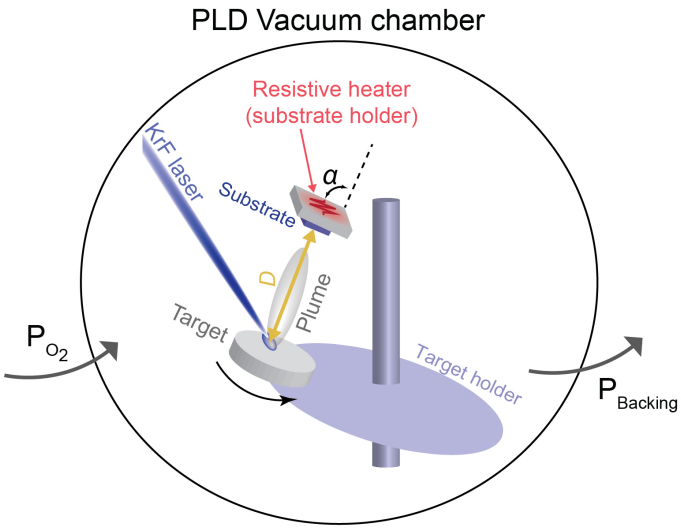

Figure 2.1 Schematic illustration of PLD. The substrate-target distance is *D* and the angle between the substrate and the plume is *α*.

When selecting the target, larger density is desirable since it is linked to lower formation of particulates (0.1 - 0.4 μm size) or droplets (1 μm size) during the deposition which increase the roughness of the surface of the thin-film or even create multilayers structures. Particulates can be controlled by either altering the kinetics of the plasma with the effect of the gas pressure or similarly, the substrate to target distance (*D*) (**Figure 2.1**). At low pressure, because the speed of the atoms is high, larger *D* is required to minimize substrate damage. In contrast, at low pressure, the opposite effect occurs, and a shorter *D* is needed to activate the substrate surface and obtain a flat thin-film surface. Alternatively, mechanical solutions are also accessible, -i.e. filters, a PLD configuration with the substrate above the target, off-axis configuration (**Figure 2.2**), or the replacement of the polycrystalline targets by single-crystal targets (higher density).

The substrate provides mechanical support and serves as a template for the growth of the thin-film without interfering with its properties. For epitaxial thin-films, the substrate provides the desired crystallographic orientation, which requires good lattice matching and crystal orientation to minimize defects arising from the interface due to stain[51]. In addition, the crystallinity of the film is highly affected by the substrate temperature, which modifies the surface mobility of the vapour atoms. Sufficient high temperature favours defect-free growth whereas low temperatures may result in amorphous structures.

The final stoichiometry of the thin-film is influenced by the gas introduced in the chamber i.e. growing in a reactive atmosphere that interacts with the ablated species or increasing the pressure, which affects the kinetic energy of the plume and slowing down its expansion.

In this work, the two PLD systems are used as described in detail in **Chapter 3** and **Chapter 4**.

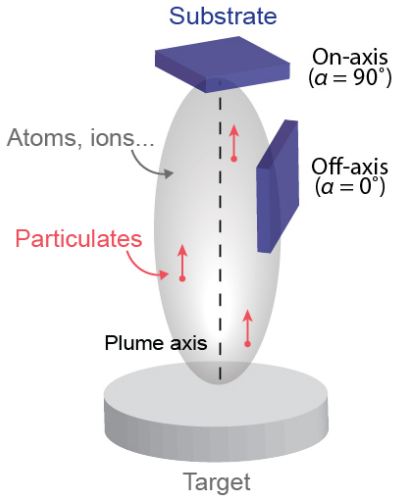

Figure 2.2 Schematic illustration of the PLD plume interaction with the substrate in an on- and off-axis configuration.

2.2 Characterization of the structural properties

2.2.1 X-ray diffraction

X-ray diffraction (XRD) is used to perform the qualitative and quantitative phase identification analysis and to obtain a better understanding of the microstructure (e.g. crystallite size, orientation, or stress) as a function of different growth parameters.

XRD consists of the diffraction of an incident beam of X-rays (primary side) on a sample collected in a detector (secondary side) while varying the angles of the incident beam with the sample (2θ). The collected signal corresponds to a series of peaks (diffraction pattern) containing information of the sample object of study.

In a crystalline solid, atoms are periodically arranged in planes separated by the interplanar spacing (d_{hkl}). At certain angles (θ), X-ray waves scatter coherently on atoms of nearby planes when the optical path difference given by $d_{hkl}\sin(\theta)$ is a multiple of the wavelength (nλ), following Bragg's law (**Equation 2.1**). This coherent scatter results in the constructive interference of the signal and builds the diffraction pattern of the sample, whereas the remaining angles lead to incoherent scatter and destructive interactions.[52]

$$n\lambda = 2d_{hkl}\sin\theta \qquad \textbf{2.1}$$

X-rays are generated in a vacuum tube when the electrons emitted from a filament (cathode) are accelerated with an external voltage towards an anode. From the collision, X-rays are emitted from the anode tube through a beryllium window. For the case of a copper anode, the characteristic spectrum emitted contains $CuK_{\alpha 1}$ (1.54056 Å), $CuK_{\alpha 2}$ (1.54439 Å) and CuK_{β} (1.39222 Å) radiation. The CuK_{β} radiation is suppressed with a monochromator or a filter (of nickel for this anode type) that absorbs its wavelength.

The control of the illuminated area of the sample surface is done through divergence slits located on the primary side to avoid over-illumination, and on the secondary side, through anti-scatter slits to ensure that only the diffracted beam goes to the detector (the size should be equal to the divergence slit). Additionally, receiving slits are located at the focal point after the anti-scatter slits; they determine the resolution/intensity that reaches the detector depending on the application (**Figure 2.3**). Complementary, some diffractometers allow the use of programmable slits to ensure a constant surface illumination when varying the angles, compared to manual slits that ensure a constant volume illumination.

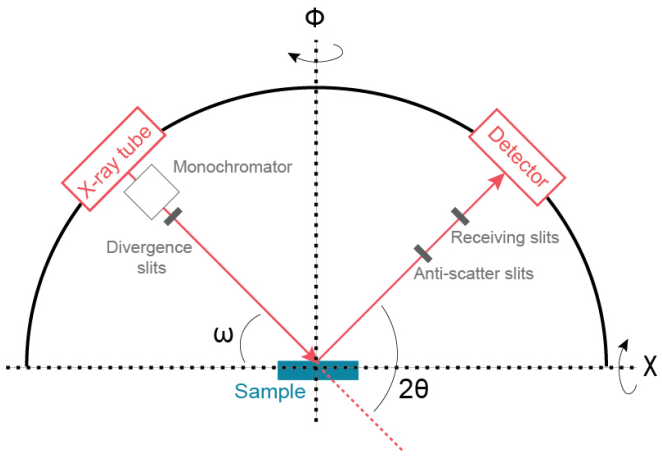

Figure 2.3 Schematic diagram of the X-ray setup.

Depending on the type of information we aim to obtain, it is possible to control the incident beam angle with the sample stage, omega (ω), and with the detector, two theta (2θ), the tilt angle of the sample stage, chi (χ), and the rotation of the sample stage about its axis, phi (φ) (see **Chapter 5** for the information that can be obtained from the different types of scan).

Phase identification and lattice parameters

From the diffractogram of a thin-film, the peak positions in 2θ allow us to identify the phase that created the diffraction pattern by correlating the angles with the International Centre for Diffraction Database or ICDD. For each peak position, d_{hkl} is calculated using Bragg's law

(**Equation 2.1**), which leads to the family of planes $\{h\ k\ l\}$. The lattice parameters (a, b and c) of a unit cell with orthogonal axes are calculated via the relation:

$$\frac{1}{{d_{hkl}}^2} = \frac{h^2}{a^2} + \frac{k^2}{b^2} + \frac{l^2}{c^2} \qquad \textbf{2.2}$$

In this thesis, the diffractograms shown in **Chapter 3** and **4** have been coloured based on the indexing of peaks according to the phases present on the thin films: SRO_{214} (orange), SRO_{113} or SRO_{4310} (red), SRO_{327} (green), RuO_2 (pink) and LSAT substrate (blue). The lattice parameters of SRO_{214} ($a = b \neq c$) have been calculated following **Equation 2.2**.

Correction of the data

For an accurate calculation of the lattice parameters, the following sources of error must be accounted for:

- Instrument misalignment. To ensure the correct alignment of the optics, we select a plane from the substrate with the strongest diffraction peak among the planes with similar χ and φ values as the ones we aim to measure on the thin film. Then, the selected diffraction peak of the substrate is used to record the offsets of the instrument (ω_{offset}, χ_{offset}, and φ_{offset}).

- Absorption of X-rays in the specimen when the sample is thick. In this study, the thickness of the thin-films is below 200 nm, and therefore, this type of error does not apply.

- Displacement of the sample from the diffractometer axis. This occurs when the sample height is different from the focal plane of the beam and it results in the shift of the diffraction peaks of a 2θ-ω scan (**Figure 2.4a**). To solve this issue, the c lattice parameter, calculated for each peak position in 2θ following **Equation 2.1** and **2.2**, is plotted against a correction function ($\cos^2\theta \sin\theta$), and the resulting plot is linearly fit (**Figure 2.4b)**. The highest precision is obtained at larger values of 2θ, where the variation of the interplanar distance is minimum ($\Delta d_{hkl} \propto \cot(\theta)$). Therefore, the intercept with the vertical axis ($2\theta = 180^\circ$), where the peak deviation in 2θ has the lowest angle deviation, provides the c-axis value corrected for sample displacement.

- Systematic and random errors must also consider. From the extrapolation to $2\theta = 180^\circ$ the systematic error which is proportional to the slope of the extrapolation line is suppressed.

The random error can be calculated from the error of the least square fitting of the data, which represents the deviation of the experimental data points from the linear curve.

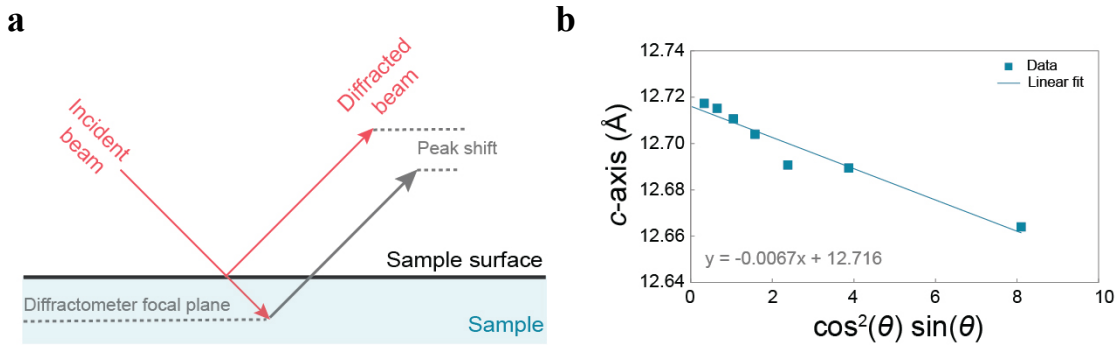

Figure 2.4 Sample displacement error. a, Schematic illustration of error due to sample displacement. **b**, Calculation of the *c*-axis lattice parameter correcting the data for sample displacement. The resulting *c*-axis value is 12.716 Å corresponding to the intercept with the vertical axis.

Calculation of the thin-film thickness

In high quality films thickness fringes are visible, and the spacing between fringes, $n_{i,j}$, is correlated with the thickness of the thin film following:

$$t = \frac{(n_i - n_j)\lambda}{2(\sin\theta_i - \sin\theta_j)} \qquad (2.3)$$

where λ is the X-Ray wavelength in nm units, and $\theta_{i,j}$ is the Bragg angle of the corresponding fringe in radians.

In this thesis, the thickness (t) of the films shown in **Chapter 5**, is obtained by fitting a model to a 2θ-ω scan on the diffraction peak SRO_{214} (0 0 6) using LEPTOS software (see **Figure 2.5**). The samples shown in **Chapter 3** have not been characterized for t due to the lack of fringes (poor quality) and excessive roughness (> 2 nm), which also makes the alternative characterization of t using X-ray reflectivity not possible.

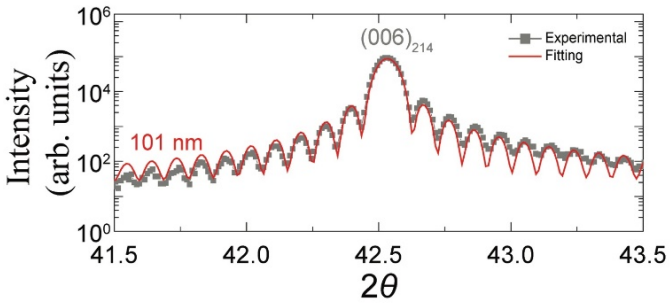

Figure 2.5 Example of thickness calculation of an SRO_{214} thin film extracted from the thickness fringes. 2θ-ω X-ray diffraction trace of the (0 0 6) peak of a Sr_2RuO_4 film (grey squares) with a model thickness of 101 nm from the fitting to simulation (red curve).

Quantitative analysis

The reference intensity ratio (RIR) is a method used for the quantitative analysis of XRD traces[53]. It involves scaling the data from a diffractogram (experimentally obtained) with data from a reference standard diffractogram (from ICDD).

For the calculation of the percentages of phases "A" and "B" from an XRD pattern it is used:

$$\frac{I^{\mathrm{A}}_{h_1k_1l_1}}{I^{\mathrm{B}}_{h_2k_2l_2}} = \mathrm{K}\frac{x^{\mathrm{A}}}{x^{\mathrm{B}}} \qquad \textbf{2.4}$$

where $I^{\mathrm{X}}_{hkl}$is the XRD intensity of an (*h k l*) diffraction plane of the phase "A" or "B", and x^{X} is the weight fraction of the phase "A" or "B". K corresponds to the ratio between both phases, and it is calculated by applying **Equation 2.4** on a simulated diffraction pattern on High-Score software that contains both phases (from ICDD) with known weight fractions.

Subtraction of instrumental broadening

The steps to consider the instrumental contribution are as follow:

1. X-ray diffraction peaks are fitted with a pseudo-Voigt profile to obtain both the peak width (FWHM) and the shape ratio of Gaussian to Lorentzian (x).

2. Known the instrumental broadening ($\mathrm{FWHM_{Inst}}$) the width of the peak that corresponds only to the sample coming from the Lorentzian contribution ($\mathrm{FWHM^{L}_{Sample}}$) is calculated following **Equation 2.5**, and for the Gaussian contribution ($\mathrm{FWHM^{G}_{Sample}}$), **Equation 2.6**.

3. The total broadening of the peak ($\mathrm{FWHM^{PV}_{Sample}}$) without the instrumental contribution, is calculated by their sum using **Equation 2.7**.

Lorentzian profile: $$\mathrm{FWHM^{L}_{Meas}} = \mathrm{x\ FWHM^{PV}_{Meas}} = \mathrm{x\ FWHM_{Inst}} + \mathrm{FWHM^{L}_{Sample}} \qquad \textbf{2.5}$$

Gaussian profile : $$\left(\mathrm{FWHM^{G}_{Meas}}\right)^2 = \left((1-\mathrm{x})\ \mathrm{FWHM^{PV}_{Meas}}\right)^2 = \\ = \left((1-\mathrm{x})\ \mathrm{FWHM_{Inst}}\right)^2 + \left(\mathrm{FWHM^{G}_{Sample}}\right)^2 \qquad \textbf{2.6}$$

Pseudo-Voigt profile: $$\mathrm{FWHM^{PV}_{Sample}} = \mathrm{FWHM^{L}_{Sample}} + \mathrm{FWHM^{G}_{Sample}} \qquad \textbf{2.7}$$

The instrumental broadening of ω scans is defined by the primary monochromator, 0.0066˚, and of 2θ-ω scans, it is defined by the spread in wavelength and increases with 2θ from 0.012˚to 0.059˚(**Table 2.1**).

Table 2.1 Instrumental broadening in 2θ. Extracted from the simulations on Epitaxy software of different diffraction peaks of Si crystal considering the optics used in our measurements.

2θ (˚)	$\mathbf{FWHM_{Inst}}$ (˚)
> 70	0.0130
31.63	0.0117
35.57	0.0150
66.05	0.0143
69.19	0.0146
73.00	0.0169
109.67	0.0374
126.00	0.0585

Calculation of the angle between two crystallographic planes

The following equation is used to calculate the angle between a plane ($h_1\ k_1\ l_1$) and ($h_2\ k_2\ l_2$) simplified for a tetragonal unit cell ($a = b$ and c):[53]

$$\phi = arccos\left(\frac{\frac{h_1h_2 + k_1k_2}{a^2} + \frac{l_1l_2}{c^2}}{\sqrt{\left(\frac{h_1^2 + k_1^2}{a^2} + \frac{l_1^2}{c^2}\right)\left(\frac{h_2^2 + k_2^2}{a^2} + \frac{l_2^2}{c^2}\right)}}\right) \quad \textbf{2.8}$$

Reciprocal space

Consists of the 3D illustration based on the Fourier transform of the crystallographic structure in the real space. It is composed of reciprocal lattice points, RLP, that correspond to the diffraction planes ($h\ k\ l$). The vector that connects the reciprocal space origin (0 0 0) with each RLP is called the scattering vector, $\vec{s}$, its length is correlated to d_{hkl} via $|\vec{s}| = 1/d_{hkl}$, and its direction corresponds to the normal of the ($h\ k\ l$) plane (**Figure 2.6**). *S*x is the projection of $\vec{s}$ in the x-axis and *S*z, the in the z-axis respectively. Sx and Sz can be transformed into the real space following:

$$Sx = 1/\lambda\ [\cos(\omega) - \cos(2\theta - \omega)] \quad \textbf{2.9}$$

$$Sz = 1/\lambda\ [\sin(\omega) + \sin(2\theta - \omega)] \quad \textbf{2.10}$$

for a given RLP, the correlation between the broadening of the RLP, Δs, and the FWHM of the X-ray diffraction peak in the real space is given by:

$\Delta s \,||\, \vec{s}$: $$\Delta s = \text{FWHM}_{2\theta} / \lambda \cdot \cos(\theta) \quad \textbf{2.11}$$

$\Delta s \perp \vec{s}$: $$\Delta s = 2\,\text{FWHM}_{\omega} / \lambda \cdot \sin(\theta) \quad \textbf{2.12}$$

where the FWHM is in radians.

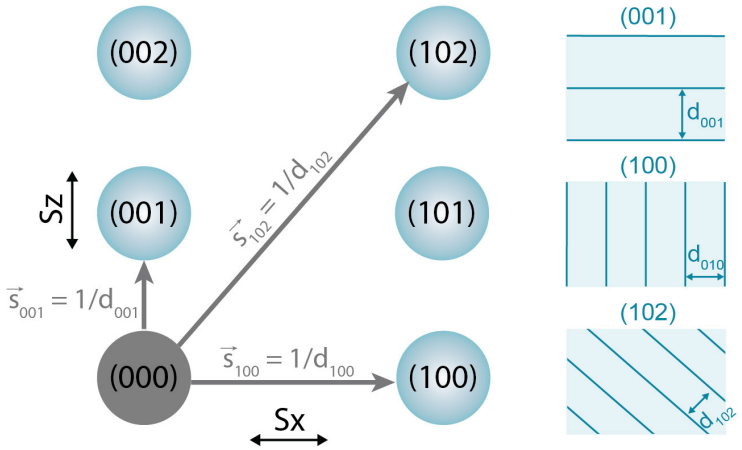

Figure 2.6 Representation of the reciprocal space and the correlation of the scattering vector with the real space. The left side image corresponds to the reciprocal space and the right-side image to the real space. The scattering vector is labelled $\vec{s}$ and the interplanar distance as *d*. In both cases, the subindex corresponds to a plane (*h k l*). Sx and Sz correspond to the projection of $\vec{s}$ in the x and z direction respectively. (Adapted from[52]).

In this work, the X-ray diffraction data is acquired using a Panalytical Empyrean X-ray diffractometer, with a $Cu_{K\alpha 1}$ X-ray source and a hybrid two bounce primary monochromator located in the Department of Materials Science and Metallurgy in the University of Cambridge (United Kingdom).

2.2.2 Atomic force microscopy

Atomic force microscopy (AFM) is used to determine the roughness of the thin-films as well as to investigate mosaic tilt from the map of the topography of the surface.

The AFM scans the sample surface with the aid of a sharp tip attached to a cantilever. When the tip approaches the sample surface, there is an attractive force that bends the cantilever towards the surface, and when the tip is near to the surface, it experiences an electrostatic repulsive force that deflects the cantilever in the opposite direction. The deflection that the cantilever experiences is based on the Hooke's law ($F = -\text{k}y$), where k is the cantilever spring constant and y, is the cantilever distance deflected from its neutral position. Changes in the deflection of the cantilever are tracked by a position-sensitive photodiode (PSPD) screen,

which detects changes in the direction of a reflected beam on the flat surface of the cantilever (**Figure 2.7**)[54].

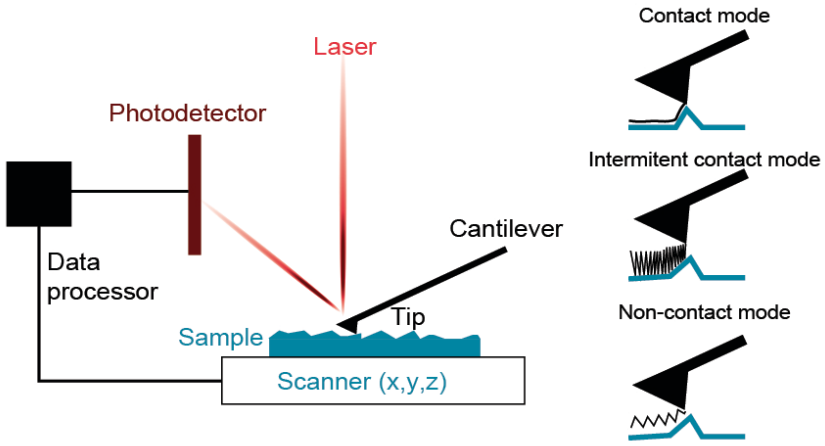

Figure 2.7 Schematic illustration of an atomic force microscope (left) showing the different operating modes (right).

AFM has different working modes. The most common are contact, intermittent contact, and non-contact. In contact mode, the tip of the cantilever is in soft contact with the surface of the sample, where the surface features cause a strong repulsion force that deflects the tip cantilever. In non-contact mode, the tip vibrates at a certain frequency and scans the surface right above it with the aid of a feedback loop that controls the oscillation and ensures the surface is untouched. Features on the surface are imaged by tracking changes in the oscillation signal (suitable for softer materials). In the intermittent contact mode, the vibration of the tip has a higher amplitude and the tip touches the sample. Non- and intermittent-contact scans are used to examine soft surfaces, sensitive to the vibration of the tip, or with particles weakly attached.

The AFM images in this thesis are taken from contact mode since it does not represent a threat for the thin-films. The data is levelled to make facets point upwards and coloured using Gwyddion software. Apart from the image of the surface, the value of the roughness is extracted from the root mean square (*RSM*) of the heights of the scanned area as a measurement of the quality of the thin-film. *RSM* values are more precise than only measuring average roughness (R_a) since the latter is not able to distinguish between peaks and valleys (**Figure 2.8**).

$$R_a = \frac{1}{n}\sum_{i=1}^{n}|y_i| \qquad \textbf{2.13}$$

$$RMS = \sqrt{\frac{1}{n}\sum_{i=1}^{n}y_i^2} \qquad \textbf{2.14}$$

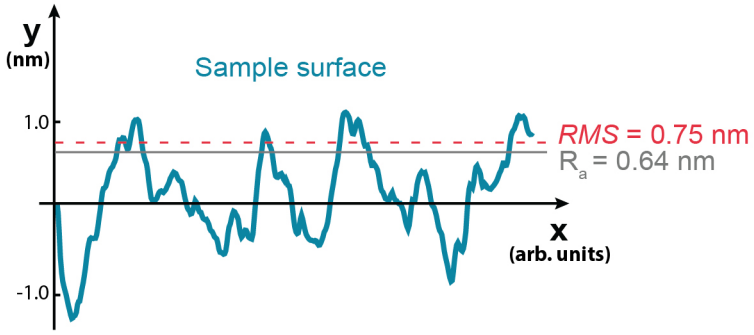

Figure 2.8 Example of a section of the surface profile of an SRO_{214} thin-film highlighting the difference between Ra and RSM. The height is indicated on the y-axis and the length on the x-axis.

In our work, we use a Cypher Atomic Force Microscope with contact mode located at the Institute of basic science, centre for correlated electron systems (IBS-CCES) at Seoul National University.

2.2.3 Scanning and transmission electron microscopy

A transmission electron microscope (TEM) is used to image the microstructure of a sample. The scale and information that can be obtained depend on the resolving power of the microscope (generally < 0.3 nm), the energy spread of the electron beam (several eV), the thickness of the specimen (> 1 μm) and the composition/stability of the material object of study.[55]

A beam of high energy electrons (100 - 400 keV) is transmitted through the sample and forms an image. From the beam interaction with the atoms of the specimen, inelastic and elastic scattering occurs, making possible to obtain fine details from its microstructure (composition, defects).

Whereas the conventional TEM has a parallel beam that floods the whole area of interest, scanning TEM (STEM) has a scanning focused beam that addresses each pixel in series. Several detectors can be used to collect the signal generated at each pixel, allowing high spatial resolution imaging (~ 0.15 nm in aberration corrected STEM probes) and compositional analysis.

Defects in the sample can be studied by modifying the contrast of the image using bright or dark-field imaging. “Bright field” term is used when the TEM image is formed only by un-scattered electrons (transmitted), blocking the rest with an aperture. In this case, since there is no scattering, the areas with higher atomic mass will appear darker. Whereas “dark field” term it is used when the un-scattered electrons are blocked, and a proportion of the scattered

electrons are selected with the aperture to form the image. In this case, areas with no material will appear dark, and regions that scattered electrons into the aperture appear bright.

An scanning electron microscope is used to image the microstructure of the scanned area with a resolution ~ 1 nm allowing topographic and compositional analysis. From the interaction of the primary beam of electrons with the sample different signals are emitted (secondary electrons, backscattered electrons, characteristic X-rays or visible light) that reveal different information of the specimen.[56]

The topography of the sample is analysed from the image generated with the intensity detected from secondary electrons, and the elemental composition, from the X-rays emitted from the sample, using an electron energy dispersive X-ray spectroscopy (EDX) detector.

In this work, SEM-EDX is applied in **Chapter 4** for the characterization of the Sr:Ru ratio of SRO single crystals based on the atomic percent using a KEYENCE VE-9800 equipped with an EDX AMETEK detector at 20 kV located in the University of Kyoto (Japan).

The TEM characterization of SRO_{214} thin films shown in **Chapter 5** and its corresponding sample preparation, are performed by Dr Giorgio Divitini and Dr Fabien Massabuau in the Department of Materials Science and Metallurgy at the University of Cambridge (UK). The cross sectional samples are milled using a focused ion beam microscope (Helios Nanolab). Bright-field TEM is used to perform the $\vec{g} \cdot \vec{b}$ analysis to confirm the presence of dislocations (described in detail in **Chapter 5**) using a FEI Tecnai Osiris at 200 kV. Compositional mapping to investigate the presence of impurities on thin films is carried out using STEM–EDX in the same instrument, employing a Super-X detector with a total collection solid angle of 0.9 sr. The maps have been coloured for Sr (green), Ru (pink) and O (blue) content, with the white regions indicating highest (relative) atomic content. High-resolution STEM images are acquired on a probe-corrected FEI Titan operated at 300 kV.

2.3 Characterization of the electric and magnetic properties

2.3.1 Electric properties at low temperature

Low-temperature electrical transport characteristic of the thin-films is obtained using a four-point measurement setup.

The resistance, R, is calculated as a function of temperature, T, using a current bias, I, of less than 100 μA between the external contacts and recording the voltage, V. The current is

chosen to ensure it does not affect the superconducting transition temperature but large enough to maximise the voltage signal to noise ratio.

For this thesis, thin-films are measured from room temperature down to 0.3 K with a pulse-tune cryogen-free system using a He^3 probe with a 7 T magnet.

Electrical contacts

The transport characteristic of the thin films in **Chapter 3** are measured directly on a region of the film (**Figure 2.9a**), and in **Chapter 4** and **5** (**Figure 2.9b**), via four electrical contacts of Au sputtered across the films using a metallic "shadow" mask. Each Au pad is electrically connected to a chip carrier using Al wires bonds with a diameter of 25 µm using an ultrasonic wire bonder.

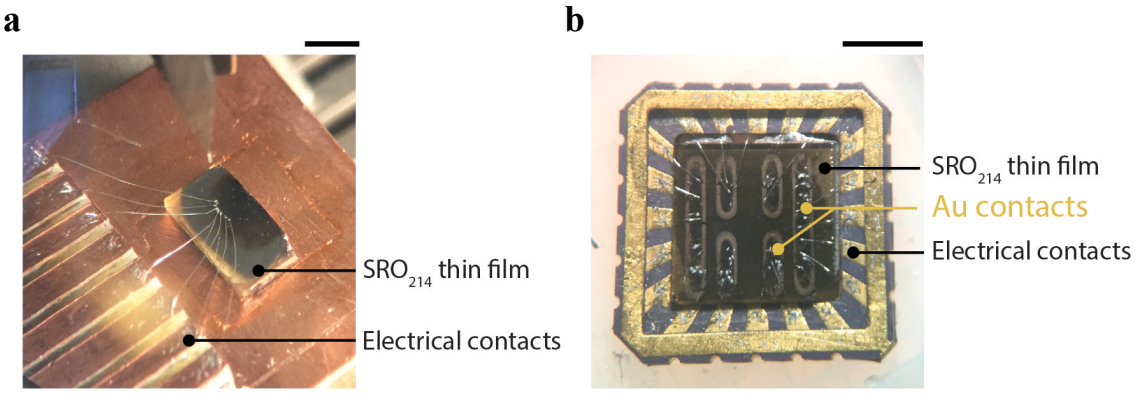

Figure 2.9 Photograph showing the electrical contacts on SRO_{214} thin films. a-b, Electrical contacts directly performed on the film (**a**) and via Au pads (**b**). The scale bar in **a-b,** correspond to ~ 0.5 cm.

Residual resistivity ratio (*RRR*)

A good indicator of the purity of a material is the residual resistance ratio (*RRR*), which corresponds to the coefficient of the resistance at high versus low temperature (equation **2.15**). This is because at high temperature the resistance of a metal is governed by the scattering of electrons due to thermal excitation (phonons) and collisions with impurities in the crystal. However, when the temperature is low, the thermal excitation is minimized, and the main source of the resistance are imperfections in the lattice.

$$RRR = \frac{R_{\mathrm{RT}}}{R_{\mathrm{LT}}} \qquad \textbf{2.15}$$

where R_{RT} is the resistance at room temperature and R_{LT} at low temperature.

In this thesis, the R_{LT} for superconducting samples corresponds to the value of the resistance before the superconducting transition occurs, and for non-superconducting samples (metallic), to the saturated minimum in the resistance. High values of *RRR* correlate to high purity and small concentration of impurities or defects. As a reference, the highest *RRR* reported to date on SRO_{214} thin films is ~ 80 (see literature comparison on **Figure 5.10**).

Magnetic measurements

The magnetic characteristics of the thin-films are investigated using a magnetic property measurement system (MPMS)[57]. The equipment operates in a range of temperatures (400 - 1.8 K) using liquid He and can apply magnetic fields up to 7 T generated by a superconducting magnet. The signal from the sample is detected by a superconducting quantum interference device (SQUID). Both magnets are cooled down in liquid helium. While using the DC measurements scans, the sample is shifted through the pick-up coils, which generates a SQUID voltage proportional to its magnetic momentum, depending on the position and field applied. Additionally, liquid nitrogen is also used to prevent heat loss from the He tank.

Chapter 3

Growth of SRO_{214} metallic thin-films

3.1 Background

Before the optimization of the growth parameters (O_2 pressure, laser fluence, or temperature) for the fabrication of SRO_{214} thin-films, two key aspects are addressed based on reported studies on SRO_{214} thin-films (described in **Chapter 1**): target stoichiometry and substrate selection.

Regarding the target, the most important parameter is the Ru content. RuO_2 is well known to be very volatile due to its high vapour pressure, so when using a stoichiometric SRO_{214} target the final stoichiometry of the resulting thin-film is likely to be Ru deficient. As a reference, during the fabrication process of SRO_{214} single crystals, Z.Q. Mao *et al.*[23] added a 15% Ru excess to the feed rod composition, instead of the stoichiometric formula Sr_2RuO_4, to ensure that the resulting crystal had the correct Ru content after the Ru evaporation. Based on that, J. Cao *et al.*[44] investigated the effect of the Sr/Ru ratio in the target composition (from stoichiometric to 15% Ru excess) on the electrical properties of pulsed laser deposited (PLD) SRO_{214} thin-films. They realised that only thin-films deposited from the ablation of a target with 15% of Ru excess ($Sr_2Ru_{1.15}O_4$) showed evidence for incipient superconductivity, with an elevated (onset) critical temperature ($T_{c\text{-}onset}$) of 1.9 K, and a residual resistivity ratio (*RRR*) of 6.3, larger compared to those from a stoichiometric target (*RRR* = 1.8). The high $T_{c\text{-}onset}$ compared to the T_c in SRO_{214} (1.5 K), together with the broad superconducting transition (1.6

K) was associated with structural defects (further discussed in **Chapter 5**). Similarly, Uchida *et al*.[46] studied different Ru/Sr flux ratios (from 0.48 to 0.53) on SRO_{214} thin-films deposited by molecular beam epitaxy (MBE). In their report, all the films were superconducting, with improved $T_{c\text{-onset}}$ (1.1 K - 0.57 K) and *RRR* (37 - 22) values at higher Ru/Sr flux ratio, but with a rougher surface (*RMS* = 9 - 0.4 nm), most likely due to the segregation of RuO_2.

When selecting the substrate, it is important to ensure a minimal lattice mismatch with the SRO_{214} thin-film to reduce the number of defects arising at the interphase (i.e stacking faults commonly observed in layered perovskites). For instance, $(LaAlO_3)_{0.3}(Sr_2TaAlO_6)_{0.7}$ (LSAT) crystal provides a very low lattice mismatch in-plane (0.03 %), but an elevated mismatch in the out-of-plane direction (69.64%). Despite that, in PLD, only SRO_{214} thin-films deposited on (0 0 1) LSAT[43,44] substrates show traces of superconductivity, though with reproducibility issues. There are also attempts on different perovskite substrates, (1 0 0) $SrTiO_3$, (1 0 0) $LaAlO_3$, and (1 1 0) $NdGaO_3$, but all leading to metallic behaviour at low temperatures and no traces of superconductivity[1]. Nevertheless, it is worth to mention that superconducting SRO_{214} thin-films deposited by MBE, have been recently achieved on (0 0 1) LSAT, and also (1 1 0) $NdGaO_3$[46,47].

In this chapter, it is first investigated the growth of SRO_{214} thin-films using a sintered polycrystalline target of SRO_{214} with 15% Ru excess, and (0 0 1) LSAT substrates. Following previous results on PLD, it is studied the effect of the growth parameters on the structural and electrical properties, and also, different thermal annealing processes to enhance the films after the deposition.

3.2 Growth conditions

The thermodynamic stability lines of SRO[42,58] (reproduced in **Figure 3.1**) help to understand the effect of changes in the O_2 pressure and the substrate temperature (*T*) during the deposition on the stoichiometry of the resulting thin-film. **Figure 3.1** indicates that unstable SRO_{214} easily decomposes into other phases of the same family, including SRO_{113} or SRO_{327}.

In general, each phase is stable when the growth conditions are located below their corresponding stability line. However, the O_2 pressure or *T* do not strictly correlate with the stability lines showed for some thin-films. For instance, the growth conditions reported of superconducting SRO_{214} thin-films by PLD (yellow circles with added references), are not located below the SRO_{214} stability line. This could be because each PLD system has different characteristics that could affect the pressure, i.e. background pressure, substrate-to-target distance, chamber dimensions, O_2 released during the target ablation or backing pressure among

others. Therefore, from this study, the key is that stable SRO_{214} will tend to form at an O_2 pressure lower than SRO_{113} or SRO_{327}, where the other phases are no longer stable. Based on that, in this study, the initial O_2 pressure selected follows other reported results and according to the phases present on the deposited films, it is re-adjusted towards the direction of single-phase SRO_{214}.

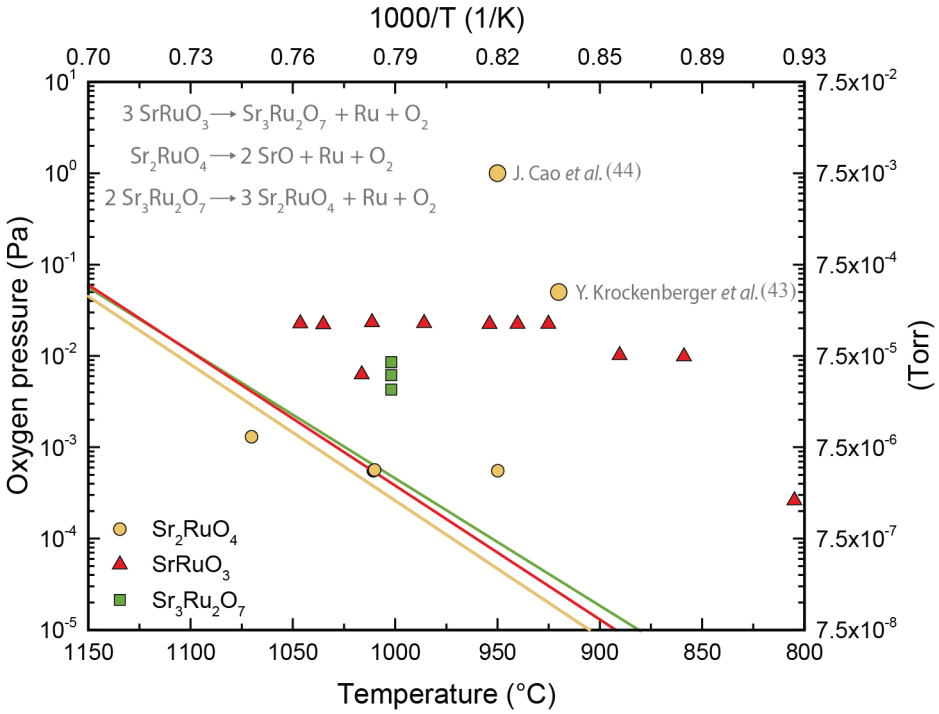

Figure 3.1 Stoichiometric stability diagram of SRO_{214}, SRO_{113}, and SRO_{327} phases versus growth *T* and O_2 pressure. The diagram includes the thermodynamic stability lines of SRO phases, experimental results of thin-films deposited with the indicated O_2 pressure and *T* with different stoichiometries, Sr_2RuO_4 (yellow circles), $SrRuO_3$ (red triangles) and $Sr_3Ru_2O_7$ (green squares), and chemical reactions of the decomposition of SRO phases when unstable. (From[42,58])

Regarding the substrate *T*, Krockenberger *et al.*[43] achieved superconducting SRO_{214} thin-films using a growth *T* of 950˚C, and only observed reflection high-energy electron diffraction (RHEED) oscillations in a narrow growth window (< 10˚C). Similarly, superconductivity is observed in PLD films grown by J. Cao *et al.*[44] when *T* is optimized to 950˚C. Nevertheless, Madhavan *et al.*[59] explored *T* in the range of 950˚C to 1050˚C using PLD, but with no trace of superconductivity in *a*- or *c*-axis oriented SRO_{214} thin-films. Following previous attempts and the limitations of our equipment, this study explores a range of *T* near 950˚C.

3.3 Post-annealing treatments

The electrical properties of SRO_{214} could be enhanced also after growth if structural defects are removed. A study performed on SRO_{214} single crystals by Mao *et al.*[9] showed that decreasing

crystallographic defects by annealing the crystals at high T (1200 - 1500˚C) in air for 3 days, shifted the T_c to a higher temperature.

Based on that, once the thin-films are deposited, post-annealing treatments in vacuum and air are run on SRO_{214} thin-films to test if the structural and electrical properties are improved.

3.4 Thin-film fabrication set up description

3.4.1 Description of the PLD system

The PLD system used for the growth of SRO_{214} thin-films in this Chapter ("101 system") is located in the Department of Materials Science & Metallurgy at the University of Cambridge. The target is located at the bottom of the chamber and the substrate above it at an adjustable angle (α), making possible to perform on- (α = 90˚) or off-axis (α = 0˚) depositions (**Figure** 3.2).

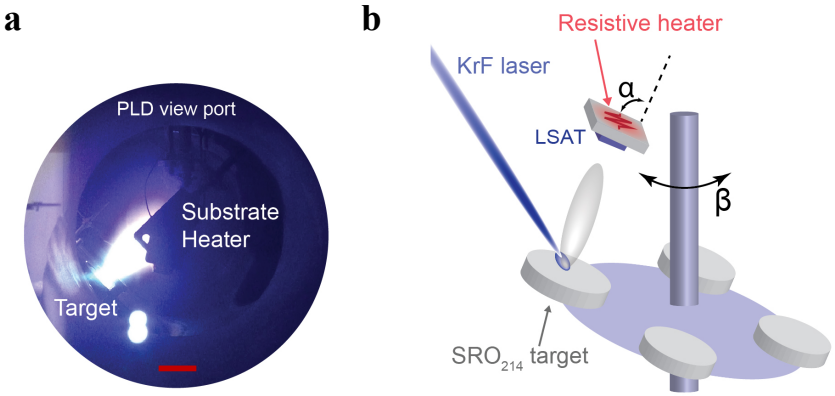

Figure 3.2 PLD system in Cambridge used for growing SRO_{214} thin-films. a, A photograph from one of the PLD viewports during the deposition of SRO_{214}. The target and the heater are labelled. The deposition is performed at an angle α**. b,** An schematic illustration of the PLD set-up, showing the substrate-target configuration. The angle of the heater is labelled as α, and the rotation of the target as β. The scale bar in **a** corresponds to ~ 2.5 cm.

During the growth, the target is ablated by a Lambda Physik KrF pulsed-laser (λ = 248 nm) while rotated about its axis and shifted left to right, with small rotations of the target carousel (β). This way, the overheating of one spot and the creation of particulates that could damage the surface of the substrate are prevented. The target carousel can load up to six targets, so it is covered with a metallic shield with a gap that allows the laser to ablate only the desired target. Simultaneously, a resistive heater (**Figure 3.3a**) provides the set temperature (up to 960˚C) to the substrate through contact with thermal paste.

Before the deposition, it is necessary to ensure that the ablation plume from the target is well centred on the substrate. To do so, the metallic shield is attached on the heater, previously

cleaned with grit paper and acetone in the fume hood. Then, the target is ablated for about 1000 pulses, without any substrate laded, in the same O_2 pressure as planned for the deposition and at room temperature. The heater is adjusted based on the shape of the plume deposited on the shield (**Figure 3.3b,c**).

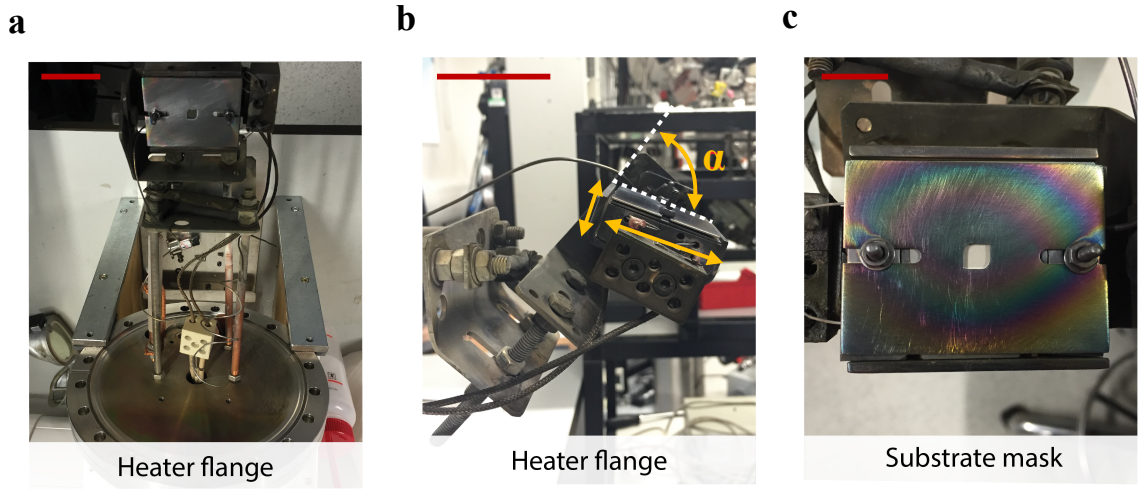

Figure 3.3 Resistive heater flange used for the PLD growth of SRO_{214} thin-films. a-c, Photographs showing the PLD flange with the resistive heater: front view (**a**), side view showing the adjustable directions with red arrows (**b**) and substrate shield (**c**). The scale bars in **a,b** correspond to ~ 5 cm and in **c,** to ~ 2 cm..

3.4.2 Target preparation

The sintered target $Sr_2Ru_{1.15}O_4$ (2.45 cm diameter), fabricated following a similar procedure as shown in **Chapter 4**, is attached to a metallic target holder using carbon tape. Before each deposition, the target surface is lightly polished using grit paper (P600) with isopropyl alcohol (IPA), then sonicated in ethanol (for 2 minutes) with only the surface is in contact with the solvent, and dried with N_2 gas.

3.4.3 Substrate preparation

The dimensions of the (0 0 1) oriented LSAT substrates are 5 x 5 x 0.5 mm^3. When the crystals have larger dimensions, they are cleaved using a pen with a diamond tip. To do so, the substrates are rested on leant-free paper with the unpolished surface facing up, and then using the diamond tip guided with a ruler, a line is drawn with the desired dimensions. Finally, the single crystal is wrapped in leant-free paper and cleaved through the line by simply applying pressure with the hands.

Before loading the substrates into the PLD chamber, they are first sonicated in acetone for 10 minutes, then IPA for 10 minutes and dried with N_2 gas. Once cleaned, they are attached to the resistive heater with a drop of thermal paste 20Ag/1Pd (ESL 9695-G) to ensure good thermal contact during the growth of the thin-film. The advantage of using thermal Ag paste

with Pd is that the melting point is shifted to 1000˚C, above the growth temperature (950˚C), which helps to prevent the contamination of the PLD chamber during the growth. Once attached, the remaining parts of the heater are covered with a metallic mask, with a gap on the substrate location, and secured with screws.

3.5 Discussion

In this study, a polycrystalline target of $Sr_2Ru_{1.15}O_4$ and *c*-axis oriented LSAT substrates are used. The starting growth conditions are set equal to those reported by J. Cao *et al*.[44] for SRO_{214} thin-films by PLD; this is a substrate temperature (*T*) of 950˚C, a laser repetition rate of 2 Hz, a laser energy of 380 mJ (4 $J \cdot cm^{-2}$), 5000 pulses, an O_2 backing flow of 7 Pa and a substrate-to-target distance of ~ 50 mm. It is worth to mention that the initial optimization of the growth conditions is done without considering the thickness of the thin films, and instead the focus is set on the reduction of the impurity phases.

3.5.1 Thin-film optimization

The effect of the O_2 pressure is studied in a range from 9.9 Pa to 0.5 Pa, with the remaining aforementioned conditions fixed. X-ray diffraction on the deposited thin-films reveals variations in the phase composition when varying the O_2 content (**Figure 3.4**). At high O_2 pressure (9.9 Pa), the thin-film composition is mainly SRO_{113} (or SRO_{4310}) and SRO_{327} phases. However, when the O_2 pressure is decreased (below 5.2 Pa), SRO_{214} phase starts to form and the impurity phases are reduced. These results corroborate that stable SRO_{214} starts to form at lower O_2 pressure than SRO_{113} and SRO_{327} as predicted from[42,58] (depicted in **Figure 3.1)**.

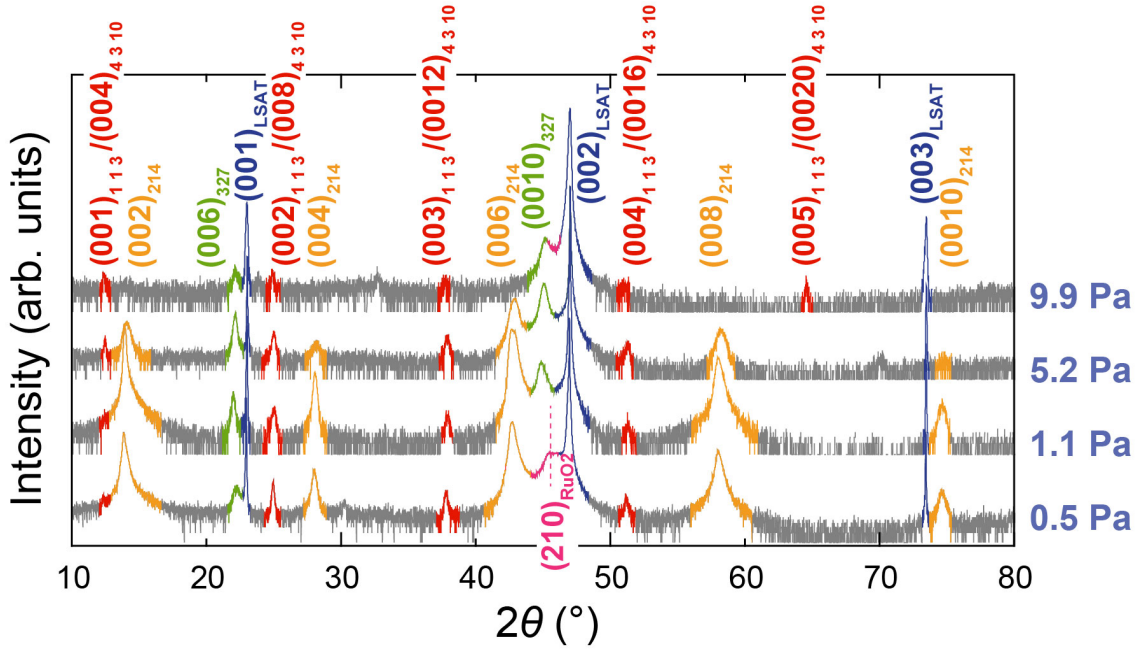

Figure 3.4 X-ray diffraction of SRO_{214} thin-films deposited at 950°C, 2 Hz, 4 J·cm^{-2} when varying O_2 pressure (9.9 – 0.5 Pa). The diffraction peaks have been indexed with the following phases: SRO_{214} (yellow peaks) SRO_{113} and SRO_{4310} (red peaks), SRO_{327} (green peaks), RuO_2 (pink peaks) and LSAT substrate (blue peaks).

Despite the X-ray diffraction pattern showing a similar phase composition at low O_2 pressure (1.1 and 0.5 Pa), the electrical characterization of the thin-films as a function of T shows different properties. In **Figure 3.5a** it can be observed that the resistance (R) normalized at $T = 300$K, as a function of T, changes from insulating to metallic when reducing the O_2 pressure, with the best results observed at 0.5 Pa (yellow curve). Accordingly, the residual resistivity ratio (RRR) increases (**Figure 3.5a inset**), indicating higher quality films with lower O_2 content. The lowest concentration of defects ($RRR \approx 3$) is observed in the film deposited at 0.5 Pa of O_2 (yellow square).

At very low T, only the thin-film deposited at 0.5 Pa of O_2, shows a downturn in $R(T)$ at 1.25 K (see **Figure 3.5b**), consistent with the onset of the superconducting transition of SRO_{214} bulk (1.5 K). We attribute this feature to incipient superconductivity since it vanishes when exposed to a field of 100 and 900 mT (**Figure 3.5b**).

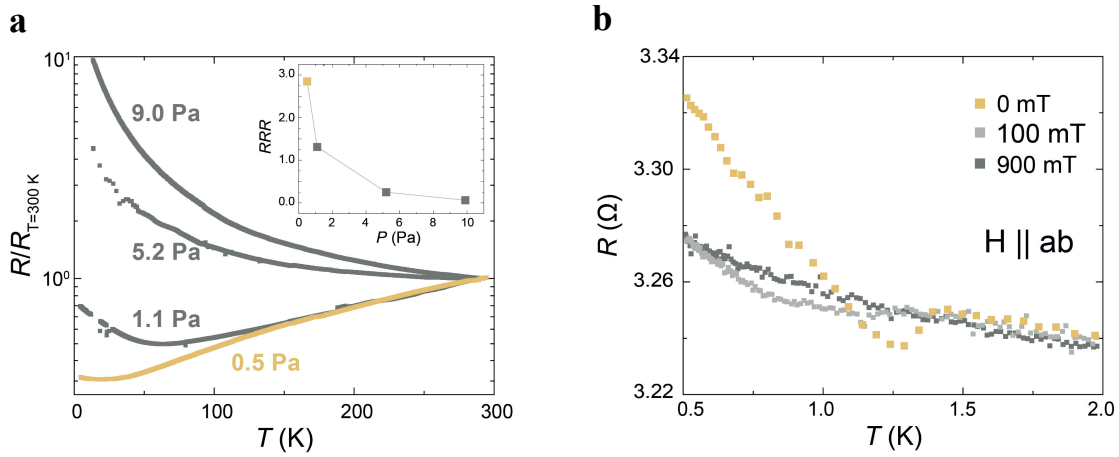

Figure 3.5 Characterization of the electrical properties of SRO_{214} thin-films deposited at 950˚C, 2 Hz, 4 J·cm^{-2} when varying the O_2 pressure (9.9 – 0.5 Pa). a, *T* dependence on the normalized resistance at *T* = 300 K when lowering the O_2 pressure (**a**), and the corresponding *RRR* (a-inset). **b,** Resistance at very low *T* of the thin-film deposited at 0.5 Pa of O_2 (yellow squares / yellow curve in **a**) and when applying an in-plane magnetic field of 100 mT (light grey squares) and 900 mT (dark grey squares).

After the O_2 optimization, the *T*-dependence is investigated on the phase composition and electrical properties of the SRO_{214} thin-films, while keeping the O_2 pressure fixed at 0.5 Pa. From the X-ray diffraction patterns, it is not observed any significant difference when decreasing the growth *T* from 950˚C to 920˚C (**Figure 3.6a**). However, the *R*(*T*) characteristic plotted in **Figure 3.6b**, show enhanced metallic behaviour in the thin-film deposited at 950˚C (depicted in yellow) and an improved *RRR* of 3 compared to the films deposited at lower *T* (*RRR* < 1) (**Figure 3.6b inset**).

Based on the above mentioned, the optimized growth conditions showing incipient superconductivity correspond to 950˚C, 0.5 Pa of O_2, 2 Hz, 380 mJ (4 J·cm^{-2}) and 5000 pulses.

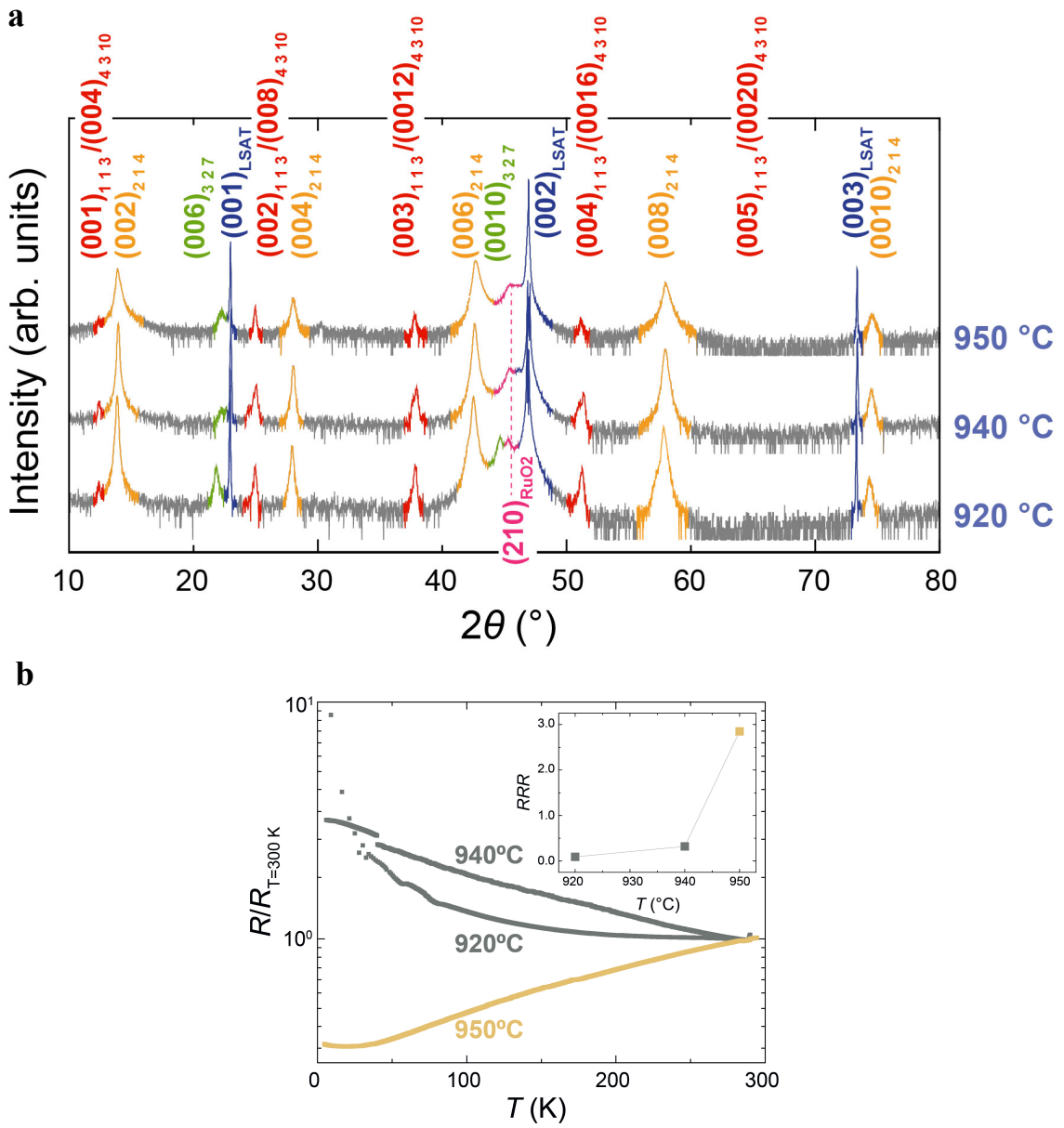

Figure 3.6 Phase composition and electrical characterization of SRO_{214} thin-films deposited at 0.5 Pa of O_2, 4 J·cm^{-2}, 2 Hz, and 5000 laser pulses, when varying the *T* (950 – 920°C). a, X-Ray diffraction patterns when varying *T*, indexed with the following phases: SRO_{214} (yellow peaks) SRO_{113} and SRO_{4310} (red peaks), SRO_{327} (green peaks), RuO_2 (pink peaks) and LSAT substrate (blue peaks). **b,** *T* dependence on the normalized resistance at *T* = 300K when lowering the *T* (**b**), and the corresponding *RRR* (**b-inset**).

3.5.2 Thin-film stability

The stability of the thin-film with the optimized growth conditions is tested by re-measuring its structural and electrical properties after several months. **Figure 3.7a** shows that the phase composition remains unchanged in the second test, compared to the first measurements.

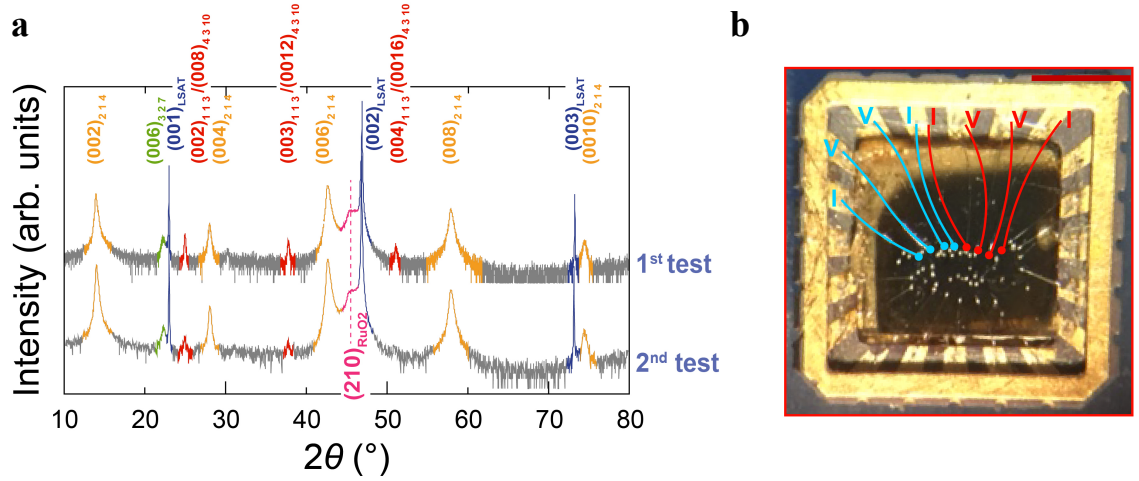

Figure 3.7 Stability test of SRO_{214} thin-films deposited at 950°C, 0.5 Pa of O_2, 2 Hz, 4 J·cm^{-2} and 5000 laser pulses. **a,** X-ray diffraction pattern of the thin-film after deposition (1st test) and after a few months (2nd test) indexed with the following phases: SRO_{214} (yellow peaks) SRO_{113} and SRO_{4310} (red peaks), SRO_{327} (green peaks), RuO_2 (pink peaks) and LSAT substrate (blue peaks). **b,** Different arrangement of the electrical contacts (blue and red) to perform $R(T)$ measurements. Only configuration in blue shows incipient superconductivity after several months, indicating non-uniform electrical properties. Scale bar in **b** corresponds to ~ 0.5 cm.

Regarding the electrical properties, the superconducting downturn in $T = 1.25$ K is also observed after the time, but it is worth to mention that it is only visible when the electric contacts are placed in the configuration indicated in blue in **Figure 3.7b**. This reveals that the thin-film is not uniform and neither its $R(T)$ characteristic.

3.5.3 Lower O_2 pressure

To enhance the phase composition and electrical properties, the O_2 partial pressure is lowered below 0.5 Pa (previously used), keeping a total pressure of 1 Pa (introducing argon) to prevent changes in the plume shape. The other growth conditions and the number of laser pulses (5k) are not altered. After decreasing the pressure to 0.1 Pa, the non-uniformity of the thin-films film becomes more visible (see photograph in **Figure 3.8a-inset**), showing different gradients of grey colour. We characterized the $R(T)$ curves of four different regions of the film indicated with coloured circles (**Figure 3.8a**). The results reveal that the region 1 (blue circle) has insulating properties, region 2-3 (pink and green circles) is more metallic than the region 1, and region 4 (purple circles) is the most insulating as the electric contacts could not be attached. Similarly, when the pressure is decreased further to 0.05 Pa, the thin-film still shows a grey colour gradient **Figure 3.8b-inset**, and the $R(T)$ characteristic is more insulating in region 1 (blue circle) than in region 2 (green circle) (**Figure 3.8b**).

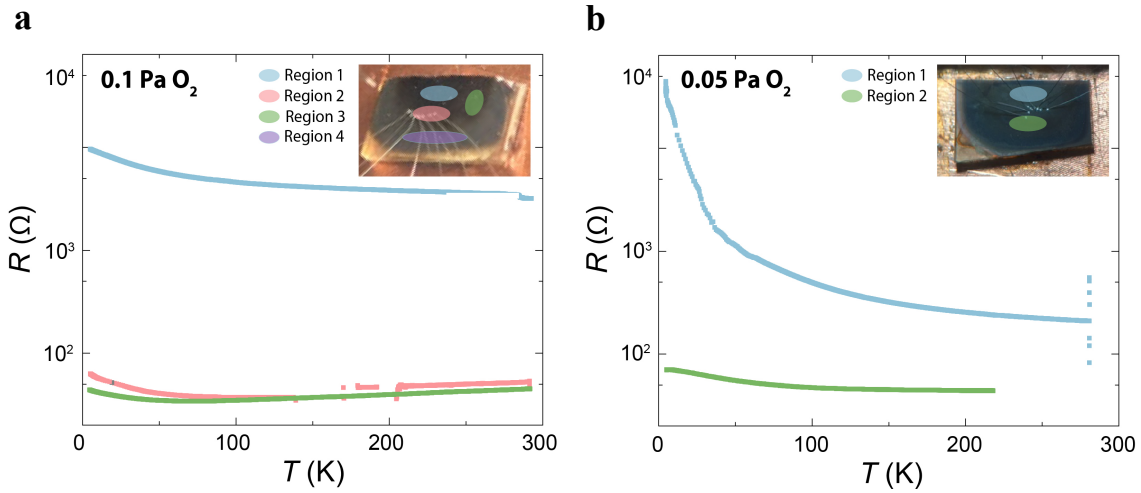

Figure 3.8 Electrical transport measurements of SRO_{214} thin-films deposited at 950˚C, 2 Hz, 4 J·cm^{-2} and 5000 laser pulses when lowering the partial O_2 pressure from 0.1 to 0.05 Pa and keeping fixed the total pressure to 1 Pa. a,b, *R*(*T*) characteristics of the SRO_{214} thin-films shown in the photography inset deposited at an O_2 pressure of 0.1 Pa (**a**) and 0.05 Pa (**b**). The coloured regions depicted on the films correspond to non-uniform parts of the films with different tones of grey, where the electrical properties have been tested. The scale bars in **a,b-insets** indicate ~ 5 mm.

An additional thin-film at 0.05 Pa of O_2 is deposited, with 1 Pa of total pressure, but this time doubling the thickness (10k laser pulses) to record its *R*(*T*) and also study the changes in the topography of the surface by AFM images. From the electric properties shown in **Figure 3.9a**, it can be observed that similar to previous results, the region 1 (blue circle) is more insulating compared to the region 2 (green circle). It is worth to mention that the values of *R* are lower than those shown in **Figure 3.8b**, which indicates fewer defects in thicker films, most likely as a result of the relaxation of the crystallographic structure when doubling the thickness. The AFM results match those extracted from the *R*(*T*) curves; the topography images of region 1 (insulating) reveal larger roughness compared to region 2 (less insulating).

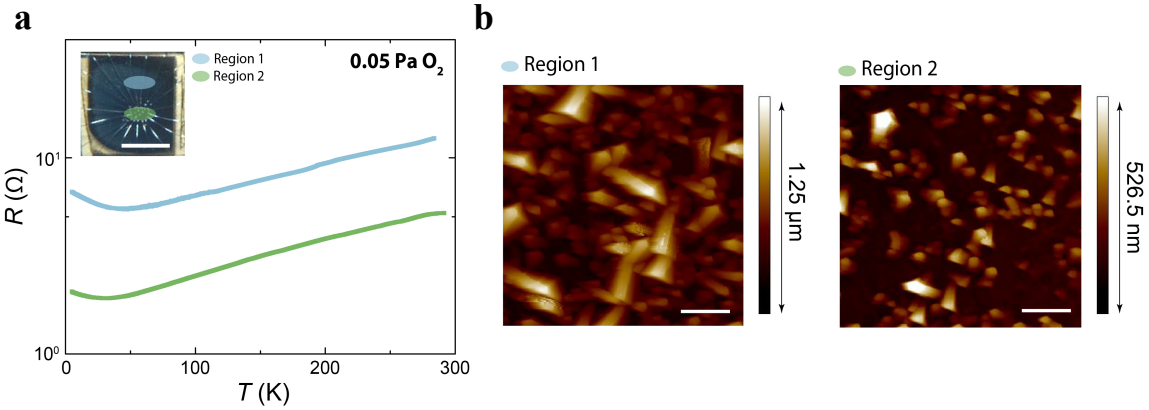

Figure 3.9 Electrical transport and AFM topography characterization of SRO_{214} thin-films deposited at 950˚C, 2 Hz, 4 J·cm^{-2}, 0.05 Pa of O_2 partial pressure, 1 Pa of total pressure and 10k pulses. a, *R*(*T*) characteristic of the regions indicated in the inset. b, AFM topography images from region 1 (blue circle) and region 2 (green circle). The scale bar in **a-inset** corresponds to ~ 5 mm and in **b**, 1 µm.

Additionally, the phase composition from X-ray diffraction patterns of the thin-films deposited at 0.5 Pa and 0.05 Pa is compared. A larger amount of the impurity phases SRO_{113} and SRO_{327} is observed when decreasing the pressure to 0.05 Pa of O_2.

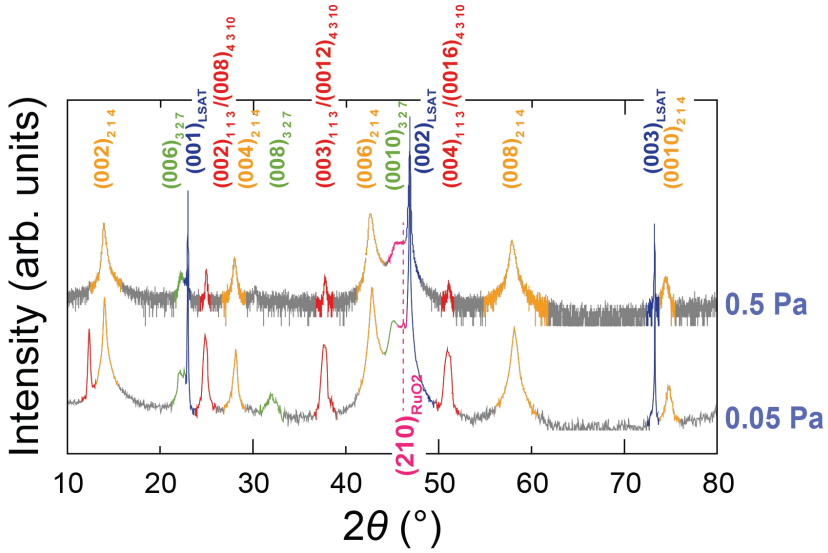

Figure 3.10 Phase composition of SRO_{214} thin-films deposited at 950°C, 2 Hz, 4 J·cm^{-2}, 5000 laser pulses, when varying the O_2 pressure from 0.5 Pa to 0.05 Pa. X-ray diffraction pattern of a thin-film deposited with a total pressure of 0.5 Pa of O_2 (top) and a partial O_2 pressure of 0.05 Pa and total pressure of 1 Pa (bottom). The peaks are indexed with the following phases: SRO_{214} (yellow) SRO_{113} and SRO_{4310} (red), SRO_{327} (green), RuO_2 (pink) and LSAT substrate (blue).

Based on the electric and structural characterization, it is concluded that lowering the O_2 pressure leads to a more stable SRO_{214} phase and enhanced electrical properties, with a limit set at 0.5 Pa of total O_2 pressure for our system. Decreasing the O_2 partial pressure further (while keeping a total pressure of 1 Pa) does not lead to further improvements in the structural or electrical properties.

From the different depositions, it also becomes evident that the thin-films have different regions that can be easily observed directly by eye, which from experimental results are correlated to non-uniform electrical properties and different topography. The cause of this gradients could be due to a non-uniform distribution of the temperature of the substrate during the growth.

3.5.4 Non-uniform heating

The temperature distribution of the PLD heater is tested by placing two different substrates next to each other on the heater, near the centre of the plume, and depositing two thin-films simultaneously (**Figure 3.11a inset**) at 950°C, 0.5 Pa of O_2, 2 Hz, 4 J·cm^{-2} and 5000 laser pulses. From the $R(T)$ characteristic, it can be observed that the sample located on the right side (grey curve) is more metallic with enhanced quality (RRR = 0.21), compared to the sample placed on

the right side (green curve) (*RRR* = 0.09). Additionally, despite of being exposed to the same growth conditions, the phase composition analysis also shows disparities between both thin-films (**Figure 3.11b**). The left-sided sample, which has worse electrical properties, also contains a larger amount of SRO_{327} when compared to the right-sided film, which has slightly better electrical properties. The possibility of the samples being exposed to different parts of the plume is excluded since it is ensured that both are located in the area corresponding to the central part of the plume.

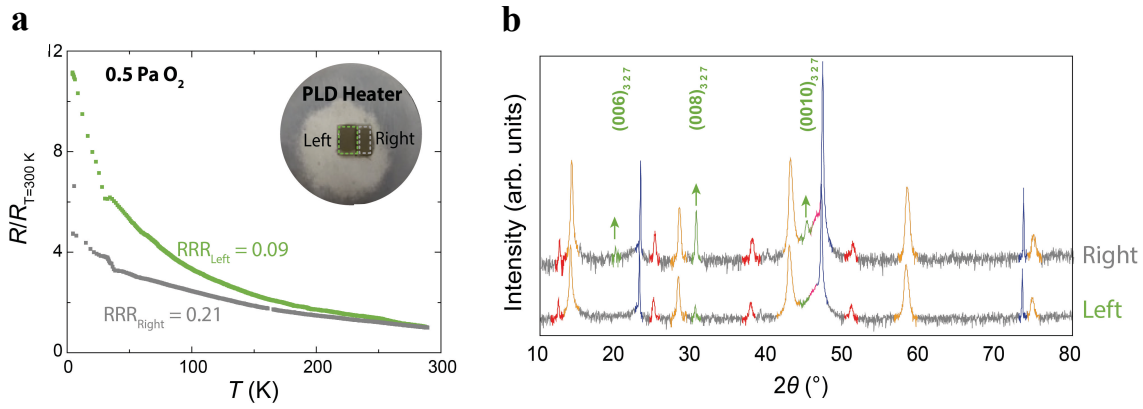

Figure 3.11 Testing the effect heater uniformity by depositing simultaneously two thin-films on two substrates placed next to each other at 950°C, 0.5 Pa of O_2, 2 Hz, 4 J·cm^{-2} and 5000 laser pulses. a, *R*(*T*) curves normalized at *T* = 300 K for two thin-films located next to each other: left (green curve) and right (grey curve). Inset shows a photograph of the PLD resistive heater and the corresponding sample arrangement. **b,** Compositional analysis by X-ray diffraction of the thin-film using the following peak indexing colours: SRO_{214} (yellow) SRO_{113} and SRO_{4310} (red), SRO_{327} (green), RuO_2 (pink) and LSAT substrate (blue).

From this experiment, it is concluded that the resistive heater of our setup is limiting the further improvement of the thin-film properties during the deposition. Based on that, the structural and electrical properties of the thin-films after the deposition are tested with different thermal annealing processes.

3.5.5 Post annealing in vacuum

The effect of thermal annealing is first tested in vacuum conditions to decrease the number of structural defects while preventing Ru loss, on the electric and structural properties of the thin-film previously described (those labelled as "left" and "right" in **Figure 3.11a**).

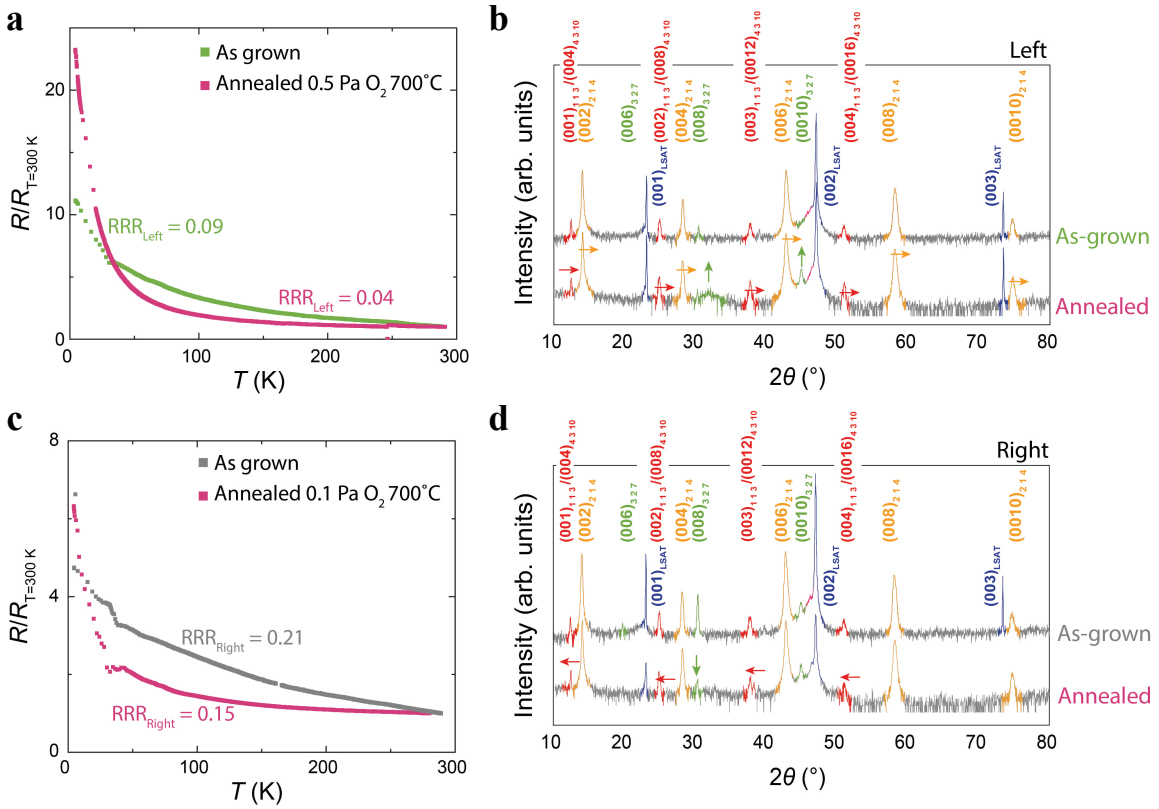

Figure 3.12 Comparison of the electrical properties and phase composition of "as-grown" SRO_{214} thin-films deposited at 950 ˚C, 0.5 Pa of O_2, 2 Hz, 4 J·cm^{-2} and 5000 laser pulses, and annealed in vacuum. a,c *R*(*T*) curves comparison of thin-films as-grown (green and grey) and after being annealed in vacuum (pink) at 700 ˚C for 20 min at 0.5 Pa (**a**) and 0.1 Pa (**c**). **b,d** X-ray diffraction pattern of the as-grown thin-film and after being annealed at 700 ˚C for 20 min at 0.5 Pa (**b**) and 0.1 Pa (**d**) with the following peak indexing colours: SRO_{214} (yellow peaks) SRO_{113} and SRO_{4310} (red peaks), SRO_{327} (green peaks).

For the post-annealing treatment, the sample labelled as "left" (green curve) is re-loaded in the vacuum chamber and exposed to 0.5 Pa of O_2, the same pressure as during the growth, and 700˚C for 20 min. The *R*(*T*) characteristic shows a lower *R* at high *T* (> 50K), but a more insulating response at low *T* (< 50K) (see **Figure 3.12a** and **Table 3.1**). The reduced value of *RRR* after the annealing process indicates that the quality of the film is not improved as expected and therefore the number of defects is not reduced.

Consistent with the reduction in the *RRR*, the comparison of the X-ray diffraction patterns after annealing shows a larger amount of SRO_{327} impurity phase (green vertical arrows) compared to the as-grown film (**Figure 3.12b**). As well, from **Figure 3.12b** it can be observed that SRO_{214} and SRO_{113} peaks shift to higher angles (horizontal yellow and red arrows), which correspond to an insignificant reduction on the *c*-axis (less than 1%) compared to the as-grown values (i.e.- SRO_{214} by 0.26% and SRO_{113} of 0.69%).

Similarly, the annealing in vacuum conditions is tested on the thin-film labelled as "right" (grey curve in **Figure 3.12c**), but this time the sample is exposed to lower O_2 pressure to prevent

the increase of the impurity phase SRO_{327}. This is 0.1 Pa of O_2 and 700˚C for 20 min. The results after annealing at lower O_2 pressure are comparable to those reported of the "left" film, with no improvement of the electrical properties and *RRR* (see **Figure 3.12c** and **Table 3.1**), besides the successful reduction of the SRO_{327} impurity phase. From the X-ray diffraction pattern, it can be observed a small shift on the SRO_{113} peaks towards lower angles (**Figure 3.12d** red arrows), which corresponds to an enlargement of the *c*-axis of 0.4% compared to the "as-grown" values, which most likely is due to Ru deficiencies[60].

Table 3.1 Values of resistance, *RRR* and the *c*-axis lattice parameter of SRO_{214} thin-films deposited at 950 ˚C, 0.5 Pa of O_2, 2 Hz, 5000 laser pulses and 4 J·cm^{-2}, "as grown" and after annealing in vacuum conditions. The values of the c-axes are extracted from the peak position of the 2theta-omega X-Ray diffraction peaks after correcting the data for sample displacement.

Thin-film (O_2 Pressure / Temperature)	**R_{290K} (Ω)**	**R_{5K} (Ω)**	***RRR* = R_{290K} / R_{5K}**	***c*-axis SRO_{214} (nm)**	***c*-axis SRO_{113} (nm)**
As grown ("left")	3022	34028	0.09	12.734	7.207
Annealed (0.5 Pa O_2 / 700˚C)	286	6552	0.04	12.700 (-0.26%)	7.155 (-0.69%)
As grown ("right")	3835	18261	0.21	12.710	7.161
Annealed (0.1 Pa O_2 / 700˚C)	154	997	0.15	12.706 (-0.03%)	7.196 (+0.4%)

The fact that no improvement on the *RRR* is observed after annealing, reflects that apart from impurity phases, Ru deficiencies might also be playing an important role in the enhancement of the electrical properties at low *T* as reported in[61].

3.5.6 Post annealing in air

Given the results after annealing in vacuum, thin-films are now annealed in air inside a crucible rich in Ru to try to improve the structural properties as well as prevent the further Ru loss.

This test is run on a new thin-film deposited at 950˚C, 0.5 Pa of O_2, 2 Hz, 4 J·cm^{-2} and 5000 laser pulses (same growth conditions as for the previous test), which is annealed in air during three different stages. The 1st stage consists of 900˚C for 12 h, the 2nd stage of 1000˚C for 12 h and the 3rd stage of 1000˚C for 24 h.

The *R*(*T*) characteristic of the "as-grown" thin-film (grey curve) shows insulating behaviour at low *T*, and a *RRR* = 0.25 (**Figure 3.13a**). After the 1st stage, there is an inflexion point making

the transition from metallic to insulating behaviour at 170 K. Also, besides the significant reduction of the *R* at high (290 K) and low *T* (5 K) (see **Table 3.2**), the *RRR* decreases to 0.07. From the X-Ray characterization, the reduction of the *RRR* could be related to the increase of the impurity phase SRO_{113}, which was already present in the "as-grown" film, but in a lower concentration (**Figure 3.13b**). The electrical properties of the thin-film after the 2nd (yellow curve) and 3rd stage (red curve), follow a similar trend, with lower *R* at high and low *T*. However, the inflexion point is shifted to 150 K and 125 K respectively, and the values of *RRR* increase, indicating an improvement in the crystallographic structure.

The peak position of X-Ray data indicates that the *c*-axis of the SRO_{214} phase slightly decreases (-0.4%) after the 1st stage, compared to the "as grown" values, and then remains constant during all the process. Whereas the *c*-axis of the SRO_{113} phase increases 2.32% with the 1st, and after the 2nd and 3rd stages is reduced a 0.84% and 0.72% compared to previous annealing stages. The initial expansion of the lattice parameter could infer that after the 1st stage there is a loss of Ru in the SRO_{113} phase, that it is later recovered; possibly due to the Ru rich crucible used. Also, it is worth to mention that the expansion of the SRO_{113} unit cell follows a parallel trend as the *RRR* values, which points at the Ru content being a key parameter on the electrical properties.

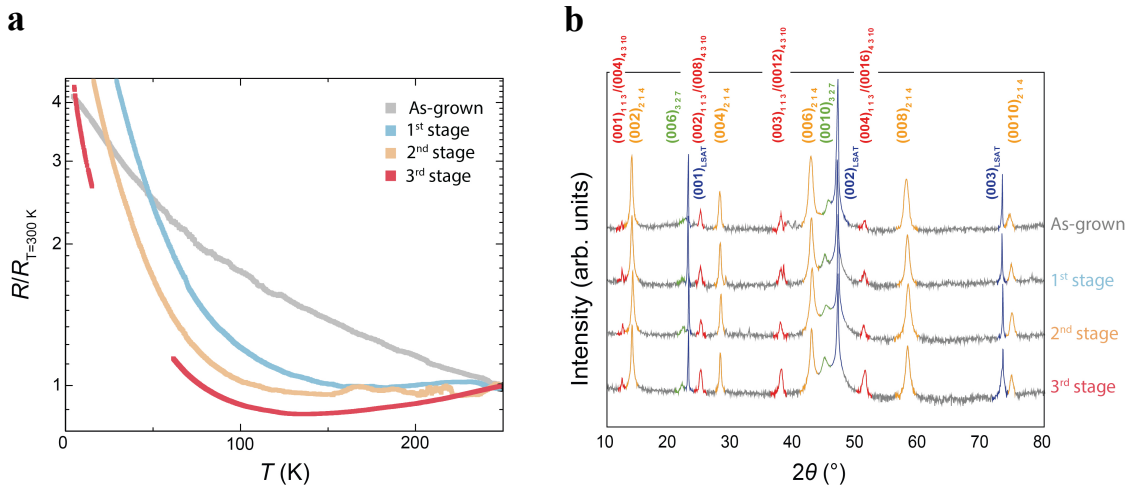

Figure 3.13 Comparison of the electrical properties and phase composition of "as-grown" SRO_{214} thin-films deposited at 950 °C, 0.5 Pa of O_2, 2 Hz, 4 J·cm^{-2} and 5000 laser pulses, and annealed in air. a, *R*(*T*) curve comparison of thin-films as-grown (gray) and after being annealed in air: 1st stage 900°C for 12 h (blue), 2nd stage 1000°C for 12 h (orange) and 3rd stage 100°C for 24 h (red). **c,d** X-ray diffraction pattern of the as-grown thin-film and after being annealed in air with the following peak indexing colours: SRO_{214} (yellow peaks) SRO_{113} and SRO_{4310} (red peaks), SRO_{327} (green peaks).

Table 3.2 Values of resistance, *RRR* and *c*-axis of SRO_{214} thin-films deposited at 950 ˚C, 0.5 Pa of O_2, 2 Hz, 4 J·cm^{-2}, 5000 laser pulses, "as grown" and after 3 different stages of annealing in air conditions. The values of the *c*-axes are extracted from the peak position of the 2theta-omega X-Ray diffraction peaks after correcting the data for sample displacement.

Thin-film	R_{290K} (Ω)	R_{5K} (Ω)	$RRR = R_{290K} / R_{5K}$	*c*-axis SRO_{214} (nm)	*c*-axis SRO_{113} (nm)
As grown	1048	4214	0.25	12.716	7.062
1st stage 900˚C 12 h	45.0	641	0.07	12.685 (-0.4%)	7.226 (+2.32%)
2nd stage 1000˚C 12 h	9.6	68	0.14	12.688 (0%)	7.165 (-0.84%)
3rd stage 1000˚C 24 h	28.5	113	0.25	12.685 (0%)	7.113 (-0.72%)

3.6 Conclusions

This chapter focuses on the optimization of the growth conditions of SRO_{214} thin-films from a polycrystalline target of $Sr_2Ru_{1.15}O_4$ on (0 0 1) oriented LSAT substrates.

Initially, it was studied the influence of the O_2 pressure in the chamber and the substrate temperature on the electrical and structural properties. When decreasing the O_2, it was possible to successfully reduce the impurity phases SRO_{113} and SRO_{327}, increase the *RRR*, and induce a more metallic behaviour at low *T*. The best results are achieved at 0.5 Pa, where a downturn in the *R* is observed near the superconducting transition of SRO_{214}. Regarding the growth temperature, below 950˚C, the *RRR* rapidly decreases suggesting a narrow window growth as previously observed by other authors.

After a few months, the stability of the structural and electrical properties was tested by re-measuring the films. The X-ray diffraction pattern and *R*(*T*) measurements confirm that there was no degradation on the quality of the thin-films. However, only when the electrodes were placed on certain parts of the film, the electrical properties could be reproduced, indicating that the thin-films are not homogeneous.

When the partial O_2 pressure was further reduced to 0.1 and 0.05 Pa while keeping fixed the total pressure in the chamber to reduce the impurity phases, the inhomogeneity of the films became more evident, with insulating regions and rough topography.

To understand if the lack of homogeneity was caused by a non-uniform temperature from the resistive heater, a test was undertaken by placing two substrates on different locations of the heater, in the centre of the plume, and depositing two thin-films simultaneously. From the

results, it was concluded that *T* plays a very important role in the growth of SRO_{214} thin-films since structural and electrical behaviour differed.

Therefore, since the electrical/structural properties were limited by the PLD system, different thermal post-annealing treatments were tested to try to improve the thin-films after the growth. The annealing processes in vacuum and air showed that the Ru content might be linked closely to the *RRR*, and besides using a special Ru rich crucible for the annealing treatment in air, the method did not succeed on improving further the electric and structural properties.

To conclude, metallic SRO_{214} thin-films have been achieved from a stoichiometric target. However, the optimization of the growth of SRO_{214} reached a limitation caused by the non-uniform heating that prevents reproducible results. Additionally, despite not succeeding with the post-annealing treatments, it was revealed the importance of Ru content when trying to achieve superconductivity.

Chapter 4

Growth of SRO_{214} Superconducting thin-films

4.1 Background

In **Chapter 3** it is investigated the growth parameters that affect the electrical and structural properties of SRO_{214} thin-films. Although the impurity phases are reduced and the residual resistance ratio is enhanced, the structural and electrical properties cannot be improved further. As a consequence, a superconducting transition is not achieved with impurities phases such as SRO_{113} and SRO_{327} still present. In this chapter, further enhancements are implemented by systematically examining the target material and substrate properties.

Until now, other reported attempts to grow SRO_{214} thin-films by pulsed laser deposition (PLD) have been followed, using a sintered (polycrystalline) target[43,44] of SRO_{214}. However, it is considered that sintered targets are limiting the quality of the resulting thin-film (i.e a low-density target leads to increased particulates and roughness[15], and the multi-grain structure could introduce misoriented crystalline regions on the film). Therefore, it would be beneficial the use of an alternative target consisting of a single crystal.

When selecting the stoichiometry of the single crystal target, it should contain excess Ru to minimise its deficiency in the resulting SRO_{214} thin-film (refer to the Background section in **Chapter 3**). Two alternative stoichiometries are considered: $Sr_3Ru_2O_7$ (SRO_{327}) single crystals with 33% excess Ru, and the eutectic phase of SRO_{214}, which would provide additional Ru via

inclusions. Based on the advantages and disadvantages of each crystalline target, one is selected to proceed with the optimization of the growth conditions.

For the substrate material, it is used (0 0 1) oriented $(LaAlO_3)_{0.3}(Sr_2TaAlO_6)_{0.7}$ (LSAT) crystals based on similar studies[43,44]. Additionally, etching the substrates before the deposition to obtain a single terminated surface could reduce significantly defects arising from the interphase, such as stacking faults[1]. However, chemical treatment on the substrates is not performed here since there is no evidence of a successful etching protocol tested on LSAT yet. Instead, the focus is set to enhance the terrace formation since the superconducting transition of SRO_{214} is suppressed when the electron mean free path is of the order of the superconducting coherence length[62] (ξ_{ab} = 66 nm). Therefore, low angle miscut LSAT (< 0.05°) is used, which results in larger terraces (> 100 nm), and additionally, a thermal treatment is applied before each deposition; which helps to improve the phase termination[63].

As an alternative, different substrates are also taken into consideration to minimize the lattice mismatch with SRO_{214}. As discussed in **Chapter 3**, attempts to use other substrates such as (1 0 0) $SrTiO_3$, (1 0 0) $LaAlO_3$, and (1 1 0) $NdGaO_3$, lead to metallic SRO_{214} thin-films at low temperatures; but not superconducting[1]. Only by molecular beam epitaxy (MBE), thin-films deposited on (1 1 0) $NdGaO_3$ show evidence of superconductivity[47]. In this chapter, two novel alternative substrates that can provide an ideal lattice matching are introduced: Sr_2RuO_4 with substitutional Ti (SRTO) and Sr_2TiO_4 (STO_{214}) crystals.

To summarize, this Chapter begins by outlining the floating zone (FZ) method, which is used to prepare SRO single crystal targets and substrates. The description is based on the knowledge I acquired during my 2 months visit to Prof. Maeno's research group at Kyoto University (Japan), where I prepared the crystalline targets and substrates. Then, the issue regarding residual impurities in SRO_{214} thin-films is discussed, and superconductivity is achieved when substituting the polycrystalline SRO_{214} target with a single crystal target of SRO_{327}. The benefits of selecting a low miscut angle LSAT and substrate thermal treatment are also reviewed together with the advantages and drawbacks of using alternative targets and substrates.

Finally, I note that the SRO_{214} thin-films characterised in this Chapter were deposited by me at the Seoul National University in Prof. Noh's laboratory, following multiple research visits.

4.2 Floating zone method

SRO single crystals are grown by floating zone method (FZ) using a two-mirror infrared image-furnace with 2 kW halogen lamps from NEC Machinery, model SC-K15HD-HP. During the FZ process, a feed rod is melted in the focal point of the lamps (molten zone) while connected to a single-crystal seed. The single crystal is continuously formed while the feed/seed are lowered and new parts of the feed melted.

In this section, the general procedure to prepare SRO single crystals is described; a detailed account is provided elsewhere [23,64,65].

4.2.1 Feed preparation

The feed is prepared from the solid solution of $SrCO_3$ powder with less than 7 ppm of Ba and RuO_2 powder with 99.9% purity to ensure high purity single crystals.

The SRO single crystal should grow from a Ru rich feed to compensate for Ru loss during the growth due to its high volatility. The initial mixture for the feed preparation of RuO_2 and $SrCO_3$ contains a nominal molar ratio of Ru to Sr ($n = 2N(\mathrm{Ru}) \,/\, N(\mathrm{Sr})$, where N(Ru) and N(Sr) are molar numbers) of n = 1.15 to achieve Sr_2RuO_4 (stoichiometric n_{stoic} = 1) and n = 1.68 for $Sr_3Ru_2O_7$ (stoichiometric n_{stoic} = 1.33).

The amount of each reactive needed for the feed rod fabrication (**Table 4.1**) is based on the chemical reactions that occur after calcination. The following corresponds to the case of SRO_{214}

$$2SrCO_3 + nRuO_2 \rightarrow Sr_2Ru_nO_{2n+2} + 2CO_2. \qquad \textbf{4.1}$$

After the FZ growth of SRO_{214}, the reaction is written considering the evaporated RuO_2 as

$$Sr_2Ru_nO_{2n+2} \rightarrow Sr_2Ru_{n'}O_{2n'+2} + (n - n')RuO_2 \qquad \textbf{4.2}$$

where $n' = n(1/L) - 1.55L$, with $L = M_{RuO_2}/M_{Sr_2Ru_nO_4}$, being the mass of the evaporated RuO_2 divided by the mass of the feed melted to form a single crystal. The modified molar ration, n', help us to understand if the initial n value used was correct.

Once the amount of each reactive is calculated, the following steps prepare the feed rod (see **Figure 4.1**):

1. dry $SrCO_3$ 500˚C for 1 hour;

2. weigh the RuO_2 and $SrCO_3$ on weight paper (do not use a metallic spoon to avoid any cross-contamination);

3. pour the weighed powders into an agate mortar (only for SRO purposes), place inside a plastic bag, flush the air inside the bag several times with N_2 and seal the bag with tape;

4. mix the materials until the white powder is not visible (~ 1 h);

5. prepare the pellet, and with the aid of a plastic stick, turn the inside of a rubber balloon out;

6. wash the inner side of the balloon with the powder mixture to avoid cross-contamination;

7. turn the balloon inside-out, fill it with the mixed powder (~ 5 g) and close with two knots;

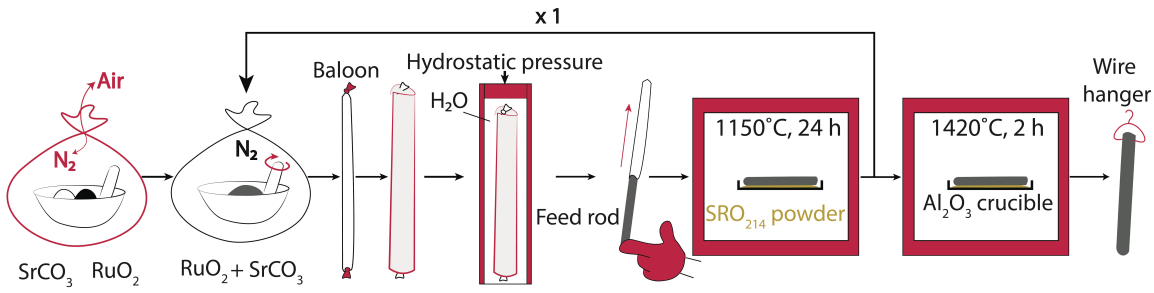

Figure 4.1 Schematic illustrations showing the steps for the feed rod preparation.

8. prepare the pellet to be pressed; attach a string to one of the extremes and insert the pellet into a paper tube (4-6 mm diameter / 100-120 mm length), which will determinate the final shape of the pellet;

9. place the pellet into a hydraulic press (Model: Nichiden SPT199-10T) and apply 1200 $kg \cdot cm^{-2}$ in water for 5 minutes;

10. after pressing, remove the paper cylinder, place the rod with the balloon on a clean surface;

11. cut one of the knots of the rubber balloon and after cutting the balloon, it will slide immediately because it was stretched, so it is important to secure the rod with a finger and avoid it from being ejected and falling apart;

12. calcinate the rod into pellets; place the rod on an alumina crucible or boat (previously coated with some SRO_{214} powder to avoid Al contamination); ramp-up to 1150˚C in air for 3 h, keep the temperature for at least 24 h, and return to room temperature;

13. crush the pellet, repeat from step 5 onwards; re-sinter ramping to 1420˚C in air during 4 h, keep for 2 h to evaporate the CO_2, and return to room temperature.

Table 4.1 Calculated values of the required amount of RuO_2 and $SrCO_3$ powder for the feed fabrication of SRO_{214} and SRO_{327} single crystals. Molecular weight considered Sr = 87.62(1) g/mol, Ru = 101.07(2) g/mol, O = 15.9994(3) g/mol and C = 12.0117 g/mol.

	n_{stoic}	n	Compound	Molecular weight (g / mol)	Weighted amount (g / mol)	Amount /g RuO_2 (g / g_{RuO2})
$Sr_2Ru_nO_4$	1	1.15	RuO_2	133.068	153.028	1
			$SrCO_3$	147.629	295.258	1.929
$Sr_3Ru_{(3n/2)}O_7$	1.33	1.68	RuO_2	133.068	335.331	1
			$SrCO_3$	147.629	442.887	1.320

4.2.2 Seed preparation

The seed is a single crystal with the required (final) orientation, which is attached to a ceramic holder during the FZ growth to ensure the right alignment (see **Figure 4.2a**).

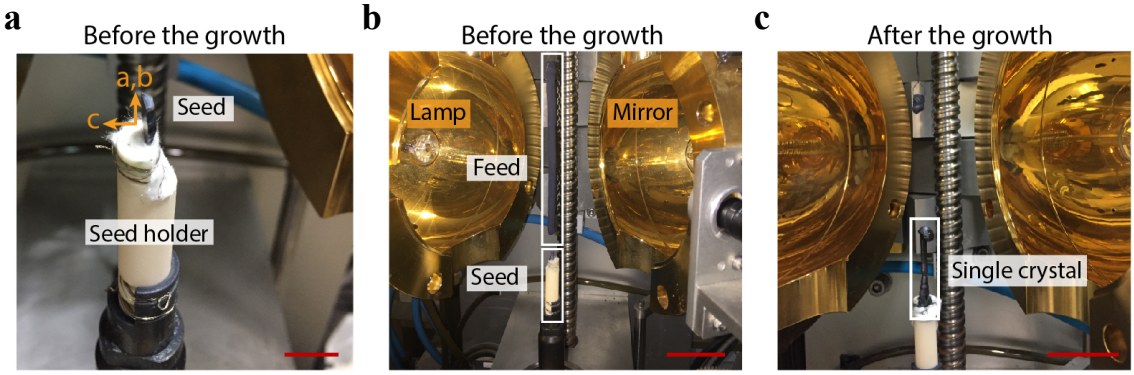

Figure 4.2 Photographs showing the floating zone system preparation before and after the growth of single crystals. a, View of an SRO_{214} seed mounted on the holder (orange arrow indicates crystallographic orientation). **a, b,** Setup of the feed and seed before growth (**b**) and the resulting SRO_{214} single crystal (**c**) after the growth. The scale bar in **a**, corresponds to ~ 1 cm, and in **b,c**, to ~ 5 cm.

4.2.3 Single crystal growth

Initially, the seed is located at the bottom of the FZ furnace and the feed is suspended from a wire (**Figure 4.2b**). Before the growth, they must be well aligned to ensure later a successful

connection while spinning on different directions (~ 33 rpm). Once adjusted, feed and seed are enclosed in a quartz tube and filled with a mixture of Ar and O_2 gas. Then it is set the pressure (P), the composition of the gas mixture and the speed of the seed (V_1), which determines the crystal growth speed.

During the single crystal growth, the voltage of the halogen lamp is regulated to control the temperature at the focal point (molten zone), together with the speed of the feed (V_2). Initially, the feed is lowered and its temperature increases as it gets closer to the molten zone, where the tip melts above 2000˚C. At this point, the seed is raised to connect to the melted tip of the feed, and when the connection is stable the rotation of the seed and feed about their axis in opposite directions is started. The single crystal starts to form and by pulling the seed and feed down, the feed continues melting and the single crystal already formed cools down as it leaves the molten zone (**Figure 4.2c**).

Table 4.2 Summary of the growth conditions for different single crystals of the SRO family. (From [65]).

	Sr_2RuO_4	$Sr_3Ru_2O_7$	$Sr_3Ru_2O_7$
n	1.15	1.55	1.68
V_1 (mm/h)	45	20	15
Atmosphere content	$10\%O_2+90\%Ar$	$100\%O_2$	$10\%O_2+90\%Ar$
Pressure P (bar)	3	10	10
ρ_{res} (μΩcm)	~0.2	~2.0	0.25
Mass loss L (%)	6.0%	10.3%	10.5%
n'	0.99	1.23	1.33

4.2.4 Caution and cleaning

To minimize the cross-contamination with other materials during the single crystal fabrication, a dedicated agate pestle/mortar and furnace are used for SRO fabrication. Before adding the powders, the pestle and mortar are wiped with ethanol, then washed with 3% of hydrochloric acid and rinsed in water. The moisture is wiped with lint-free paper and washed once again with ethanol.

4.2.5 Cutting the single crystal into sections

The single crystal is cut into sections to ease the cleaving process. The single crystal is attached to a glass slide with glue (Model Phthalic Glue S, Nikka Seiko Co., Ltd.) and cut with a diamond saw. Finally, the glue is melted with a soldering stick, allowing the different sections to be separated. Each section is labelled with letters A-Z, starting for the seed side.

4.2.6 Cleaving the single crystal

Single crystals have to be cleaved to prepare substrates (or targets). To do so, a single edge blade is aligned parallel to the selected planes of the single crystal (in **Figure 4.3a** the (0 0 *l*) planes are selected) and then, slowly tapped on its surface while dipped in IPA. If the position of the blade is correct, small pressure should be enough to easily slide and divide the crystal into parts. As a reference, after the first cleave of SRO_{214}, the inner part of the rod becomes visible and has a specular surface, which corresponds to the (0 0 *l*) planes. Further cleaving is required until the top and bottom surfaces are flat and suitable for epitaxial growth with good thermal contact (**Figure 4.3b**).

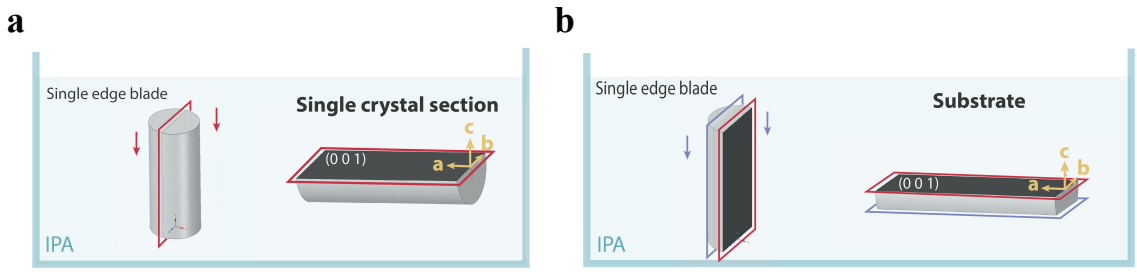

Figure 4.3 Schematic illustrations of the SRO_{214} cleaving process. a, Illustration of the first cleave from a section of a single crystal rod by inserting a single edge blade along the (0 0 *l*) plane. **b,** Further cleaving of the single crystal to prepare a suitable substrate for PLD growth. The process is carried out in a beaker filled with IPA.

4.3 Selection of the target and substrate

4.3.1 $Sr_3Ru_2O_7$ single crystal target

For the PLD growth of SRO_{214} thin-films, a set of $Sr_3Ru_2O_7$ (SRO_{327}) single crystals grown by the FZ method (at Professor Maeno's laboratory) is prepared. We first examine the crystals under an optical microscope with polarized light, looking for the lowest content of SRO_{113} impurities. **Figure 4.4a-c** shows optical images from representative crystals showing little or no SRO_{113} impurity phase (see shiny spots highlighted with pink arrows). From SEM-EDX, the Sr to Ru ratio (Sr:Ru) is 2:1.40, being the closest stoichiometry SRO_{327}, with a Sr:Ru ratio of 2:1.33 (**Figure 4.4d**). The X-ray diffraction on one cleaved crystal reveals SRO_{214} impurity phase, which is commonly observed on SRO_{327} single crystals[65]. The diffractogram matches the aimed stoichiometry, and there is an unidentified peak labelled as "*" with low intensity; close to the background level.

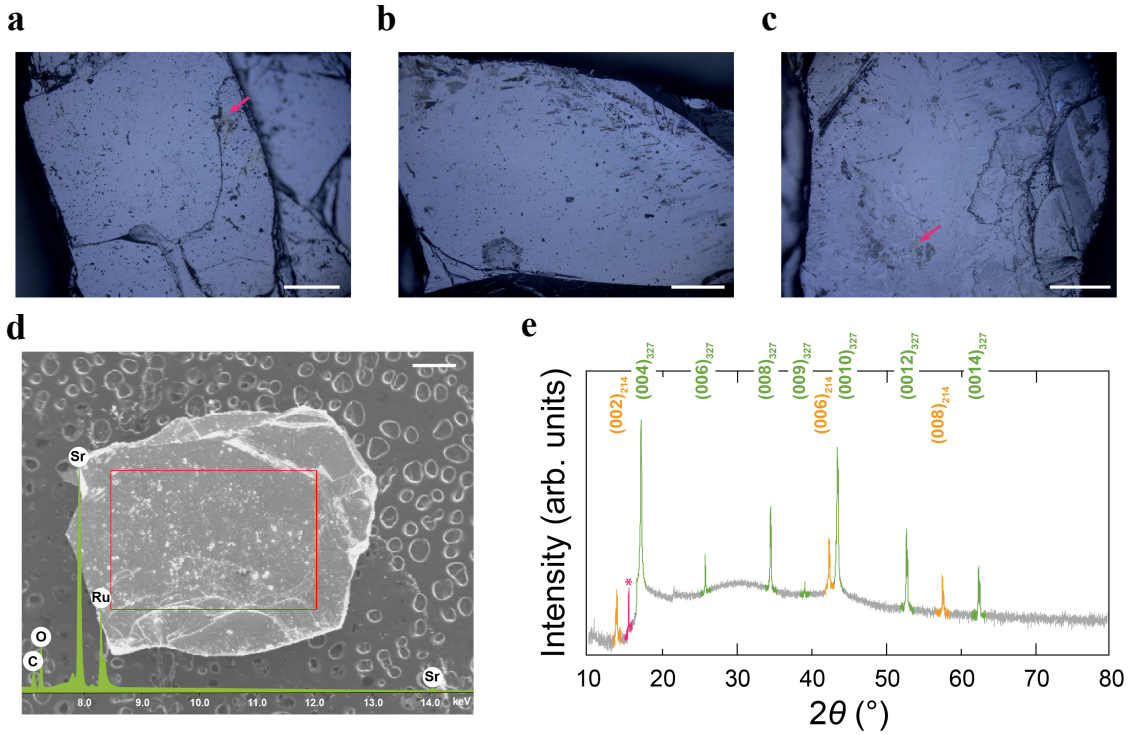

Figure 4.4 Surface characterization of an SRO_{327} single crystal. a-c, Optical images using polarized light of three different cleaved SRO_{327} single crystals from the same batch showing traces of SRO_{113} impurity phase. **d,** SEM-EDX compositional analysis confirming a Sr/Ru ratio close to SRO_{327} stoichiometry. **e,** X-Ray scan of the (0 0 *l*) diffraction peaks of a cleaved crystal indicating that SRO_{327} is the main phase (green), with traces of SRO_{214} impurity phase (yellow). There is an unidentified peak "*" (pink). Scale bars in (**a-d**) are 500 µm wide.

4.3.2 Eutectic SRO_{214} single crystal targets

Eutectic SRO_{214} single crystals are known to host Ru inclusions, which could provide the necessary excess of Ru to avoid deficient thin-films. Based on the literature and after analysing the surface of several batches under an optical microscope (**Figure 4.5**), two major disadvantages are observed. Firstly, the distribution of Ru inclusions is nonuniform (see white lines highlighted with white arrows in **Figure 4.5b,c**) and also they cannot be controlled during the fabrication of the single crystals. This would likely cause reproducibility issues on the stoichiometry of the SRO_{214} thin-films. Secondly, SRO_{214} single crystals are known to contain the impurity phase SRO_{113} (see shiny spots highlighted with pink arrows in **Figure 4.5b,c.**). Eutectic SRO_{214} is therefore not a suitable alternative polycrystalline SRO_{214}.

From now on, this chapter will focus only on the optimization of the growth of SRO_{214} thin-films using SRO_{327} single crystal targets.

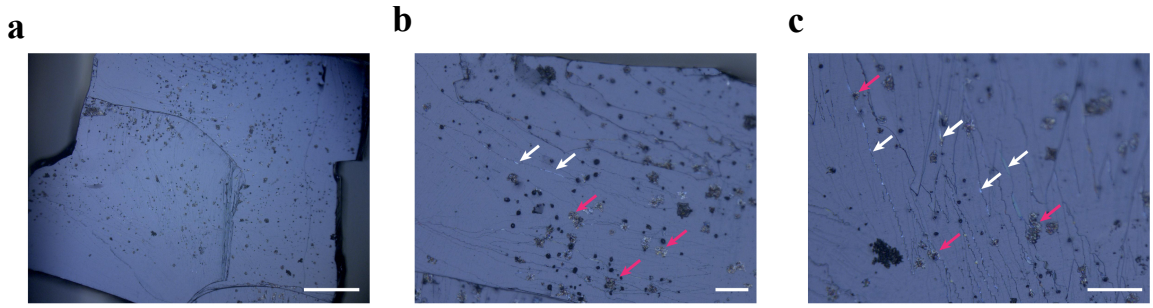

Figure 4.5 Optical microscope image with polarized light of an eutectic SRO_{214} single crystal with Ru inclusions. **a-c,** An image corresponding to a eutectic SRO_{214} single crystal (**a**) and detailed views of it (**b-c**). The white arrows indicate Ru inclusions (white lines) and the pink arrows SRO_{113} impurities (shiny spots). The scale bar in (**a**) represents 500 µm and in (**b-c**), 100 µm.

4.3.3 LSAT substrate

LSAT crystals are annealed before the deposition to treat the surface for the growth of SRO_{214} thin-films. In contrast to Sr_2TiO_4, annealing LSAT does not produce a single terminated surface. However, R. Bachelet *et al.*[63] concluded that it is possible to create an atomically flat surface with a striped pattern on LSAT by annealing in air at high temperatures (up to 1300˚C). Therefore, annealing the LSAT to promote terrace formation is tested in the main chamber in ultrahigh vacuum (0.38 Pa) for 30 min at 950˚C with an infrared diode laser heater (warming ramp rate of 50˚C·min^{-1}) before the growth of SRO_{214} films. An example of the resulting surface is shown in the AFM topography image in **Figure 4.6**, which contains steps with a height of about one unit cell of LSAT and terraces with a width larger than 100 nm.

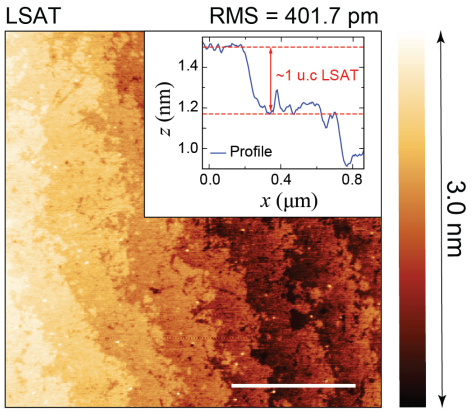

Figure 4.6 AFM topography of the surface of LSAT. The substrate has been annealed in ultrahigh vacuum for 30 min at 950˚C to promote terrace formation.

4.3.4 Alternative substrate 1 – $Sr_2Ru_{0.98}Ti_{0.02}O_4$ single crystals

The out-of-plane mismatch between SRO_{214} and LSAT may introduce structural defects in SRO_{214}. This can be overcome by depositing SRO_{214} thin-films onto lattice-matched substrates,

such as non-superconducting crystals of SRO_{214}. The SRO_{214} substrate must be non-superconducting to be able to isolate the electrical properties of the SRO_{214} thin-films deposited onto them. Insulating behaviour is ideal over metallic to eliminate the proximity effect between the SRO_{214} thin-film and the SRO_{214} substrate (which would reduce the critical temperature for the superconductivity of SRO_{214}). Insulating $Sr_2Ru_{0.98}Ti_{0.02}O_4$ (SRTO) crystals are achieved by doping SRO_{214} crystals during the FZ growth with 2% Ti, which substitutes Ru[62].

Following the FZ method, SRTO single crystals are prepared at Kyoto University (Professor Maeno's laboratory). An example of a resulting batch can be seen in **Figure 4.7a**, which is divided into sections (A-E). SEM-EDX scans on section E (**Figure 4.7a**) confirms the Ti content (Ti ≈ 2 %), and powder X-ray diffraction indicates that the single crystal is mainly composed by SRO_{214} phase (**Figure 4.7c**), with a non-identified peak (labelled as "*"); potentially associated to SRO_{113} impurity phase.

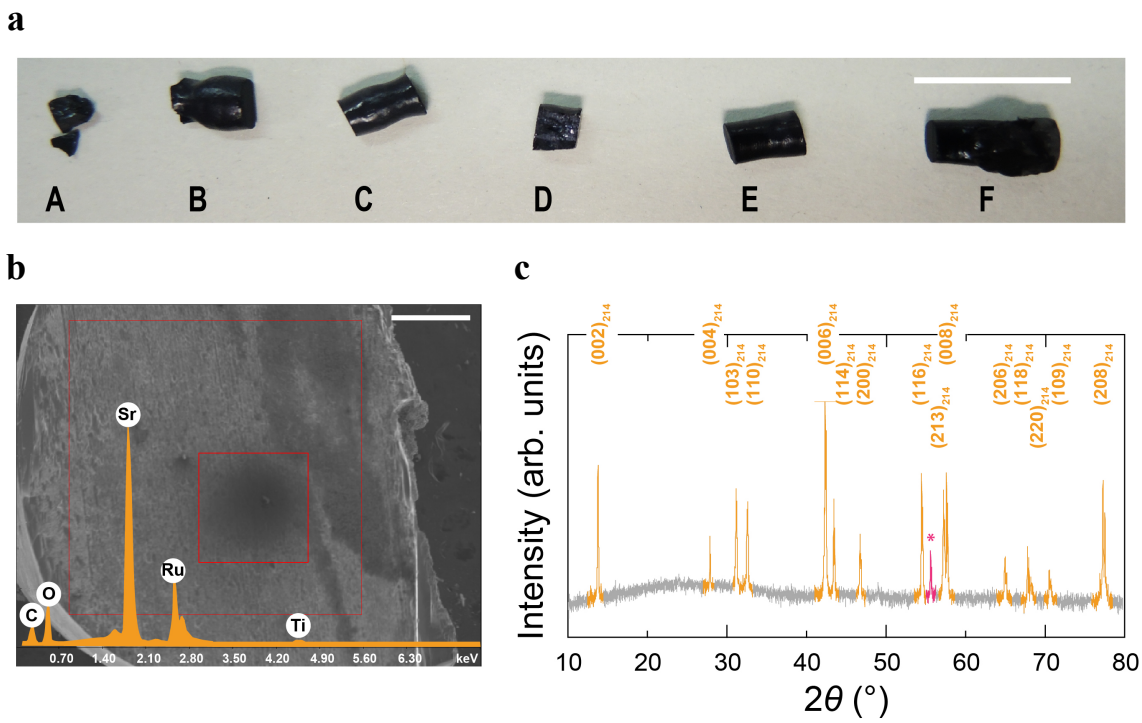

Figure 4.7 $Sr_2Ru_{0.98}Ti_{0.02}O_4$ single crystals fabricated using the FZ method. a, Photographs of the single crystal rods divided into sections, from the seed to the feed, A-F respectively. **b,** SEM-EDX analysis on section E confirming 2% of Ti content. **c,** X-ray powder diffraction on section E confirming SRO_{214} single phase. The scale bars in **a,b** correspond to 1 cm and 500 μm respectively.

4.3.5 Alternative substrate 2 – Sr_2TiO_4 single crystals

Sr_2TiO_4 (STO_{214}) crystals could be a suitable substrate for the growth of SRO_{214} thin-films based on the good lattice matching with SRO_{214} and the absence of superconducting properties, but inconveniently only polycrystals are available.

However, during the progress of this PhD thesis, single-crystalline domains have been achieved on polycrystals by Prof. Maeno *et al*. The **Figure 4.8a-c** shows optical microscope images of three different STO_{214} substrates, with detailed images displaying the single crystalline regions (**Figure 4.8d-f** respectively). These substrates are cuts from the crystal rod with a blade in IPA since they cannot be cleaved, and one side polished to ensure good thermal contact during the deposition of the thin-film.

The fact that the oriented domains are just a small fraction in the polycrystalline substrate represents an issue for the grow epitaxial thin-films and, when trying to find the location of the crystalline region after the deposition. Moreover, the fabrication of these crystals is of extreme complexity and only a few samples are currently available. Thus, an adequate strategy is needed before carrying on with the STO_{214} substrate alternative.

Therefore, the possibility to explore the growth of SRO_{214} thin-films on STO_{214} crystals, or instead on STO_{214} epitaxial thin-films, on STO_{113} substrates[66] is open for future projects.

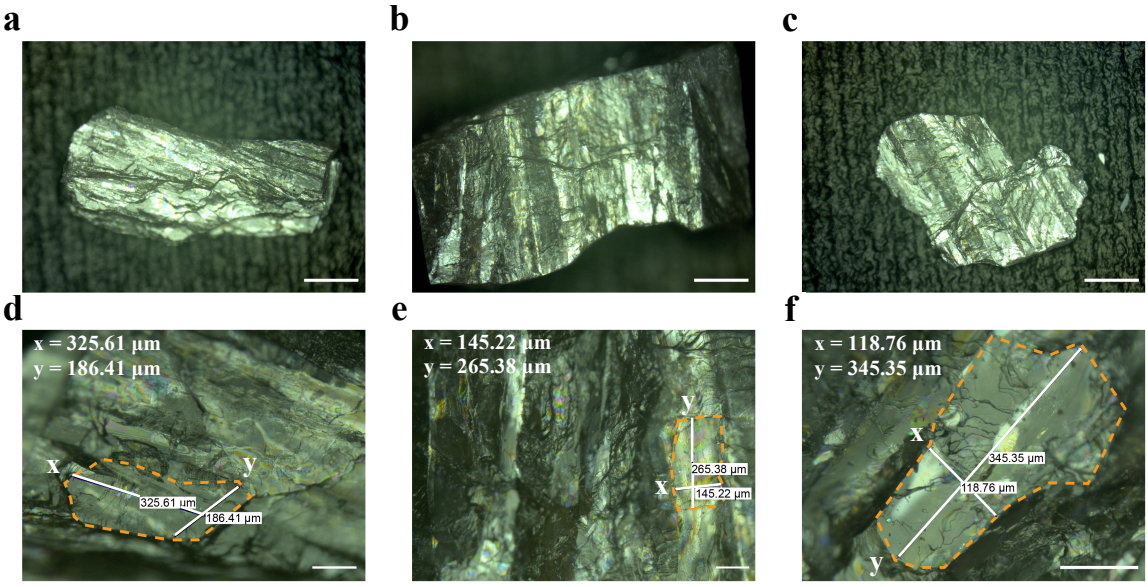

Figure 4.8 Optical microscope images of STO_{214} crystals. a-c, Images of three different STO_{214} crystals and the corresponding amplified view for each sample, (**d-f**) respectively. The area marked with a yellow dotted line delimitates single crystalline regions, and "x" and "y" the dimensions inside. Scale bars in **a-c** represents 500 µm and in **d-f** represents 100 µm.

4.4 Thin-films fabrication set up

4.4.1 Description of the PLD system

SRO_{214} thin-films are deposited with a PASCAL system at Profesor Tae Won Noh's laboratory in South Korea. During the deposition, the substrate is in thermal contact with a SiC absorber, which is heated by a diode laser able to reach up to 1000˚C. The target is mounted on a vertical configuration, located at the bottom of the chamber, which decreases the number of particulates reaching the substrate surface and helps to fabricate flatter thin-films. The system can allocate up to six targets and during the growth, the selected target can rotate about its axis to avoid overheating one spot while is ablated by a Lambda Physik KrF pulsed-laser (λ = 248 nm and spot size of 1.5 x 1.5 mm^2). For the growth of SRO_{214} thin-films, the rotation of the target is fixed, and the target carousel is twisted a β-degree to ablate the surface of the SRO_{327} single crystal along a line (**Figure 4.9**).

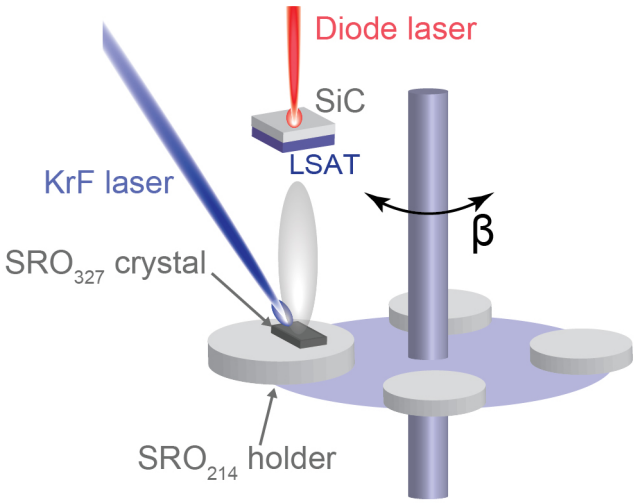

Figure 4.9 Schematic illustration of the PLD system used for growing SRO_{214} thin-films from the ablation of single-crystal SRO_{327} targets.

The laser fluence is measured with a power meter through a viewport outside the chamber by setting the laser to 10 Hz for 5000 pulses (127 W is equivalent to 0.6 $J \cdot cm^{-2}$ from previous calibrations). Before adjusting the fluence, it is required to rotate (or replace) the quartz that protects the inner part of the viewport of the incoming KrF laser since its transparency can be drastically reduced after several depositions due to the volatility of Ru.

The PLD chamber is equipped with a load-lock to avoid breaking high vacuum in the main chamber each time a new substrate is inserted. The load-lock is vented by inserting N_2 gas until atmospheric pressure is reached, which prevents moisture from attaching into the chamber walls. Every substrate ready for the deposition or replacement target loaded in the chamber, is

heated first (250˚C for 30 min) with a resistive heater to remove any organic material before being transferred into the main chamber.

4.4.2 Target preparation

Single crystalline targets of SRO_{327}, grown by floating zone method as described in (**Section 4.2**), are cleaved in isopropyl, with dimensions of approximately $3 \times 10 \times 0.5$ mm^3. The cleaved crystals are ultrasonicated in acetone (10 min), then in isopropanol (10 min) and dried using nitrogen gas. The surface of the crystals is examined under an optical microscope with polarized light to confirm a low concentration of Ru and SRO_{113} surface impurities. As shown in **Figure 4.10a**, the selected SRO_{327} single crystal is attached to an SRO_{214} polycrystalline target using Epoxy-Ag paste and cured for 30 min at 150˚C in air. This is to prevent the contamination of the chamber from other materials rather than Sr, Ru or O when aligning the KrF laser. Before loading it to the main vacuum chamber, the target (with the holder) is backed for 30 min at 250˚C in vacuum inside the load-lock.

4.4.3 Substrate preparation

LSAT substrates (from Crystech) are ultrasonicated in acetone (10 min), then in isopropanol (10 min) and dried using nitrogen gas. Then, they are attached to a SiC crystal (10×10 mm^2) with one drop of Pt paste (Tanaka Kikinzoku Kogyo K.K.) and secured with metallic clips onto the substrate holder (**Figure 4.10b**). It is important to ensure that the back of the substrate is fully covered by the Pt paste to prevent cracks during the growth due to non-uniform heating (see **Figure 4.17**). Before being loaded in the main chamber, the substrates are pre-baked for 30 min at 250˚C in vacuum in the load-lock chamber to evaporate any solvent acquired during the cleaning process or from the Pt paste.

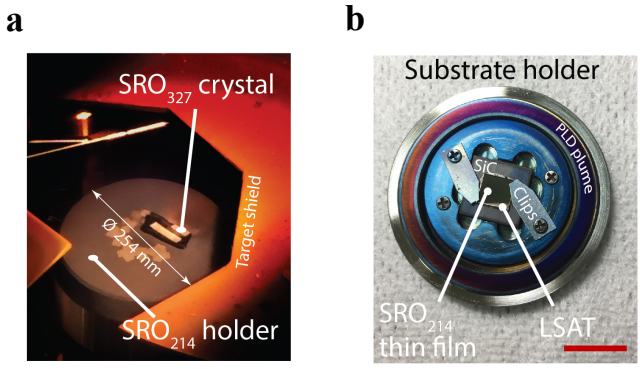

Figure 4.10 Photographs showing the target and substrate holders. a, View of the SRO_{327} single crystal target mounted on an SRO_{214} polycrystalline target holder. **b,** Substrate holder showing how the LSAT is attached to a SiC absorber and secured with metallic clips. The scalebar in **b** corresponds to ~ 10 mm.

4.4.4 Growth optimization: fluence, oxygen and temperature dependence

Due to the implementation of the SRO_{327} single crystal target and the use of a different PLD set up, the growth conditions of SRO_{214} thin-films need to be re-adjusted (oxygen pressure, laser fluence and temperature) compared to the prior growth optimization (see **Chapter 3**).

Since the starting material is an SRO_{327} target, the goal is to reduce the content of Sr, Ru and O to achieve the stoichiometry of SRO_{214} on the thin-films. The content of Sr can be reduced by increasing the pressure in the chamber; slowing down the light elements. However, the PD scaling law (Pressure x Distance = constant) introduced by H. S. Kwok *et al.*[67] demonstrates on YBCO thin-films deposited by PLD, that there is an empirical correlation between the target-substrate distance and the pressure in the chamber related to the plasma properties of the plume. Therefore, since our new set up configuration has a larger target-substrate distance, the O_2 pressure should be reduced to achieve a similar speed of the ablated material. Therefore, the first experiments consist of decreasing the pressure from 1 to 0.09 Pa, which also helps to decrease the O_2 content.

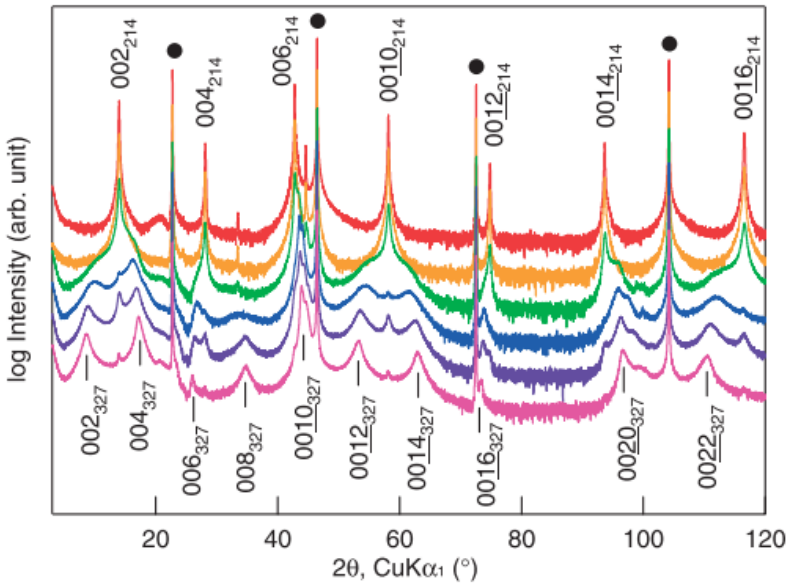

Figure 4.11 X-ray diffraction pattern showing the effect of reducing laser fluence on the variation of the final stoichiometry of thin-films from SRO_{327} to SRO_{113}. Sr_2TiO_4 substrate peaks are marked with "•", and fluence values in ascending order are 0.43, 0.43, 0.67, 0.92, 1.42 and 2.08 $J \cdot cm^{-2}$. (From [68]).

Complementary, the selection of the laser fluence it is based on a study performed by T. Ohnishi *et al.*[68]. They showed that changes in the laser fluence can modify the final stoichiometry of the resulting thin-films; from SRO_{214} to SRO_{327}; when using an SRO_{113} target (poly-crystal) for all the depositions. At a high laser fluence (2.08 $J \cdot cm^{-2}$) the resulting thin-film is mainly composed by SRO_{327} phase, whereas a continuous decrease in the laser fluence

reduces the fraction of SRO_{327} and promotes the growth of SRO_{214} until reaching single-phase films (0.43 J·cm^{-2}) (see **Figure 4.11**). Based on that, here it is studied the range from 1.40 to 0.75 J·cm^{-2}.

Following previously reported results on PLD, there is a narrow growth window for the growth of stable SRO_{214}[43] thin-films that constrains the range of temperatures available. Based on the limitations, SRO_{214} thin-films are deposited between 950˚C and 1050˚C to ensure the stabilization of SRO_{214} single-phase and high-quality thin-films.

4.5 Discussion

The optimization begins with the adjustment of the O_2 pressure while depositing SRO_{214} thin-films at 950˚C by PLD with a laser fluence of 1 J·cm^{-2}, a repetition rate of 2 Hz, 5000 pulses (t ≈ 23 nm) and a substrate-to-target distance of ~ 50 mm. X-ray diffraction of the (0 0 l) planes in a 2θ-ω scan (**Figure 4.12a**) shows epitaxial and c-axis oriented growth. Thin-films deposited at high O_2 pressure (1 Pa) have an additional phase, attributed to SRO_{327}. This can be observed from the splitting of the diffracting plane $(0\ 0\ 8)_{214}$, into $(0\ 0\ 12)_{327}$ and $(0\ 0\ 12)_{327}$. Thin-films deposited at lower O_2 pressure (0.35 Pa) show no traces of impurity phase and sharper peaks, indicating less structural defects, i.e. large microstrain and small crystallite size out-of-plane, and thickness fringes, indicating higher quality films. When the O_2 pressure is further decreased (0.09 Pa), the X-ray data shows an additional diffraction plane, marked as ”*”, which could belong to a phase from the Ruddlesden-Popper family, i.e. $(0\ 0\ 10)_{327}$, $(0\ 0\ 14)_{4310}$ or (2 1 0) diffraction plane of RuO_2, and wider peaks.

Given the narrow growth window of O_2 pressure, 0.35 Pa is selected to study the dependence of the laser fluence on the phase composition, keeping fixed the remaining growth conditions (950˚C, 2 Hz, 5000 pulses) (**Figure 4.12b**). X-ray diffraction of thin-films deposited at high laser fluence (1.40 J·cm^{-2}) shows broad diffraction peaks, indicating localized strained regions or small crystallite size in the out-of-plane direction. The structural properties of the thin-films improve when the fluence is decreased (1.00 J·cm^{-2}) since the peaks get shaper and thickness fringes become visible. A further decrease (0.75 J·cm^{-2}) also shows improved structural properties, and additionally, a small shift of the peaks towards higher angles, meaning the shrinkage of the out-of-plane lattice parameter, possibly due to a lower content of Sr on the film[68].

We now discuss the electrical transport properties of the thin-films previously characterised. From the temperature (T) dependence of the resistance (R) normalized at room temperature (**Figure 4.13**), only the films deposited at 0.35 Pa and 1.00 J·cm^{-2} show the beginning of a

superconducting transition (yellow plot). A closer look at its low *T* response can be observed in the inset of **Figure 4.13a,** when decreasing the applied current (300 – 3 μΩ) the onset temperature of the superconducting transition (T_c) is shifted to a higher temperature, setting the value in 0.4 K (below bulk value < 1.5 K). The other growth conditions tested show metallic behaviour down to 3 mK (grey plots).

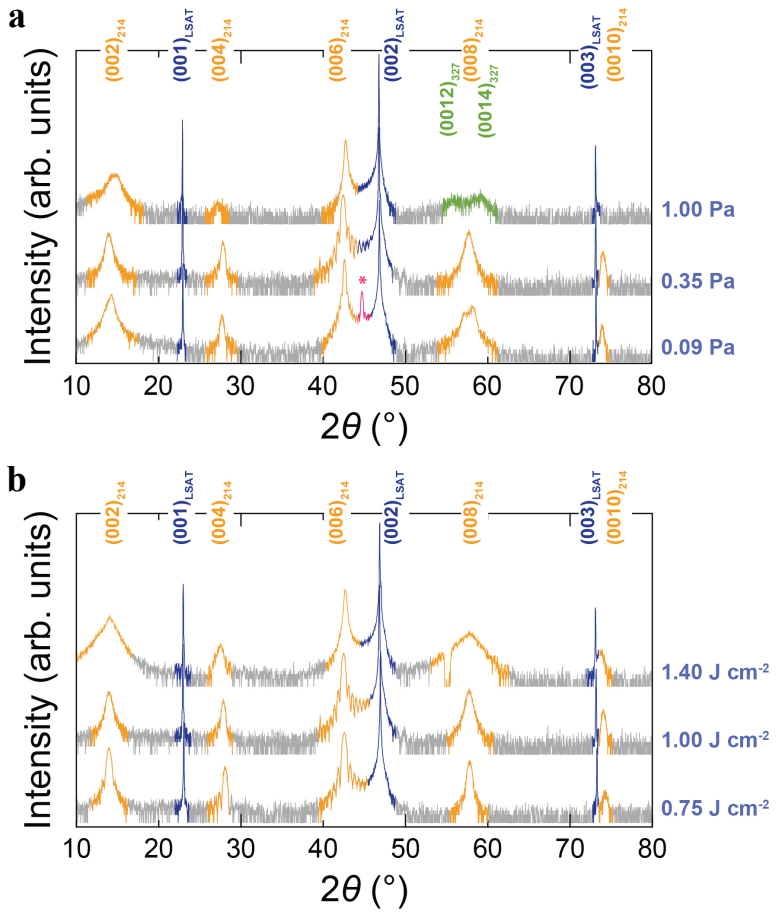

Figure 4.12 **X-ray characterization of SRO_{214} thin-films with varying O_2 pressure and laser fluence during growth when using an SRO_{327} single crystal target. a, b,** Thin-films deposited on LSAT at 950˚C, 2Hz and 5000 laser pulses (t ≈ 23 nm). **a,** Keeping a constant laser fluence of 1 J·cm-**2**, while varying the O_2 pressure (as labelled) and **b,** keeping a constant the O_2 pressure of 0.35 Pa, while varying the laser fluence (labelled). The diffraction planes for SRO_{214} (yellow) SRO_{327} (green), and LSAT (blue). The peak marked "*" corresponds to the diffraction plane of the Ruddlesden-Popper series $(0\ 0\ 10)_{327}$, $(0\ 0\ 14)_{4310}$ or (2 1 0) diffraction plane of RuO_2.

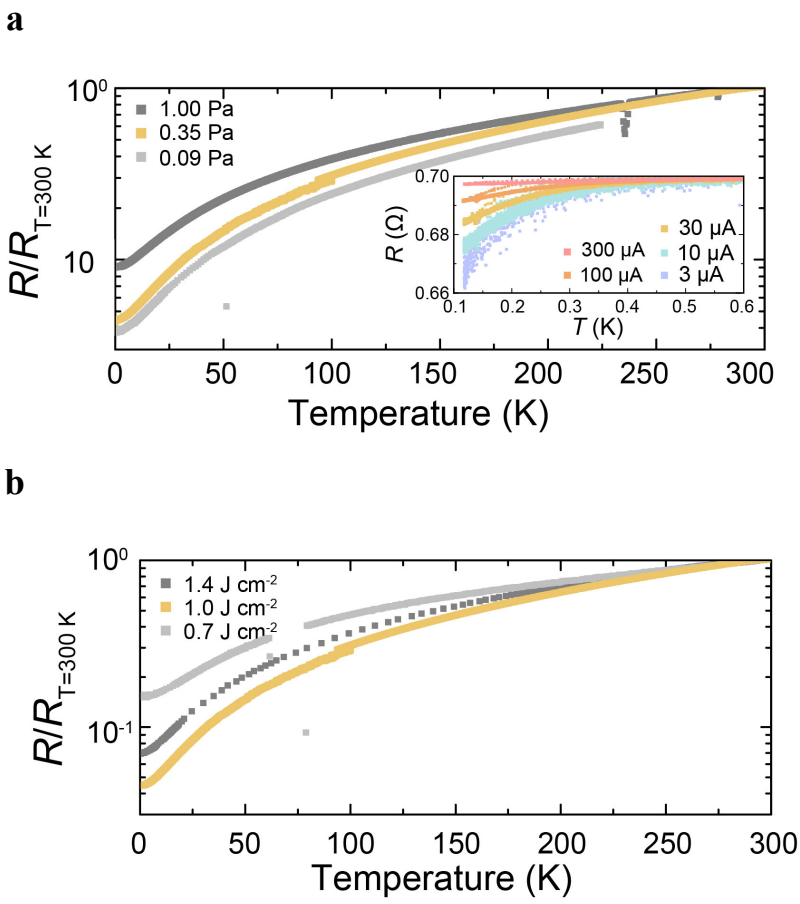

Figure 4.13 Electric transport of SRO_{214} thin-films using an SRO_{327} target when varying the O_2 pressure and laser fluence. a, b, Thin-films deposited on LSAT at 950˚C, 2 Hz and 5000 laser pulses ($t \approx 23$ nm), with fixed laser fluence (1.00 J·cm^{-2}) and different O_2 pressure (**a**), and with fixed O_2 pressure (0.35 Pa) when varying the laser fluence (**b**). Thin-films with metallic properties (grey) and partially superconducting (yellow). The inset in a corresponds to the transport properties of the thin-film deposited at 0.35 Pa and 1.00 J·cm^{-2} (yellow in **a,b**) when reducing the applied current.

We also investigated the effect of *T* on the surface topography and structural properties by atomic force microscopy (AFM) and X-ray diffraction respectively. At 950˚C, only the surface of the thin-films deposited at 0.35 Pa with 0.75 J·cm^{-2} (metallic) and 1.00 J·cm^{-2} (superconducting) reveal terrace-island growth with spiral-like steps of half unit cell of SRO_{214} (**Figure 4.14a-c**), whereas at 1.40 J·cm^{-2} (metallic) the surface shows terrace-like growth. Spiral growth is indicative of threading screw type dislocations (see **Chapter 5** for additional information), and the origin of this defect could be due to the incapability to create single side terminated LSAT substrates which leads to nucleation points that promote island growth. Similarly, screw dislocations are commonly observed on YBCO thin-films[69,70] and they affect negatively the superconducting properties of the films due to flux pinning[71]. PLD studies on YBCO thin-films deposited on $SrTiO_3$ and $LaAlO_3$ substrates indicate that superconductivity is enhanced when removing this defect by increasing the substrate *T* during the deposition[72].

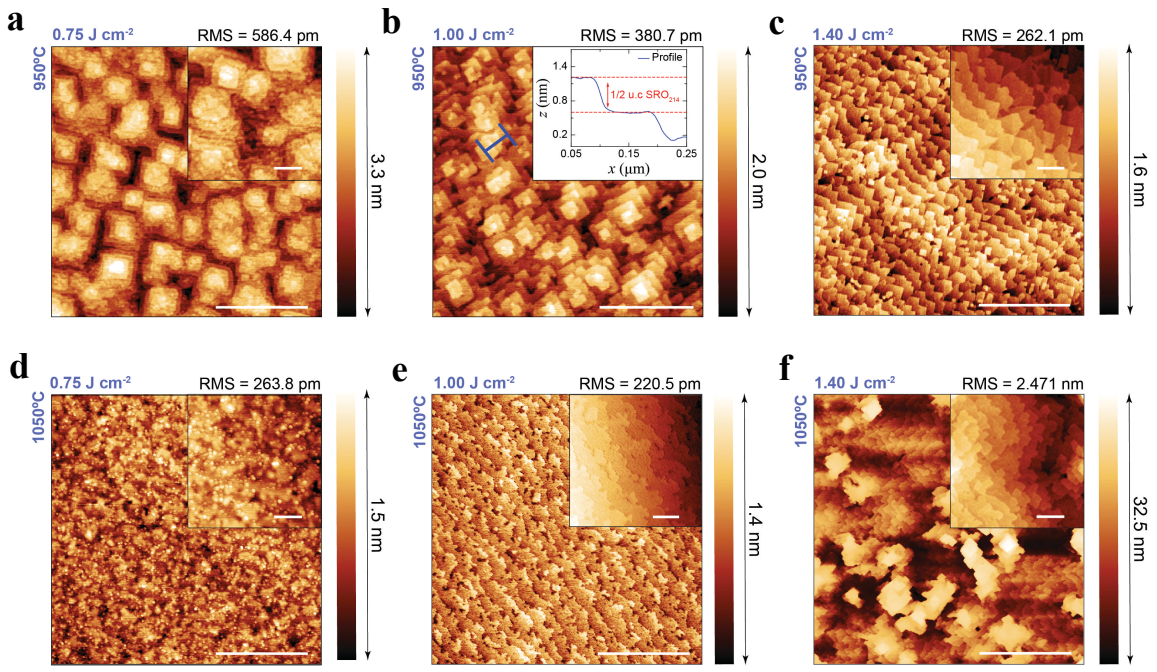

Figure 4.14 AFM topography images of SRO_{214} thin-films deposited from SRO_{327} single crystal target to study the temperature and fluence dependence on screw dislocations. AFM topography images of the surface of thin-films (3 x 3 μm) deposited at 950˚C, 0.35 Pa of O_2, 2 Hz and 5000 pulses when varying the laser fluence: 0.75 J·cm^{-2} (**a**), 1.00 J·cm^{-2} (**b**) and 1.40 J·cm^{-2} (**c**), and at 1050˚C when varying the laser fluence: 0.75 J·cm^{-2} (**d**), 1.00 J·cm^{-2} (**e**) and 1.40 J·cm^{-2} (**f**).The insets in a,c,-f are detailed topographic images (1 x 1 μm), and in **b**, the inset corresponds to the extracted height profile corresponding to the blue line. The scale bars in a-f represents 1 μm, and in the insets, 200 nm.

Since defects are one of the main suppressors of superconductivity on SRO_{214}, thin-films are deposited at a higher temperature to verify if the electric/structural properties could be enhanced. At 1050˚C, AFM on thin-films deposited at 0.75 J·cm^{-2} shows that the screw dislocations are removed, but the final result is still inhomogeneous and with percolations (**Figure 4.14a,d**). In contrast, thin-films deposited at 1.00 J·cm^{-2} show a clear enhancement of the terrace growth (without islands) and lower roughness after increasing *T* from 950˚C to 1050˚C (**Figure 4.14b,e**). Thin-films deposited at 1.40 J·cm^{-2} show a worse topography at a higher *T*; with higher roughness and inhomogeneous surface (**Figure 4.14c,f**).

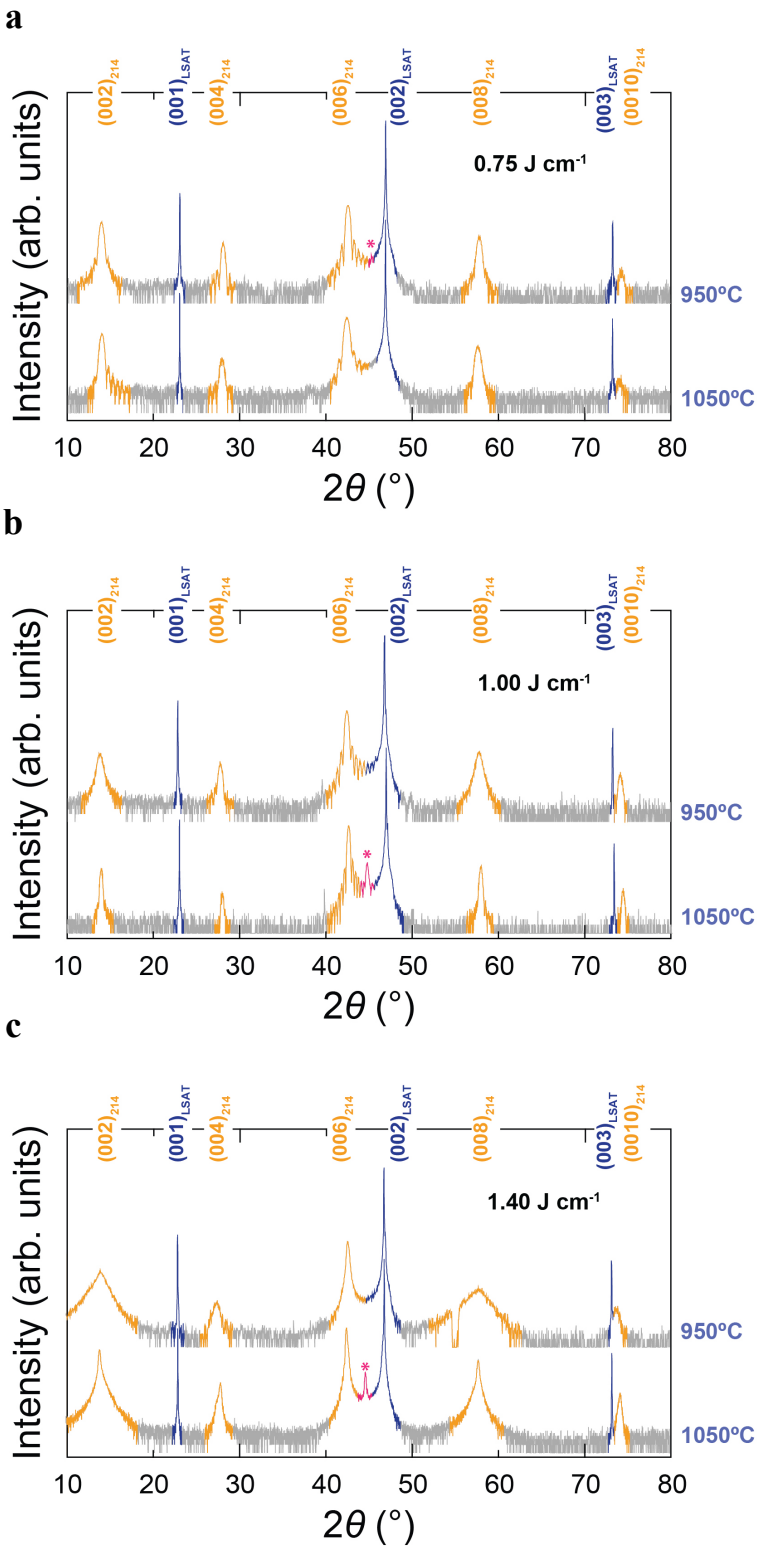

Figure 4.15 X-ray diffraction on SRO_{214} thin-films from SRO_{327} single crystal target when varying the growth temperature. a-c, 2θ-ω scan on (0 0 *l*) diffraction peaks of SRO_{214} thin-films deposited with an O_2 pressure of 0.35 Pa, a repetition rate of 2 Hz, 5000 pulses and substrate temperature of 950˚C (top) and 1050˚C (bottom) with a fluence of 0.75 J·cm^{-2} (**a**), 1.00 J·cm^{-2} (**b**) and 1.40 J·cm^{-2} (**c**). The diffraction planes for SRO_{214} (orange) SRO_{327} (green), and LSAT (blue). The peak marked "*" corresponds to the diffraction plane of the Ruddlesden-Popper series $(0\ 0\ 10)_{327}$, $(0\ 0\ 14)_{4310}$ or (2 1 0) diffraction plane of RuO_2.

The effect of increasing *T* on the phase composition and structural properties is shown in **Figure 4.15**. X-ray diffraction peaks of thin-films deposited at 0.75 J·cm^{-2} and 1.00 J·cm^{-2} are shaper when increasing *T* (**Figure 4.15a,b**); consistent with the lower concentration of screw dislocations (microstrain) observed on AFM, and larger crystallite size in the out-of-plane direction. Thin-films deposited at 1.45 J·cm^{-2} also shows shaper peaks at 1050˚C (**Figure 4.15c**), but broader than the other tested conditions and distorted (non-Gaussian or Lorentzian profile), most likely due to the presence of out-of-phase boundary defects as seen in[44], and also without thickness fringes. It is worth to mention that an additional phase labelled with "*" appears independent to the growth conditions.

The effect of *T* on the electrical properties is summarized in **Table 4.3**, which includes he contact resistance ($R_{contact}$) (measured on the surface of the thin-film with a multimeter at room temperature) and the residual resistivity ratio (*RRR*), defined as the coefficient between the resistivity at room temperature and the saturated minimum in the resistance in metallic samples or before the onset for superconducting samples. In general, at higher *T*, the contact resistance is larger and the *RRR* lower, indicating a larger amount of defects or impurities. Incipient superconductivity starting at 0.3 K is only observed on thin-films deposited at 950˚C with 1.00 J·cm^{-2}, with a *RRR* of 23, and at 1050˚C with 1.45 J·cm^{-2}, with a *RRR* of 8.54.

Table 4.3 Summary of the *T* dependence on electrical properties when using different laser fluence. *T,* indicates the temperature of the substrate during the deposition, $R_{Contact}$, is the contact resistance and *RRR*, is the residual resistivity ratio (all definitions are included in the text). *Indicates that the substrate shattered during the deposition and could not be measured.

Laser Fluence	*T* (˚C)	$R_{Contact}$ (Ω)	*RRR*	$T_{c\text{-}Onset}$ (K)
0.75 J·cm^{-2}	950	200	6.45	-
	1050	500	*	*
1.00 J·cm^{-2}	950	60	23.00	0.4
	1050	200	5.29	-
1.45 J·cm^{-2}	950	50	14.40	-
	1050	60	8.54	0.3

AFM data confirms that the variations observed on SRO_{214} topography when increasing the growth *T* are independent of the LSAT substrate since the LSAT surface remains unaltered when exposed to the temperature used during the deposition. To confirm that, a fake deposition is simulated by exposing two different LSAT substrates to 0.35 Pa O_2 for 40 minutes, at 950 and 1050˚C (including the annealing at 950˚C/30'/UHV), without depositing any material on it. In **Figure 4.16** it can be observed that the topography remains the same, with similar step size and roughness when being exposed 950 or 1050˚C.

Based on the overall analysis of structural and electrical properties, the growth conditions of the film with incipient superconductivity deposited at 950˚C (1.00 J·cm^{-2}, 2 Hz and 0.35 Pa of O_2) are optimal. Despite the film deposited at 1050˚C (1.45 J·cm^{-2}, 2 Hz and 0.35 Pa of O_2) also showing superconducting properties, the value *RRR* and T_c, larger roughness and the structural properties from X-ray demonstrate that the thin-film has poorer quality. Furthermore, working at such a high *T* introduces additional stress on the substrate which often results in the shattering of the LSAT substrate during the deposition.

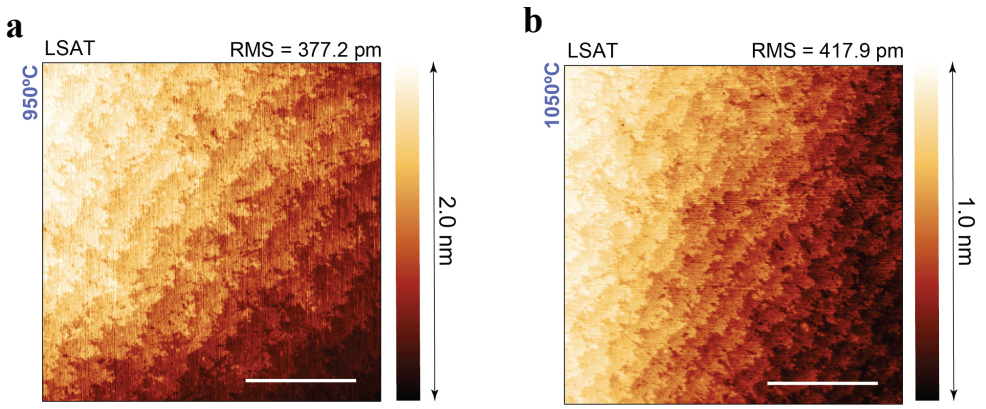

Figure 4.16 AFM topography image of LSAT substrates exposed to the same condition as during the growth of SRO_{214} thin-films. a,b, Both substrates has been pre-annealed in vacuum at 950˚C for 30 minutes before being exposed for 40 minutes in 0.35 Pa of O_2 at 950 ˚C (**a**) and 1050˚C (**b**) with no material deposited on them. Scale bar corresponds to 1 μm.

4.5.1 Caution when working at 1050˚C

One of the disadvantages when heating the substrate at high *T* for the duration of the growth (~ 1050˚C), is that the LSAT substrate ends up shattering during the deposition (**Figure 4.17**), most likely due to thermal stress. To prevent hot spots that lead to this situation, the Pt paste added between the substrate and the SiC absorber should be sufficient and uniformly distributed while keeping in mind that an excessive amount of Pt paste can contaminate the chamber environment.

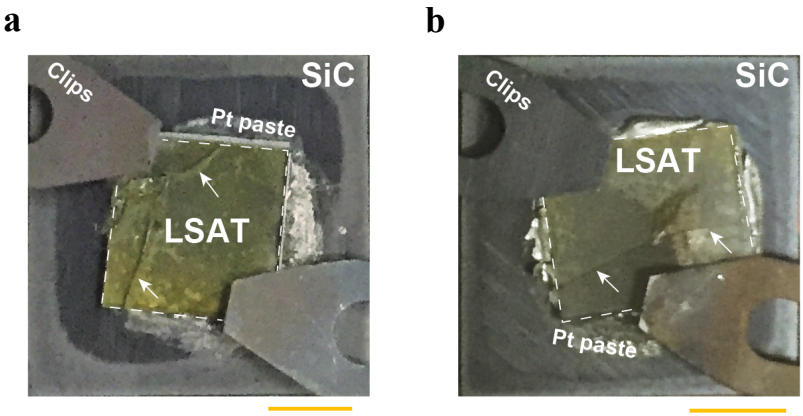

Figure 4.17 Photographs of the LSAT substrate on the substrate holder after deposition of a thin-film at 1050˚C. The substrates are attached to a SiC by Pt paste (see the excess around the LSAT). Arrows highlight cracks on the surface of LSAT caused by the high *T*. The scale bar in **a,b** corresponds to ~ 2.5 mm.

Reproducibility

We tested the reproducibility of structural and electrical properties of the thin-film grown at 950˚C, 1.00 J·cm^{-2}, 2 Hz and 0.35 Pa of O_2, by depositing an additional thin-film with matching growth conditions. From AFM topography images (**Figure 4.18**), both samples contain screw dislocations and step-growth with a half unit cell of SRO_{214} height; however, one of the samples has slightly increased roughness.

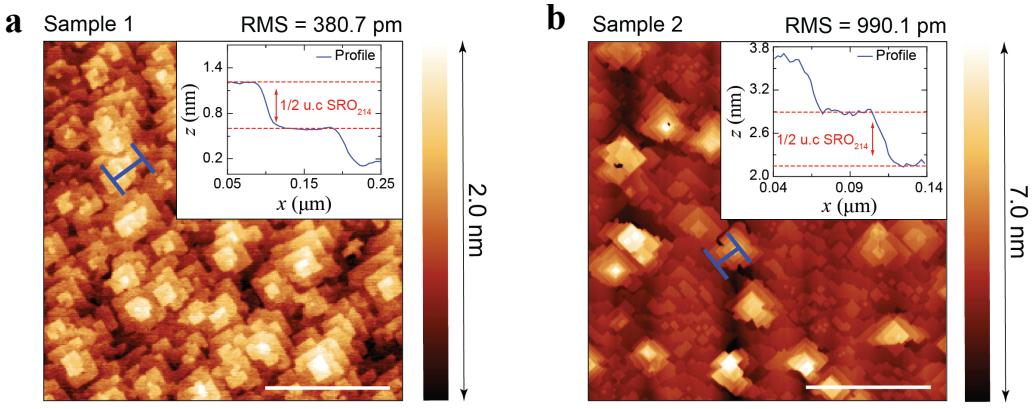

Figure 4.18 Comparison of AFM topography of SRO_{214} thin-films deposited from SRO_{327} single crystal using matching growth conditions. a,b, AFM topography images of the surface of thin-films (3 x 3 μm) deposited at 950˚C, 1.00 J·cm^{-2}, 0.35 Pa of O_2, 2 Hz and 5000 pulses showing reproducible results. The thin-films are labelled as sample 1 (**a**) and sample 2 (**b**). The inset corresponds to the extracted height profile corresponding to the blue line. The scale bars represent 1 μm.

Table 4.4 summarises the electrical properties extracted from the $R(T)$ characterization (**Figure 4.19**). Since both samples have similar $R_{Contact}$, RRR and present T_c, it is concluded that the results are reproducible within minor variations.

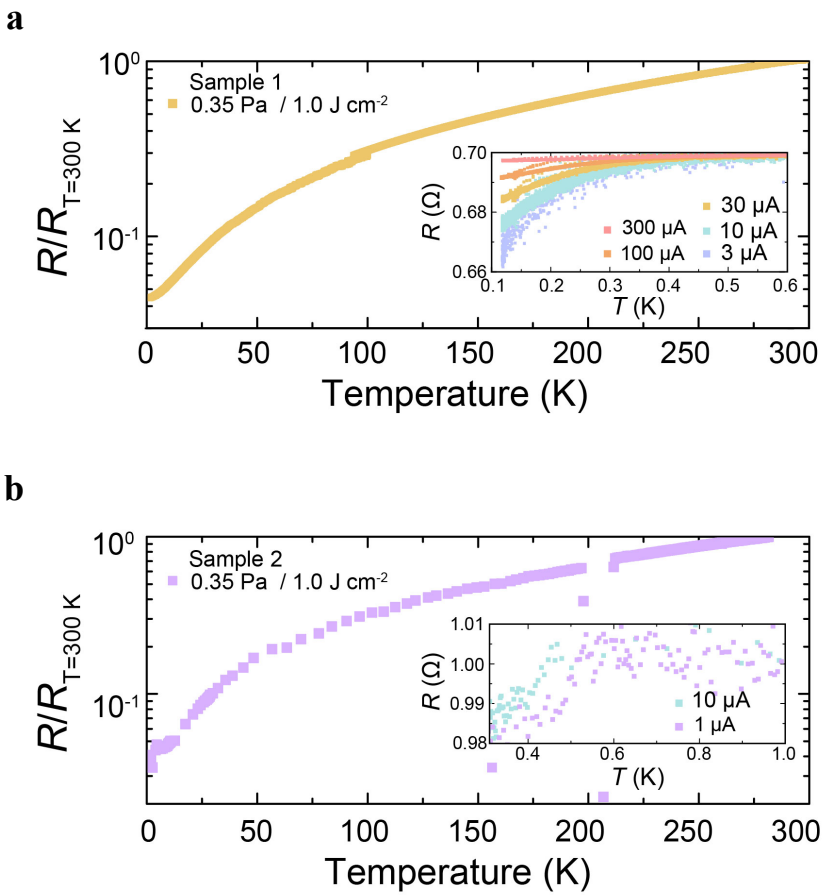

Figure 4.19 Electrical characterisation of two thin-films deposited with the same growth conditions. a,b, Temperature dependence of the R, normalized at room temperature (300 K) of thin-films deposited at 950˚C, 1.00 J·cm^{-2}, 0.35 Pa of O_2, 2 Hz and 5000 pulses. The thin-films are labelled as sample 1 (**a**) and sample 2 (**b**). The inset in **a,b,** corresponds to the resistance at low temperature when decreasing the applied current.

Table 4.4 Summary of the electrical properties of SRO_{214} thin-films deposited using the same growth conditions. T, indicates the temperature of the substrate during the deposition, $R_{Contact}$, is the contact resistance and RRR, is the residual resistivity ratio (all definitions are included in the text).

T (˚C)	Laser Fluence (J·cm^{-2})	P_{O2} (Pa)	Repetition rate / N pulses	Sample	$R_{Contact}$ (Ω)	RRR	$T_{c\text{-}Onset}$ (K)
950	1.00	0.3	2 Hz / 5000	Sample 1	60	23.00	0.40
				Sample 2	60	24.87	0.48

4.5.2 Alternative substrate 1 – Test

The suitability of $Sr_2Ru_{0.98}Ti_{0.02}O_4$ (SRTO) substrates is also tested. A thin-film of SRO_{214} of about 23nm thick is deposited using the optimized growth conditions for LSAT substrate (0.35 Pa of O_2 pressure, laser fluence 1.00 J·cm^{-2} and substrate temperature 950˚C) on one of the selected SRTO single crystals (section E).

X-ray analysis on the resulting thin-film (**Figure 4.20a**), indicates *c*-axis oriented growth of single-phase SRO_{214}. The diffraction pattern of the thin-film compared to an SRTO crystal of the same section, show sharper peaks, indicating enhanced microstructural properties (low microstrain and large crystallite size out of plane) and thickness fringes. The SRTO characterization might differ from the actual substrate used for the deposition since small differences might occur between SRTO cleaved crystals. The topography image from AFM of the surface of the thin-film reveals screw dislocations and similar roughness (**Figure 4.20a**) to SRO_{214} thin-films deposited on LSAT substrates (**Figure 4.14b**).

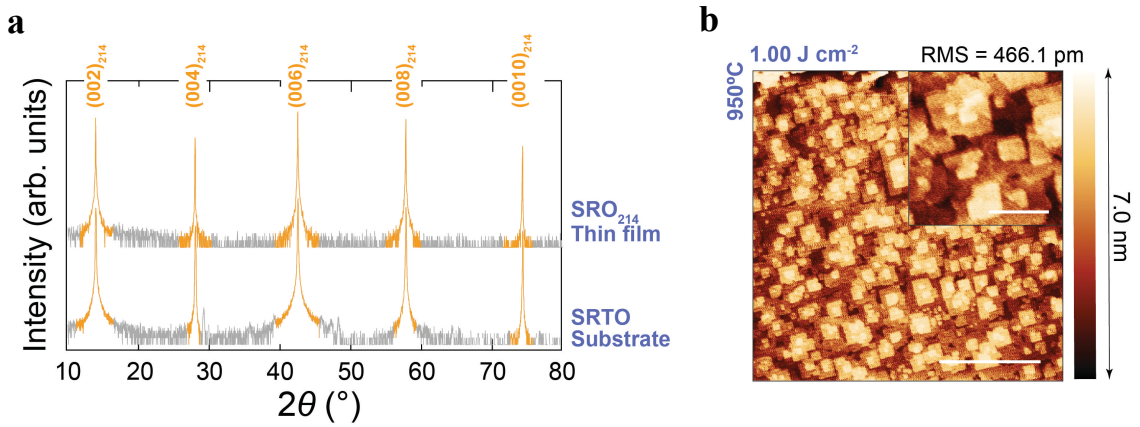

Figure 4.20 Characterization of the structural properties and surface morphology of SRO_{214} thin-film deposited on an SRTO single crystal substrate ($Sr_2Ru_{0.98}Ti_{0.02}O_4$) Ti. a,b, The growth conditions are 950˚C, 1.00 J·cm^{-2}, 0.35 Pa of O_2, 2 Hz and 5000 pulses ($t \approx 23$ nm). Comparison of the X-ray 2θ-ω scan on the (0 0 *l*) diffracting planes of the thin-film and on a cleaved single crystal of the same section as the substrate ($Sr_2Ru_{0.98}Ti_{0.02}O_4$) showing no evidence of impurity phases. **b,** AFM image of the surface (3 x 3 μm) of the thin-film showing screw-type defects. The inset corresponds to a 500 x 500 nm scan. The scale bar in (**b**) and inset correspond to 1 μm and 200 nm respectively.

The electrical characterization of the SRO_{214} thin-film deposited on SRTO single crystal does not show evidence of superconductivity down to 0.1 K (see **Figure 4.21a-b**). Regarding the structural defects, the thin-film has *RRR* of 10.30, which is higher compared to the *RRR* measured on bare SRTO single crystal used as a substrate, 4.76. However, this value is still low compared to the thin-films deposited on LSAT substrate (*RRR* ≈ 24).

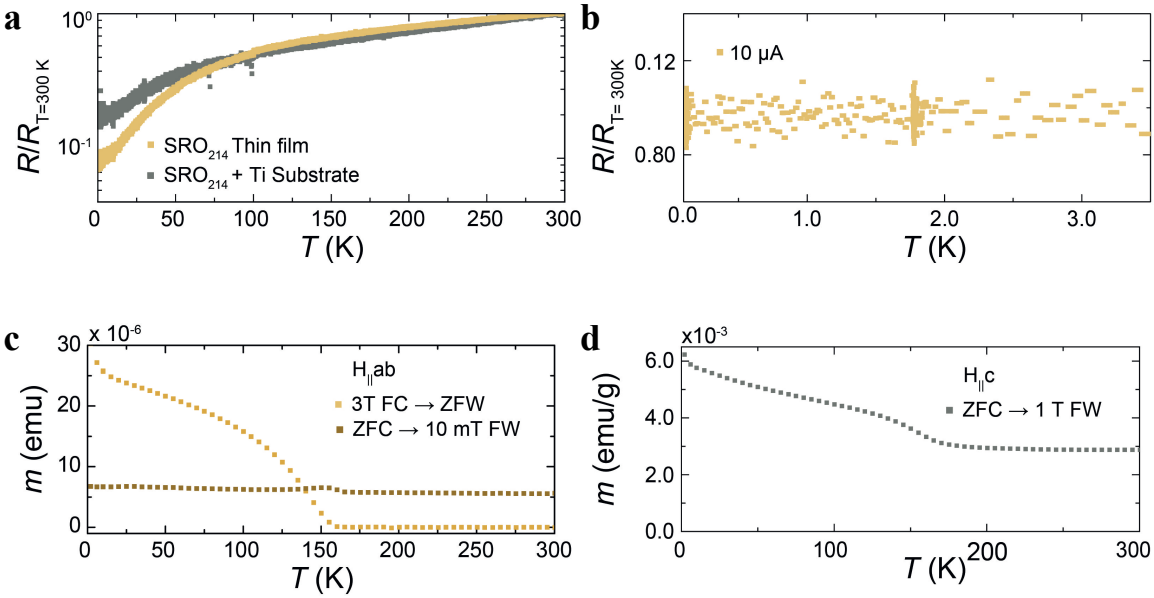

Figure 4.21 Electric and magnetic characterization of an SRO_{214} thin-film deposited on SRTO single crystal substrate ($Sr_2Ru_{0.98}Ti_{0.02}O_4$). a-c, Growth conditions are 950˚C, 1.00 J·cm^{-2}, 0.35 Pa of O_2, 2 Hz and 5000 pulses. **a,** Temperature dependence of the resistance (normalized at T = 300 K) of the thin-film (yellow) and twin substrate SRTO (grey). **b,** Corresponds to the low T normalized resistance showing no superconducting transition. **c,** Temperature dependence of the momentum of the thin-film when applying an in-plane magnetic field. Warming data in zero field (ZFW) after cooling the sample in 3 T (FC) (yellow) and warming data in 10 mT (FW) after cooling the sample in zero field (ZFC) (brown). **d** Corresponds to the $m(T)$ characteristic of SRTO (from the same batch).

We also measured the magnetic properties of the thin to confirm if there is any impurity undetected by X-ray due to a low concentration. In **Figure 4.21c-d**, the $m(T)$ curve of the thin-film shows a transition at a T_c of 160 K, most likely linked to SRO_{113}. A similar transition is also observed in the $m(T)$ characteristic of SRTO crystal (section E), indicating that it is very likely that the impurity phase is contained in the substrate and not on the resulting thin-film, also consistent with the peak labelled as "*" in **Figure 4.7c**.

Based on the results, metallic single-phase SRO_{214} thin-films can be grown successfully on SRTO single crystals with similar structural properties as observed when depositing the films on LSAT substrates. Therefore, these results open the possibility to grow SRO_{214} on a different substrate not reported previously with the optimized growth conditions. Superconducting properties can be achieved by tuning further the growth parameters.

4.6 Conclusion

We have reduced the number of residual impurities in SRO_{214} thin-films by replacing the conventionally used polycrystalline target with a crystalline target and improved the surface quality of the LSAT substrates. SRO_{327} single crystals are preferred due to their 33% excess

Ru, low concentration of impurities and higher reproducibility, which is key for maximising the reproducibility of the films. Substrates made of the eutectic phase of SRO_{214} were rejected due to the lack of reproducibility of its Ru inclusions. Additionally, annealed in-situ low angle miscut (< 0.05˚) LSAT crystals before the deposition of SRO_{214} thin-films favoured step formation. We measured a terrace width of 100 nm, which is much larger than ξ_{ab} = 66 nm in SRO_{214} and so minimises step-like defects at the interphase.

We have investigated the effect of the growth conditions (O_2 pressure, laser fluence and temperature) on the structural and electrical properties. Incipient superconductivity is achieved with an optimal value of O_2 pressure and laser fluence of 0.35 Pa and 1 J·cm^{-2} when studying the range 1 - 0.09 Pa and 1.40 – 0.75 J·cm^{-2}. With these conditions, the thin-films showed shaper X-ray diffraction peaks, meaning lower microstrain, with thickness fringes, lower defects, and low traces of impurity phases (SRO_{113} or SRO_{327}).

The evidence recorded of screw dislocations on the thin-films surface could be affecting the electrical properties. Therefore, the effect of increasing the growth temperature from 950˚C to 1050˚C to reduce the concentration of the dislocations is investigated. However, despite successfully removing the screw defects while maintaining incipient superconductivity, films deposited at 1050˚C have a higher surface roughness (RMS_{950} = 380.7 pm versus RMS_{1050} = 417.9 pm), reduced *RRR* values (RRR_{950} = 23.0 versus RRR_{1050} = 8.54) and lower T_c values ($T_{c\text{-}950}$ = 0.4 K versus $T_{c\text{-}1050}$ = 0.3 K). Additionally, the results indicate that the screw dislocations are not related to the surface structure of LSAT substrates.

The reproducibility of the selected growth conditions was tested by depositing an additional thin-film at 950˚C, 0.38 Pa of O_2 and 1 J·cm^{-2}, from which matching structural and electrical properties were obtained.

Regarding alternative substrates, the optimized growth conditions on LSAT have also been tested on $SRTO_{214}$, where metallic single-phase SRO_{214} thin-films are achieved. Single crystal targets of STO_{214} single crystals have been also prepared, however, the optimization of the growth of SRO_{214} is yet to be performed.

4.7 Future work

With the analysis performed in this chapter, we leave open the possibility to optimize further the grow SRO_{214} thin-films on $SRTO_{214}$ substrates to achieve superconducting thin-films.

Also, we prepared alternative substrates from STO_{214} single crystals, and leave open the question of how to deposit and characterise SRO_{214} thin-films on polycrystalline substrates with single-crystalline grains in the order of the micrometre scale.

Chapter 5

The origin of the suppression of superconductivity in SRO_{214}

5.1 Background

Superconductivity in SRO_{214} is characterized by a strong sensitivity to impurities and defects, which dramatically affects the critical temperature (T_c). However, in a few specific cases, crystallographic defects can enhance T_c. This section briefly reviews studies on SRO_{214} single crystals that concern defects but also highlights reports based on thin-films to analyse the reason behind the low superconducting transition temperature observed on the thin films with the optimized growth conditions (**Chapter 4**) and look for further improvements on the electrical properties.

The effect of non-magnetic impurities (Al and Si) on the electrical transport properties of SRO_{214} single crystals were investigated by Mackenzie *et al.*[6] They observed a rapid suppression of the superconducting T_c and a simultaneous increase in the residual resistivity (ρ_0) on crystals with impurity concentrations only after exceeding 50 ppm (**Figure 5.1a**). This is because Al and Si impurities are substitutional of the Ru-O conducting planes, and they contribute to the reduction of the electron mean free path of the crystal (l) by enhancing the electron scattering. The complete suppression of the superconducting transition occurs when l closely matches the superconducting coherence length (ξ_{ab} = 66 nm for SRO_{214}). Kikugawa *et al.*[62] performed a similar investigation on SRO_{214} single crystals, with other non-magnetic impurities (Ti), previously studied by Pucher *et al.*[73] (**Figure 5.1b**), and a magnetic impurity

(Ir) (**Figure 5.1d**); being both substitutional of the Ru sites. As a result, they observed that these impurities had the same effect and strongly suppressed the superconductivity, indicating that they act as strong potential scatterers as shown for the unconventional superconductor UPt_3[74].

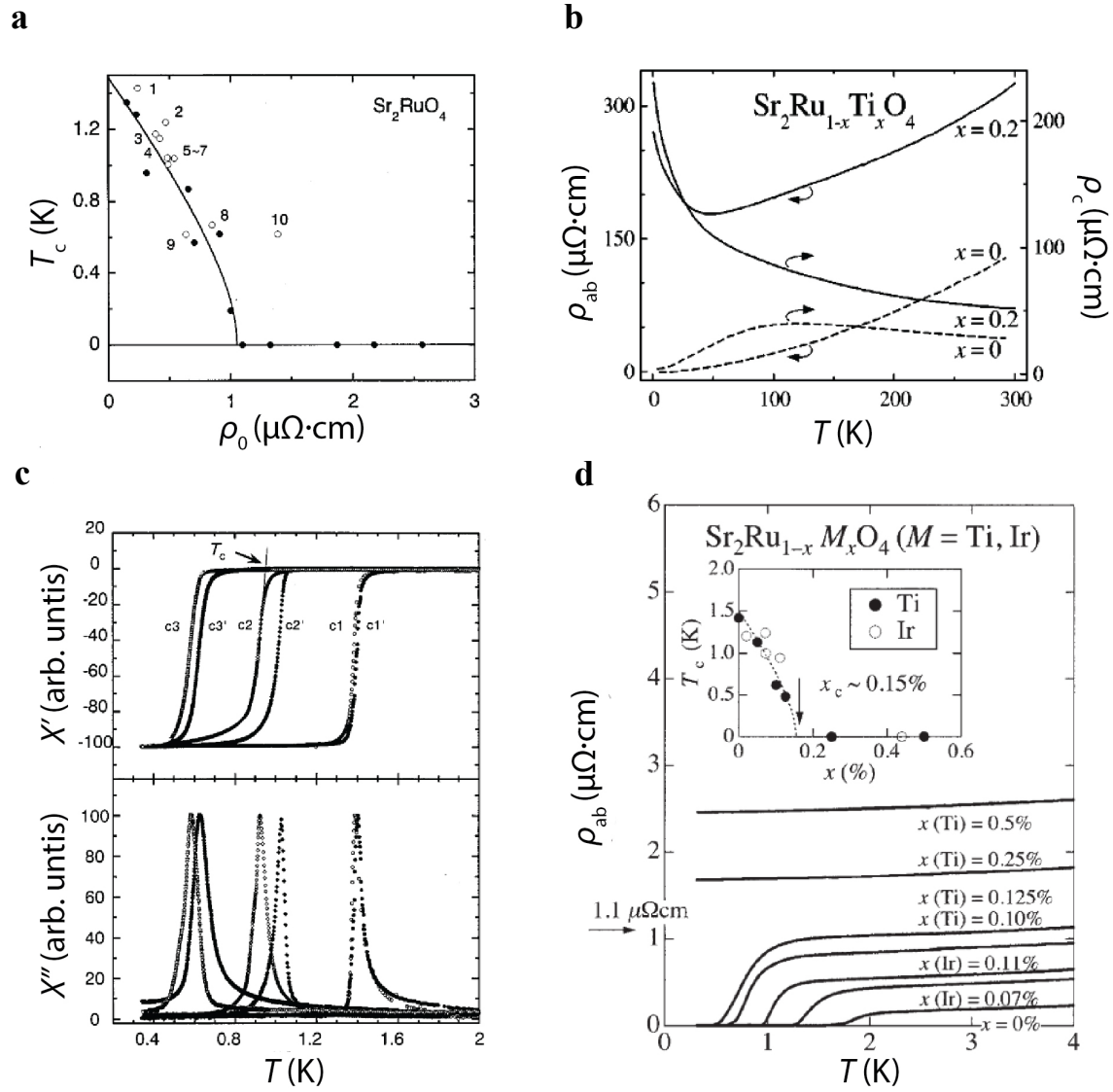

Figure 5.1 Impurity- and defect-induced suppression of the superconducting transition of SRO_{214} single crystals. Analysis of electrical (**a**, **b**, and **d**) and magnetic susceptibility (**c**). **a,** T_c versus ρ_0 when adding Al impurities (filled circles)[6] or defects (empty circles). Sharp superconducting transition (< 30 ppm Al, labels: 1,3), broad transition (30-50 ppm Al, labels: 2,4-8) and no superconductivity (> 50 ppm, label: 10). **b,d,** ρ versus T when adding Ti[62,73] (**b** and **d**) or Ir substitutional[62] (**d**) and its effect on T_c (**d-** inset). **c,** Shifts in T_c before and after thermal annealing to remove defects[9].

Similar to impurities, lattice defects act as strong potential scatterers. Mao *et al.*[9] introduced lattice defects in SRO_{214} single crystals by tuning the growth conditions, which later removed by a post-annealing treatment. They demonstrated a direct correlation between increased defects and residual resistivity (**Figure 5.1c**); however, they did not characterize the exact nature of the defects.

Local enhancements of T_c are caused by Ru inclusions, dislocations, and uniaxial strain. Single crystals of the eutectic phase of SRO_{214} with Ru precipitates have a T_c up to 3 K.[75] However, near the Ru inclusions, there is usually a large concentration of dislocations due to internal strain. Ying *et al.*[76] investigated the electrical properties of Ru-free flakes of SRO_{214} crystals to identify whether dislocations could be related to enhancements of T_c. They observed a local increase of T_c in areas with higher concentrations of edge-type dislocations and attributed this to the enhancement of the interlayer coupling in the vicinity of the compressed region caused by the dislocations. Nevertheless, despite calling them "edge" dislocations, the nature of the defects was not studied in their report. Lastly, other studies on SRO_{214} crystals (free of Ru inclusions) showed that the T_c increased locally under uniaxial pressure[77,78], and globally in the presence of tensile or compressive strain[79], preferable along in-plane directions[80].

Following with crystallographic defects, there are a few noted in the literature on SRO_{214} thin-films. They correspond to stacking faults near the interface with the substrate on thin-films deposited on (0 0 *l*)-oriented $(LaAlO_3)_{0.3}(Sr_2TaAlO_6)_{0.7}$ (LSAT) substrates. Most likely they are caused by the large out-of-plane mismatch between the thin-film and the substrate (69.64%)[43,44,46] (**Figure 5.2a**) and could explain the lack of reproducibility encountered by the authors. Besides having stacking faults, there are two reported superconducting thin-films, in which the distance between stacking faults was larger than ξ. For one of them, the T_c was locally enhanced with a broad transition, for which it is proposed that the superconducting transition occurs at higher T in the defect-free regions, and suppressed near stacking faults[44] (**Figure 5.2b,c**). Besides stacking faults, T_c was enhanced by Nair *et al.*[47] by selecting substrates with a large in-plane lattice mismatch to SRO_{214} and inducing strain on the film. They recorded a T_c of 1.9 K for SRO_{214} films on (1 1 0) $NdGaO_3$ substrates.

Despite a wide-range of experiments performed on single crystal and a few on thin-film SRO_{214}, there is no overall agreement on the nature of the structural defects that directly affect superconductivity in SRO_{214}. It is known that magnetic and non-magnetic impurities, as well as defects, alter the long-range order of the crystallographic structure of SRO_{214}, which reduces the superconducting transition. However, regarding the structural defects, it is still known very little about what exact type of defect directly correlates with the suppression of T_c in SRO_{214}.

In this chapter, we use resistivity measurements to evaluate the impact of defects in SRO_{214} thin-films to establish correlations with the suppression of superconductivity. Potential bulk-like defects are investigated in addition to linear and planar defects; misorientation, dislocations, microstrain and strain by X-ray diffraction.

a

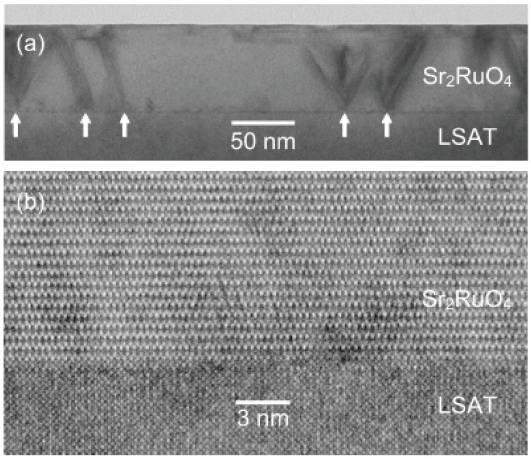

b

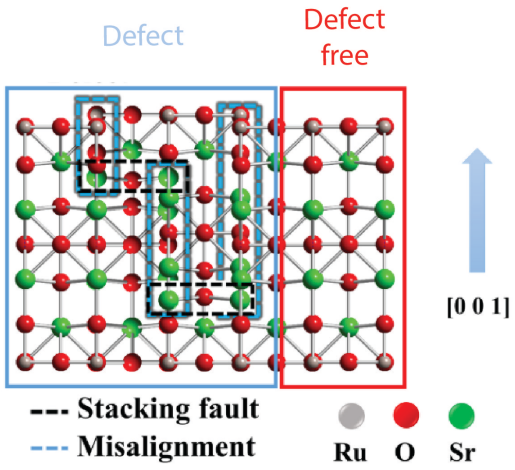

c

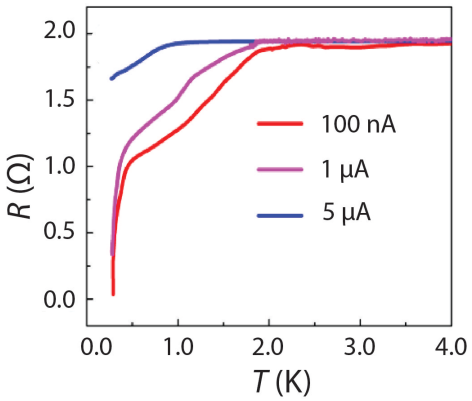

Figure 5.2 Stacking faults in SRO_{214} thin-films. a, Cross-sectional high-resolution transmission electron microscopy (HR-TEM) showing stacking faults at the substrate interface[6]. **b,** Schematic of lattice distortion caused by stacking faults, creating a defective region within the thin-film[44]. **c,** Broad superconducting transition due to defective regions on the thin-films[44].

5.2 Bulk defects from impurities

During the growth of SRO_{214} thin-films, other Ruddlesden-Popper phases of the same family stabilize when varying the oxygen pressure (see **Figure 3.4** in **Chapter 3**). Magnetic impurities of SRO_{113} and SRO_{327}, coexisting in the matrix of SRO_{214} might represent a hazard to superconductivity since the ferromagnetic exchange field of these phases can act as a pair breaker. During the fabrication of single crystals by the floating zone method (see **Chapter 4**), SRO_{113} phase tends to form when decreasing the seed-feed relative speed. It is worth noting that on single crystals, when the concentration of this impurity is low (< 100 ppm), no correlation with T_c has been recorded in the literature[23], and when the impurity phase is high enough (> 100 ppm for single crystals or > 2% for oriented thin-films), they can be characterised by X-ray diffraction, from a 2θ-ω scan. Alternatively, if the concentration is low they can be distinguished through the temperature dependence of the magnetic susceptibility, since SRO_{113} is ferromagnetic[26] with a bulk Curie temperature T_{Curie} of 160 K, and SRO_{327} is a paramagnet[25] at low temperature with a maximum paramagnetic moment below 16 K.

During the fabrication of single crystals, Ru inclusions can also solidify forming the eutectic concentration at the core of the crystal; Ru from the surface is lost due to evaporation. In SRO_{214} single crystals, Ru metal inclusions, as well as the SRO_{113} phase, can be observed on the surface of cleaved crystals with an optical microscope[23] (**Figure 5.3**) (see **Chapter 4**).

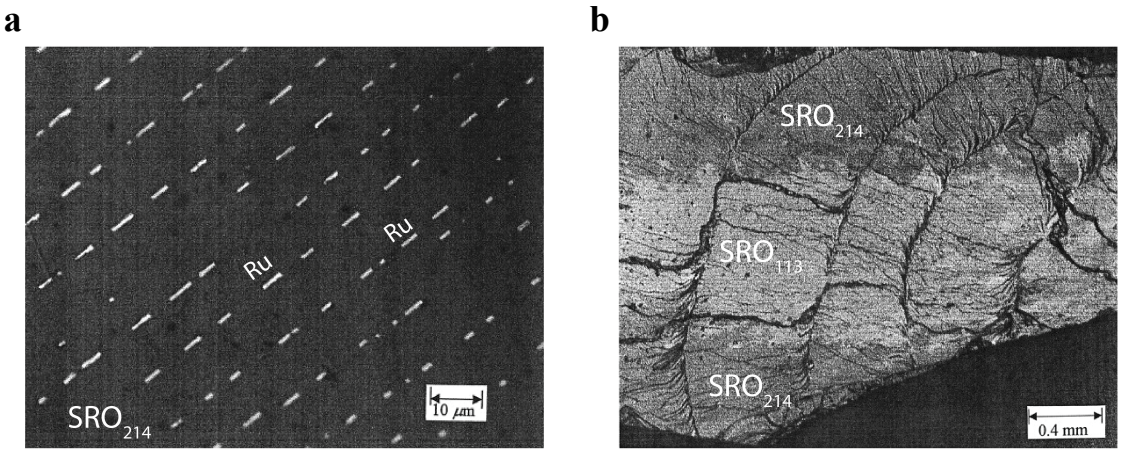

Figure 5.3 Optical micrographs of a cleaved surface of SRO_{214} single crystal showing impurity phases. a, A (0 1 0) cleaved surface where the light contrast represents Ru microdomains, and **b,** is from a (0 0 1) cleaved surface, where the light contrast corresponds to regions of epitaxial intergrowth of SRO_{113} phase in SRO_{214} (darker contrast). (From[23]).

5.3 Linear and planar defects

A representative example of electrical properties affected by linear and planar crystallographic defects is given by the semiconductor GaN. This material has been widely studied[81–84] since the performance of electrical devices based on GaN are strongly affected by defects and strain-induced during the fabrication process. Similar types of crystallographic defects should, therefore, be investigated in SRO_{214} thin-films since they could be potential candidates for the suppression of superconductivity. Following GaN reports, the targeted defects in this study are narrowed down to misoriented crystalline regions (tilt and twist) and the consequent dislocations (edge- and screw-type), microstrain ($\mu\varepsilon$), crystallite size (L), strain (ε), and stacking faults (frequently observed in SRO_{214} thin-films).

In the case that any crystallographic defect was present on SRO_{214} thin-films, they would perturb the crystallographic structure in real space, but also induce variations in the form of broadening or shifts on the reciprocal lattice points (RLP). We use X-ray diffraction (XRD), complemented with transmission electron microscopy (TEM) to evaluate these variations and quantify the presence of each structural defect. To do so, it is crucial to understand the direction where each defect broadens or shifts the RLP and the type of XRD scan required. Additionally, since some defects will enlarge the RLP in the same direction, it is also important to know whether they vary linearly when increasing the scattering vector, or they remain constant to be able to separate each contribution.

In the following section, the structural defects analysed in this study are described together with the experimental procedure to quantify them.

5.3.1 Tilt, twist, edge- and screw-type dislocations

In the mosaic crystal model, the film is described as the combination of smaller crystallites (blocks), misoriented to each other and the substrate. Rotation of these blocks about an axis parallel to the surface is known as mosaic tilt, and a rotation about an axis perpendicular to the surface is known as the mosaic twist. Tilted and twisted blocks are separated by low-angle grain boundaries consisting of dislocations, which can be edge- or screw-like, with a Burgers vector ($\vec{b}$) perpendicular or parallel to the dislocation line vector ($\vec{u}$) respectively.

Figure 5.4 illustrates how misoriented blocks tilt or twist the family of planes $\{h\ 0\ 0\}$, $\{0\ k\ 0\}$ and $\{0\ 0\ l\}$ depending on the direction of the dislocations. For simplicity, only one in-plane direction is represented as SRO_{214} has a tetragonal unit cell.

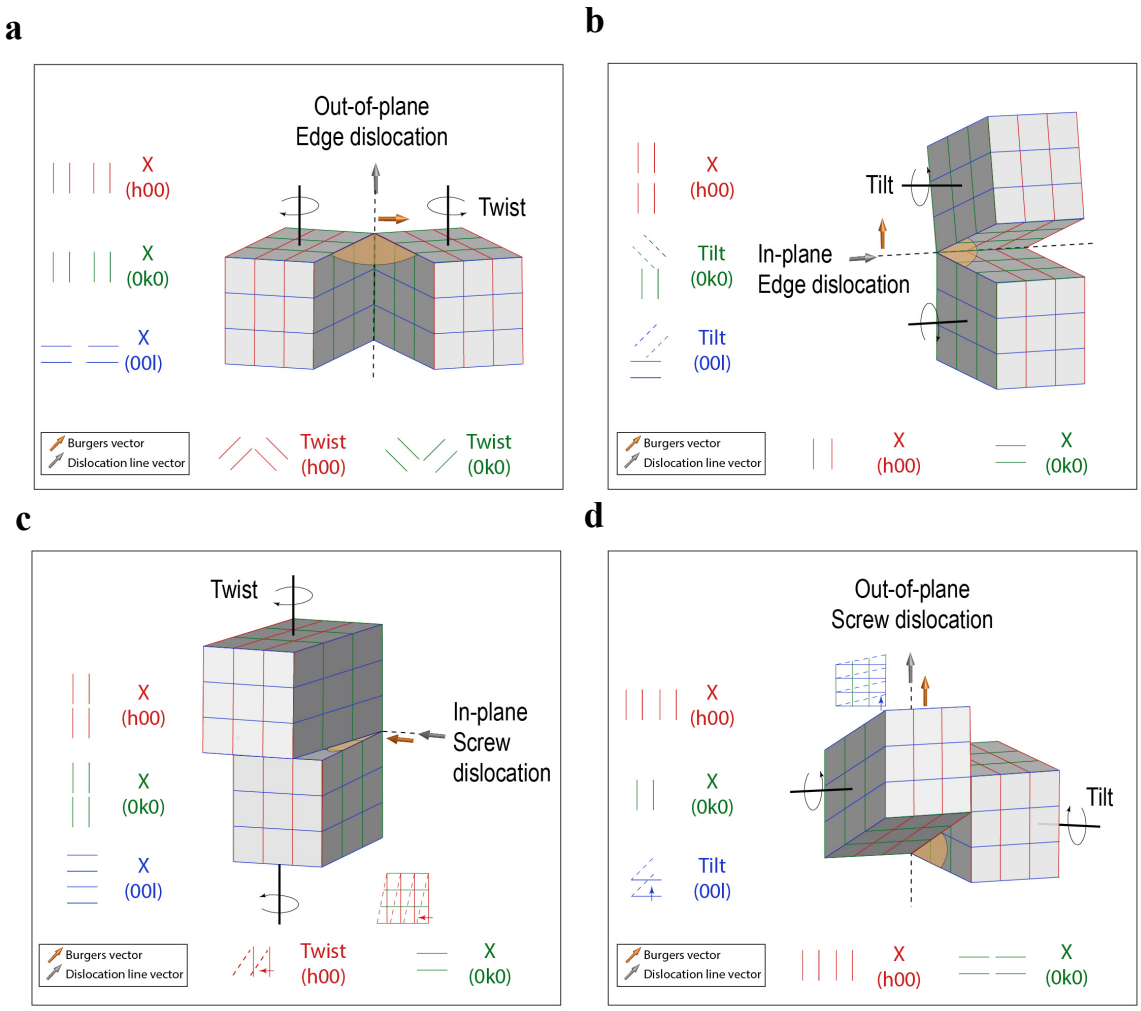

Figure 5.4 Schematic illustration showing how tilt and twist affect the {*h* 0 0}, {0 *k* 0} or {0 0 *l*} family of planes using the mosaic block model. The model includes the associated edge-type dislocations, in- (**a**) and out-of-plane (**b**) and screw-type dislocations, in- (**c**) and out-of-plane (**d**), represented by its line vector (grey arrow) and its Burgers vector (orange arrow).

When crystallographic planes are rotated with respect to adjacent planes (tilted or twisted), they vary the direction of the scattering vector ($\vec{s}$, normal to the plane surface). As an example, the schematic of the real space in **Figure 5.5** depicts an out-of-plane edge dislocation in an SRO_{214} thin-film, caused by the addition of an additional half-plane of (h 0 0) type. As a consequence, the {h 0 0} planes are rotated (twisted) and the direction of $\vec{s}$ is changed. In the reciprocal space, these changes increase the broadening of the RLP in the direction perpendicular to $\vec{s}$. Such broadening is measured from the FWHM of the XRD diffraction peaks of a ω scan.

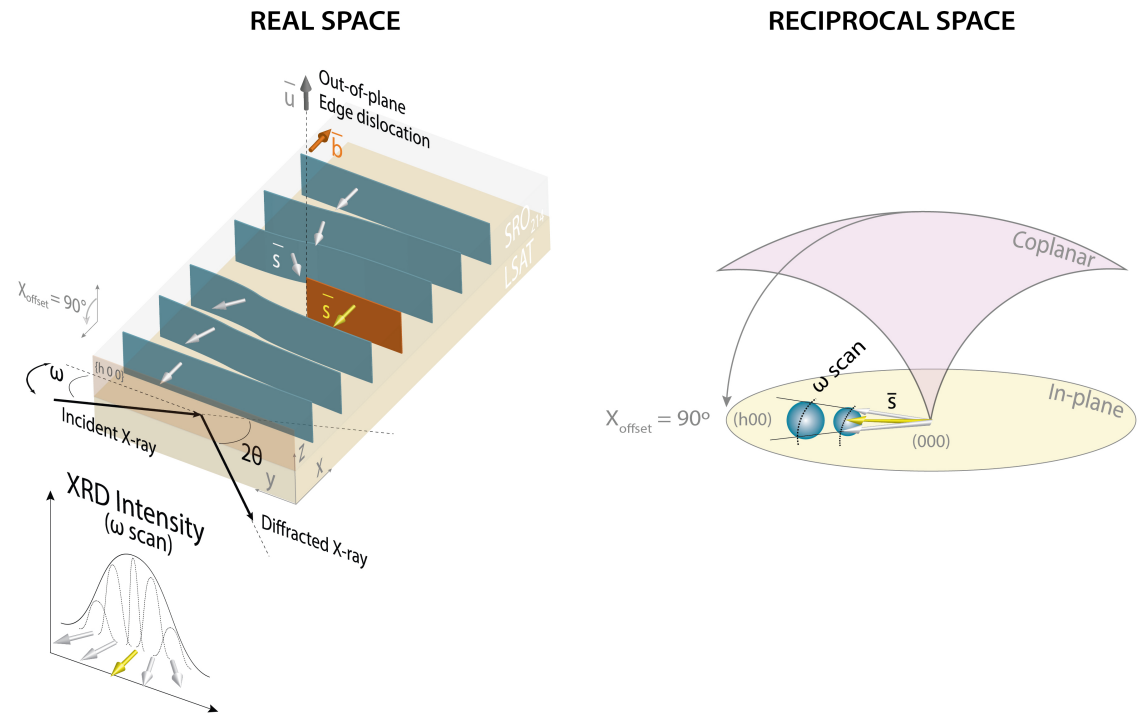

Figure 5.5 Schematic of an SRO_{214} thin-film with an out-of-plane edge dislocation in real space and the consequent broadening caused in the RLP. In the real space, the represented planes are $\{h\ 0\ 0\}$ and have a white arrow indicating its $\vec{s}$, except from the additional half plane, which has a yellow arrow. The edge dislocation is represented by its line vector ($\vec{u}$), grey arrow, and the Burgers vector ($\vec{b}$), orange arrow. It is also illustrated the X-ray diffraction set up of an ω scan in edge configuration to measure the degrees of twist. In reciprocal space, the $\{h\ 0\ 0\}$ planes are represented showing how variations in $\vec{s}$ increase the width of the RLP, and the corresponding ω scan to measure it.

In general, the degree of tilt can be extracted from the $FWHM_{\omega}$ of the $(0\ 0\ l)$ diffracting planes by XRD in a standard symmetric geometry. Apart from tilt, the total $FWHM_{\omega}$ measured is also affected in the same direction by the in-plane crystallite size, L_{ab}, and the instrumental broadening (**Figure 5.6a**). Since tilt varies linearly with $\vec{s}$ and L_{ab} is constant and independent of $\vec{s}$, its contribution can be separated by plotting the $FWHM_{\omega}$ in reciprocal space units, Δs, against $\vec{s}$. Where the $FWHM_{\omega}$ is extracted from the pseudo-Voigt profile fit of each $(0\ 0\ l)$ diffraction peak and has been corrected for the instrumental broadening as indicated in **Chapter 2**. From the linear fit of the plotted data, the resulting slope corresponds to the degrees of tilt (in radians) and the interception with the ordinate axis with $1/L_{ab}$:

$$\Delta s = 1/L_{ab} + Tilt \cdot s \qquad \textbf{5.1}$$

Similarly, twist affecting the $(h\ k\ 0)$ diffracting planes can be measured from the $FWHM_{\omega}$ with the film mounted in an edge geometry configuration - i.e. by measuring $(h\ k\ 0)$ planes with an offset in chi (χ_{offset}) of 90˚ (see **Figure 5.6b**), or by glancing angle in-plane, transmission or skew geometry[81]. For our thin-film geometry in-plane measurements are not physically possible, so to maximise the intensity we adopt a skew geometry (non-coplanar) configuration (**Figure**

5.6**c**). We measure the FWHM$_\omega$ from the (4 1 3) diffracting planes, which provides a good estimate of twist due to the large χ_{offset} (> 70° calculated using **Equation 2.7**)[83]. From the total FWHM$_\omega$, after applying a pseudo-Voigt fit, the contribution of twist is obtained after subtracting the L_{ab} (previously separated from the tilt) and the instrumental broadening (as shown in **Chapter 2**).

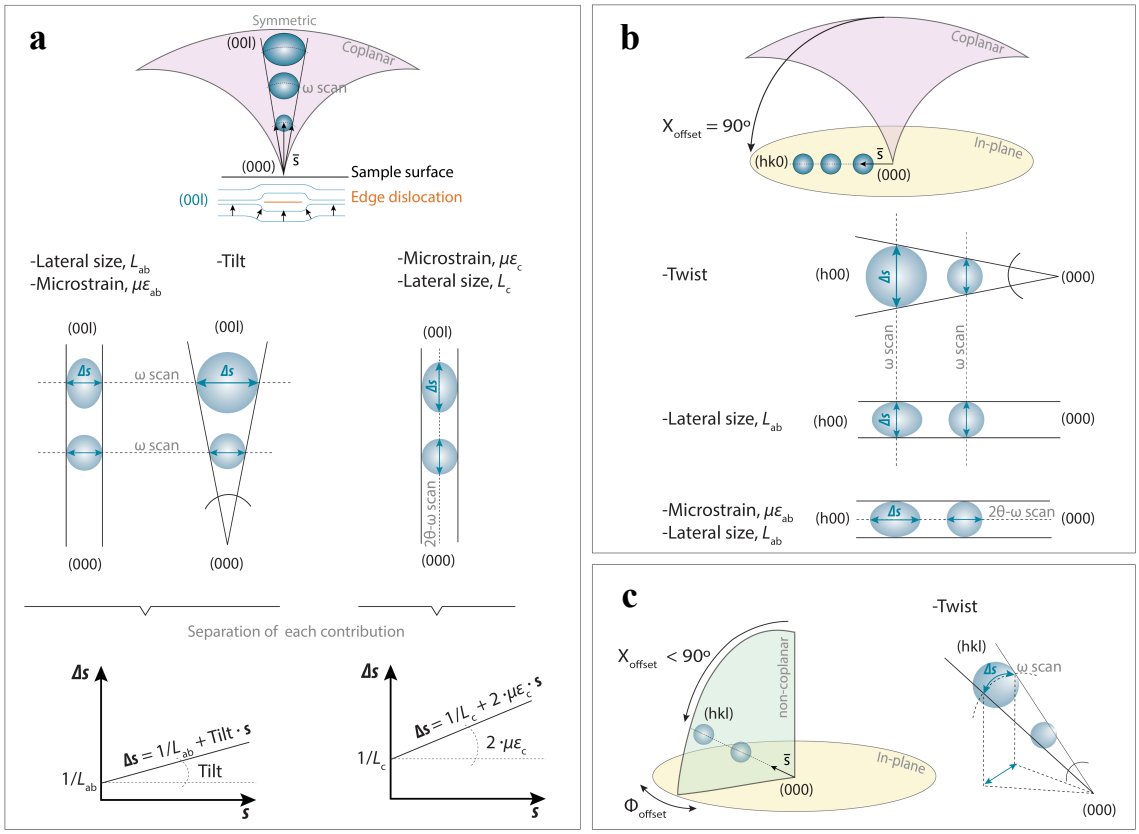

Figure 5.6 Summary of the different sources of broadening of the RLP and its measurement method using XRD. On symmetric co-planar planes {0 0 *l*} (**a**), tilt associated to dislocations, L_{ab}, and $\mu\varepsilon_{ab}$ cause broadening in the direction perpendicular to $\vec{s}$ (measured by ω scans), whereas L_c, and $\mu\varepsilon_c$, in the direction of $\vec{s}$ (measured by 2θ-ω scans), and each contributions can be separated using the plots indicated below. On in-plane RLP {*h k* 0} (**b**), twist and L_{ab}, affect the width of the RLP in the direction perpendicular to $\vec{s}$ (measured by ω scans) and L_{ab} and $\mu\varepsilon_{ab}$, in the direction perpendicular to $\vec{s}$ (measured by 2θ-ω scans). When in-plane measurements are not possible, the width of non-coplanar RLP {*h k l*} with a large χ_{offset} (**c**) provides a good estimation of in-plane broadening. (Adapted from [85]).

If the concentration of dislocations associated to tilt and twist is high enough, they can be visualized by local TEM measurements, with the $\vec{g} \cdot \vec{b}$ analysis, where $\vec{g}$ is the diffracted beam direction (also referred to as $\vec{s}$) and $\vec{b}$ is the Burgers vector of the dislocation. In the $\vec{g} \cdot \vec{b}$ analysis, different $\vec{g}$ are tested to determinate the type of dislocation (edge- or screw-type) based on the direction of the dislocation line vector, $\vec{u}$, and $\vec{b}$. When the condition $\vec{g} \cdot \vec{b} \neq 0$ is fulfilled ($\vec{b} \parallel \vec{g}$), the dislocations have a higher-contrast area and are visible, whereas for the

condition $\vec{g} \cdot \vec{b} = 0$ ($\vec{b} \perp \vec{g}$), the dislocations remain not visible (as shown in the schematic of **Figure 5.7**).

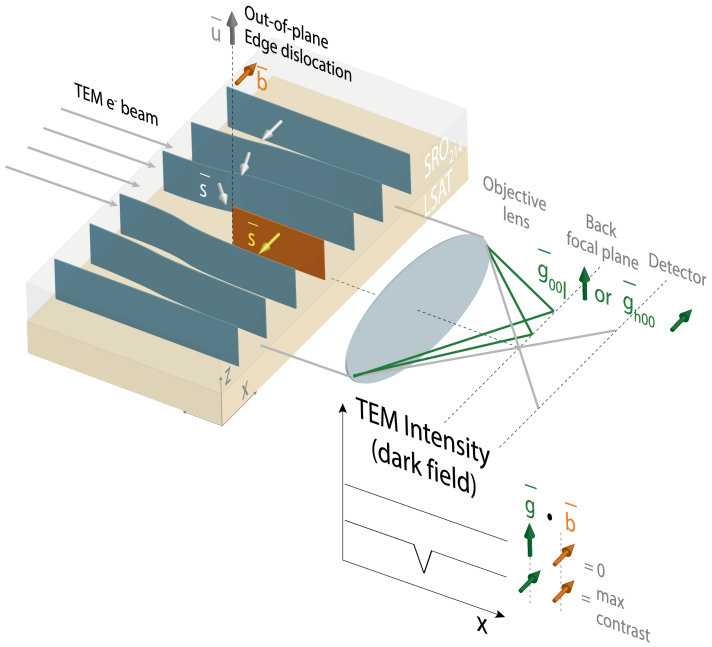

Figure 5.7 Schematic illustration of an SRO_{214} thin-film with an out-of-plane edge dislocation and the TEM $\vec{g} \cdot \vec{b}$ analysis to visualize the dislocations. TEM images are taken using dark field method with two perpendicular diffraction conditions ($\vec{g}_{00l}$ and $\vec{g}_{h00}$), green arrows. The edge dislocation is represented by its line vector ($\vec{u}$), grey arrow, and the Burgers vector ($\vec{b}$), orange arrow.

5.3.2 Microstrain

At grain boundaries between misoriented crystallographic regions, the associated dislocations produce local variations of the interplanar distance (d), known as in-homogeneous strain or microstrain ($\mu\varepsilon = \Delta d/d$). As illustrated in **Figure 5.6a,b**, the broadening of the XRD peaks in a 2θ-ω scan, $\mathrm{FWHM}_{2\theta\text{-}\omega}$, is affected by $\mu\varepsilon$, $\mathrm{FWHM}_{\mu\varepsilon}$, and L, FWHM_L:

$$\mathrm{FWHM}_{2\theta-\omega} = \mathrm{FWHM}_L + \mathrm{FWHM}_{\mu\varepsilon} \qquad \textbf{5.2}$$

From the Scherrer equation, $\mathrm{FWHM}_L = \frac{\mathrm{K}\cdot\lambda}{L\cdot\cos(\theta)}$, with K being the shape factor depending on the crystallite shape (for simplicity K = 1, see reference[86] for further information) λ, the X-ray wavelength, 1.5406 Å. And $\mathrm{FWHM}_{\mu\varepsilon} = 4 \cdot \mu\varepsilon \cdot \tan(\theta)$. By combining the formulas and re-arranging them we obtain:

$$\frac{\mathrm{FWHM}_{2\theta-\omega} \cdot \cos(\theta)}{\lambda} = \frac{1}{L} + \frac{4 \cdot \mu\varepsilon \cdot \sin(\theta)}{\lambda} \qquad \textbf{5.3}$$

For the calculation of the out-of-plane $\mu\varepsilon$ it is used the $FWHM_{2\theta\text{-}\omega}$ of co-planar diffraction peaks -i.e. (0 0 l). Since the broadening in reciprocal space units (Δs), is parallel to $\vec{s}$, its correlation to the real space follows:

$$\Delta s = \text{FWHM}_{2\theta-\omega} / \lambda \cdot \cos(\theta) \qquad \textbf{5.4}$$

By introducing **Equation 5.4** in **Equation 5.3**, and considering $|\vec{s}| = s = 2\sin\theta/\lambda$, it is obtained:

$$\Delta s = \frac{1}{L_c} + 2 \cdot \mu\varepsilon_c \cdot s \qquad \textbf{5.5}$$

From the linear equation ($\Delta s = \Delta s_0 + \text{m} \cdot s$), the value of $\mu\varepsilon_c$ can be extracted from the slope, $m = 2 \cdot \mu\varepsilon_c$, and the information about L_c can be obtained from the interception with the y-axis axis, $\Delta s_0 = 1/L_c$.

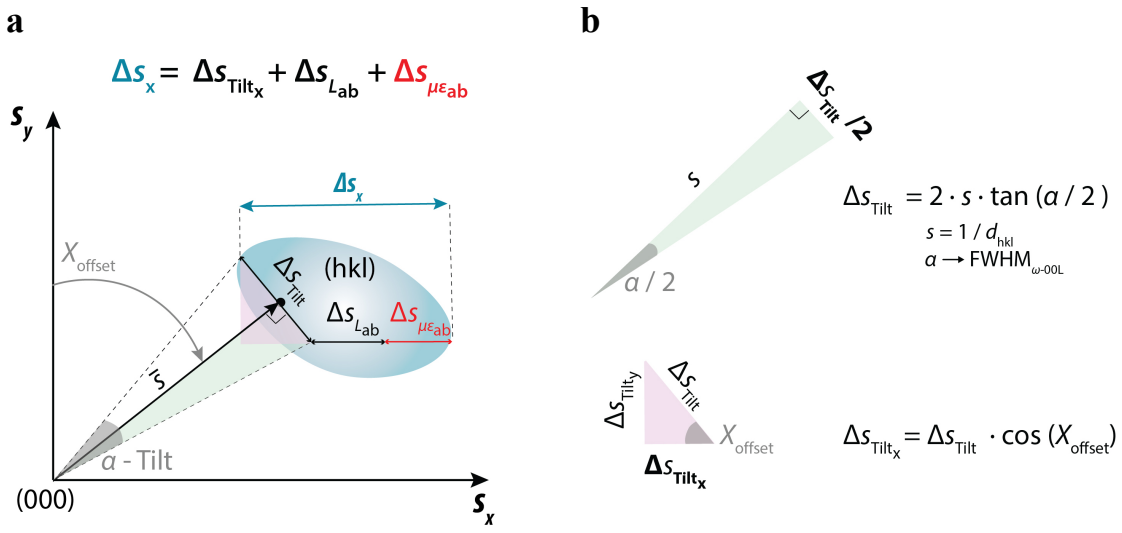

Figure 5.8 Schematic illustration of reciprocal lattice map of (*h k l*) plane indicating the different contributions to broadening. a, The figure illustrates that the total broadening in S_x direction as the result of α degrees of tilt, L_{ab} and $\mu\varepsilon_{ab}$. **b,** Detailed geometrical considerations for the calculation of the tilt component in the S_x direction.

The microstrain in-plane, $\mu\varepsilon_{ab}$, has to be calculated indirectly due to the complexity of in-plane measurements. This is done by subtracting from the total broadening of a reciprocal space map of any (*h k l*) plane in the S_x direction (Δs_x), the projection of the broadening due to tilt (Δs_{Tilt_x}), and due to L_{ab} ($\Delta s_{L_{ab}}$) (see **Figure 5.8a**). **Figure 5.8b** illustrates how Δs_{Tilt} and its projection in S_x direction is calculated based on their geometry and knowing the degree of tilt (α) and the modulus of the scattering vector (s) given an (*h k l*) plane and its χ_{offset} (**Equation 2.7**). The value of L_{ab} ($\Delta s_{L_{ab}} = 1/L_{ab}$) and α are obtained as indicated in **Figure** 5.6**a**.

It is worth noting that apart from the aforementioned contributions to the total broadening, there is also diffuse scattering surrounding each spot originated from the presence of other dislocations, stacking faults or impurities, which is neglected in this study as it would require synchrotron measurements to obtain higher resolution data.

5.3.3 Strain

Apart from creating broadening, a defective crystallographic structure can also shift the RLP i.e. strain (ε), defined as the variation of the average value of d. Materials under strain (or compression) experiment the expansion (reduction) of the lattice parameters compared to reported values under normal conditions. This type of defect varies the length of $\vec{s}$ ($s = 1/d_{hkl}$) while keeping the same direction, resulting in the shift of the RLP.

Out-of-plane strain (ε_c), is obtained by comparing the values measured of c-axis extracted from the peak position of a 2θ-ω scan of the (0 0 l) planes (c_{meas}), with reported values in the in non-strained conditions found in the literature (c_{ref}), following:

$$\varepsilon_c = \frac{c_{\text{meas}} - c_{ref}}{c_{ref}}, \varepsilon_{ab} = \frac{a_{\text{meas}} - a_{ref}}{a_{ref}} \qquad \textbf{5.6}$$

where the measured values have been calculated from data corrected for sample displacement as shown in **Chapter 2**.

Similarly, in-plane strain (ε_{ab}), can be calculated from the in-plane lattice parameter, a or b ($a = b$ in SRO_{214}) from a 2θ-ω scan on (h k 0) planes. However, due to the complexities of in-plane measurements, the in-plane lattice parameters can be obtained alternatively from the projections in Sx and Sz of any (h k l) diffracting plane in a RSM (see **Figure 2.6**).

5.4 Discussion

We investigate PLD thin-films with the same growth conditions (950˚C, 0.35 Pa of O_2 and laser fluence of 1.0 J cm^{-2}) in a range of thicknesses (t), from 15 to 166 nm (**Figure 5.9**) (see **Chapter 4** for optimization of the growth conditions).

In **Figure 5.9a** the T_c for each film is correlated with its, t, where two differentiated regions can be observed; above, and below t = 50 nm. Above 50 nm, all the thin-films are superconducting and the T_c increases with t, reaching the maximum value of 1.05 K for t = 166 nm. Although it is still below SRO_{214} bulk T_c (1.5 K), it corresponds to the highest reported value of a fully superconducting SRO_{214} thin-film on LSAT substrate (**Figure 5.10a**). However, below 50 nm, films deposited with a laser repetition rate of 2 Hz show metallic

behaviour (inside the red bubble), with partial (corresponding to the sample with optimized growth conditions shown **Chapter 4**) or complete suppression of the T_c.

Additionally, the *t*-dependence with *RRR* is plotted (**Figure 5.10b**), defined as the coefficient between the resistivity at room temperature and the saturated minimum in the resistance in metallic samples or before the onset for superconducting samples. For the superconducting samples (included in the blue bubble) *RRR* is enhanced with the *t*, with the highest recorded value of 110 (t = 100 nm), which is high relative to equivalently-thick SRO_{214} films reported elsewhere (**Figure 5.10b**). In comparison, metallic films (t < 50 nm) show a reduced *RRR*, pointing at the presence of defects.

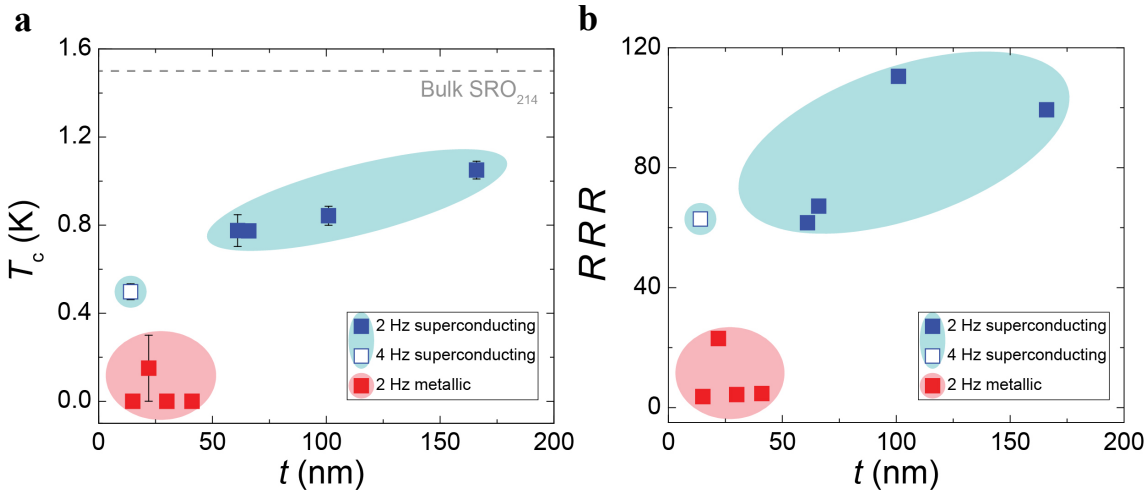

Figure 5.9 Characterization of the electrical properties of SRO_{214} thin-films when varying the film thickness. a,b Thickness dependence of the T_c (**a**) and the *RRR* (**b**). Blue bubbles identify superconducting samples and red bubbles metallic samples (including partially superconducting thin film with optimized growth conditions from **Chapter 4**). Error bars in **a** represent the width of the superconducting transition.

It is worth noting that below 50 nm superconductivity is observed in one film (t = 15 nm). Since this film is deposited with double laser repetition rate (4 Hz) compared to the rest of the films, it is represented by an empty square.

For the superconducting thin-films, we calculated the superconducting coherence length in- and out- of plane at 0 K, $\xi_{ab}(0)$ and $\xi_c(0)$ from the upper critical field in-and out-of-plane at 0 K, H_{c2}^{ab} and $H_{c2}^{c}(0)$ following:

$$H_{c2}^{c} = \phi_0/2\pi\xi_{ab}^2 \quad \textbf{5.7}$$

$$H_{c2}^{ab} = \phi_0/2\pi\xi_{ab}\xi_c \quad \textbf{5.8}$$

where ϕ_0 is the superconductor flux quantum ($\phi_0 = \frac{h}{2e} = 2.067 \cdot 10^{-15} \mathrm{kg} \cdot \mathrm{m}^2 \cdot \mathrm{s}^{-2} \cdot \mathrm{A}^{-1}$) derived from the combination of the Planck constant (h) and the electron charge (e).

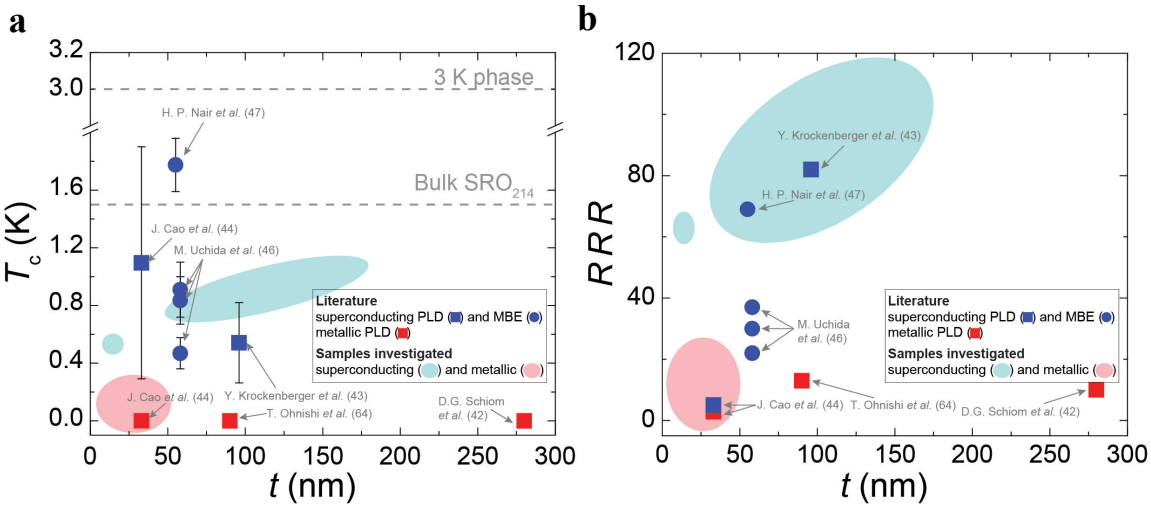

Figure 5.10 Comparison of the electrical properties of SRO_{214} thin-film from our study and previously published results. a,b Thickness dependence of the T_c (**a**) and the *RRR* (**b**). Blue bubbles identify superconducting samples and red bubbles metallic (including partially superconducting) samples from this thesis, and squares and circles and represent PLD and MBE respectively. Error bars in **a** represent the width of the superconducting transition.

H_{c2}^{ab} and $H_{c2}^{c}(0)$ are known values from electrical transport measurements when applying different in- and out-of-plane magnetic fields. For each field, the temperature at which the normal resistance drops 50 or 90% is recorded (labelled as "Rn50" and "Rn90" in the example shown in **Figure 5.11a**). From extrapolation of the recorded temperatures to 0 K, H_{c2}^{ab} and $H_{c2}^{c}(0)$ are obtained with an error bar that indicates the difference between 50 and 90% drop in the normal resistance (see example in **Figure 5.11b**).

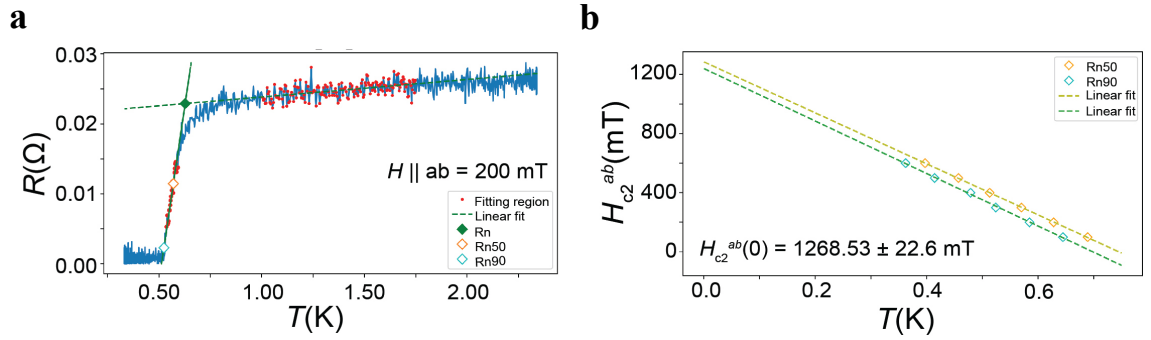

Figure 5.11 Example showing the procedure to obtain the upper critical field in-plane H_{c2}^{ab}. a, Example of a $R(T)$ characteristic with an applied field in-plane of 200 mT fitted to obtain the temperature at which a drop of the normal resistance of 50% (Rn50) and 90% (Rn90) occurs. **b,** Applied field versus the temperature of Rn50 and Rn90 extrapolated to 0 K to obtain $H_{c2}^{ab}(0)$ (indicated in the graph). The error bar is the difference between $H_{c2}^{ab}(0)$ for Rn50 and Rn90.

Since the *t*-dependence of the ξ_{ab} and ξ_c of superconducting samples confirms similar values to SRO_{214} bulk (**Figure 5.12a**), it is then studied the normal resistivity (ρ_0), defined as the resistivity at the onset of the superconducting transition, or 0.1 K for metallic films to confirm if the suppression of the superconductivity is related to impurities and defects. From **Figure 5.12b** it can be observed that superconducting films (inside the blue bubble) have lower ρ_0 compared to metallic or partially superconducting films (red bubble), where $\rho_0 > 5$ μΩ·cm, suggesting that defects or impurities might be acting as pair breakers like previously seen on single crystals. This is also supported by the decrease of *RRR* below 40, when *t* goes under the critical value of 50 nm (**Figure 5.9b**).

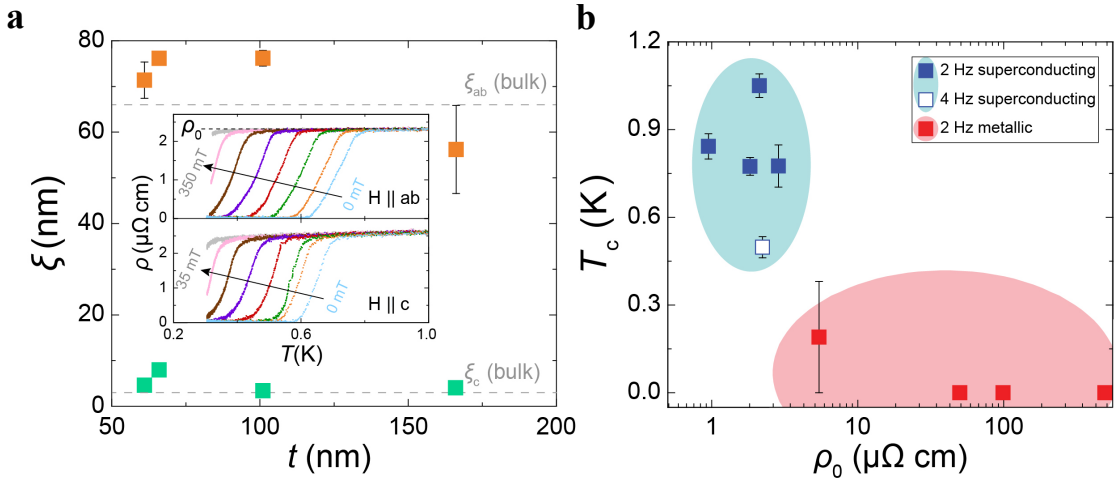

Figure 5.12 Characterization of the electrical properties of SRO_{214} thin-films to correlate non-superconducting behaviour with structural defects. a, Correlation between the coherence length in- and out-of-plane (green and orange squares respectively) with the film thickness and **b,** the correlation between the T_c and the normal resistivity (ρ_0) when varying the thickness. Blue bubbles identify superconducting samples and red bubbles metallic samples (including partially superconducting thin film with optimized growth conditions from **Chapter 4**). Error bars in **a** represent the difference between 50 and 90% drop in the normal resistance.

Based on the electrical transport properties, a superconducting (t = 66 nm) and a metallic (t = 41 nm) thin-film are selected to compare their microstructure and look for potential defects or impurities that could perturb the long-range crystallographic order in the metallic film. We first look at the surface of the thin-films with an optical microscope, but since no contrast was observed (i.e. due to additional phases) a more detailed analysis by TEM is performed on cross-sections extracted from the films. STEM (**Figure 5.13a,g**) and HR-TEM images (**Figure 5.13b,h**) demonstrate *c*-axis coherent growth. STEM on the superconducting sample (**Figure 5.13a**) additionally reveals inclusions close to the SRO_{214}/LSAT interface that are crystalline (see HR-TEM in **Figure 5.13f**) and EDX compositional analysis confirms that they are mainly elemental Ru (**Figure 5.13c-e**) or RuO_2 (**Figure 5.14**).

On the metallic sample, STEM shows a 1-2 nm thick region (dark contrast indicated with an arrow) (**Figure 5.13g**) with varying composition compared to the SRO_{214} thin-film. Chemical analysis by EDX shows atomic layers that have stoichiometric Sr (green map), are Ru deficient (pink map) and rich in O (blue map) compared to the thin-film (**Figure 5.13i-k**). This is also supported by HR-TEM, which shows that there is a lower concentration of heavy atoms in that area and stoichiometric SRO_{214} in the rest of the thin-film (**Figure 5.13h**,**l**). The formation of this region could be due to the separation of the Ruddlesden-Popper phase into SRO_{113} (perovskite unit cell) and SrO (rocking salt unit cell). In an oxidizing atmosphere, such as during the PLD growth, SrO can stabilize into SrO_2 leading to an O-rich and Ru-deficient region that matches the stoichiometry from EDX analysis.

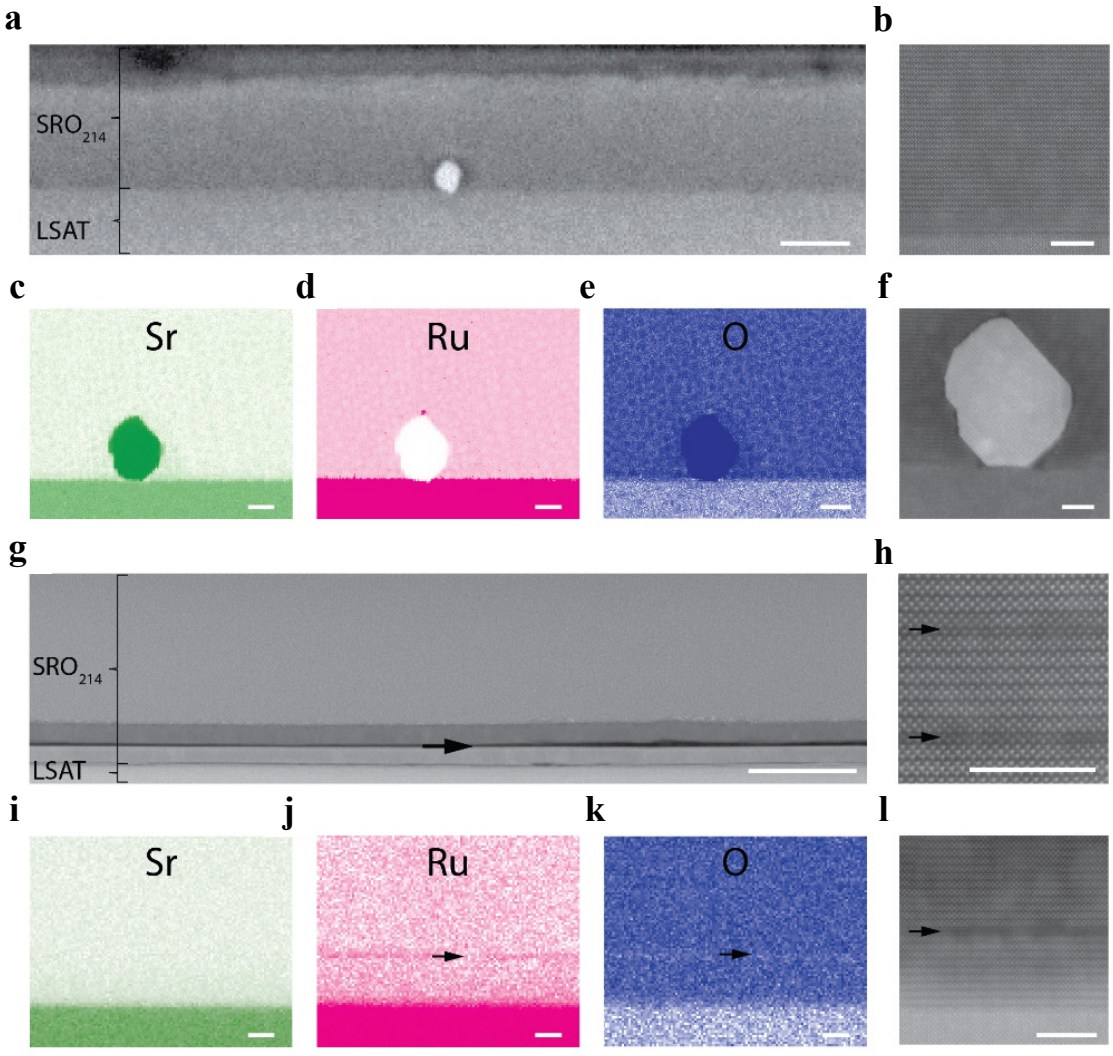

Figure 5.13 Comparison of the structural and chemical properties of superconducting and metallic SRO_{214} films. **a-f**, STEM micrographs for a t = 66 nm thick superconducting film (a) showing inclusions at the SRO_{214}/LSAT interface and HR-STEM of an area close to the same interface in (**b**). EDX maps of the inclusions in (**a**) are shown in **c-e** for Sr (**c**), Ru (**d**) and O (**e**) with a HR-STEM micrograph of the inclusion in (**f**). **g-l,** STEM micrograph of a t = 41 nm metallic film (**g**) showing an interface layer of different stoichiometry (dark black line indicated with an arrow) to the rest of the film with corresponding EDX maps for Sr (**i**), Ru (**j**) and O (**k**). **h,l,** HR-STEM on an area of the SRO_{214} thin-film (**h**) and

SRO_{214}/LSAT interface (**l**) showing a decreased concentration of heavy atoms in some of the layers. **g-l** Depleted region indicated with arrows. The scale bars are **a,** 50 nm, **b, f, h, l,** 5 nm, **c, d, e, I, j, k,** 10 nm and **g**, 25 nm. Note that in (**c-e**) and (**i-k**), white regions indicate highest (relative) atomic content, whereas intense (pink, green, blue) colouring indicates the lack of the corresponding element.

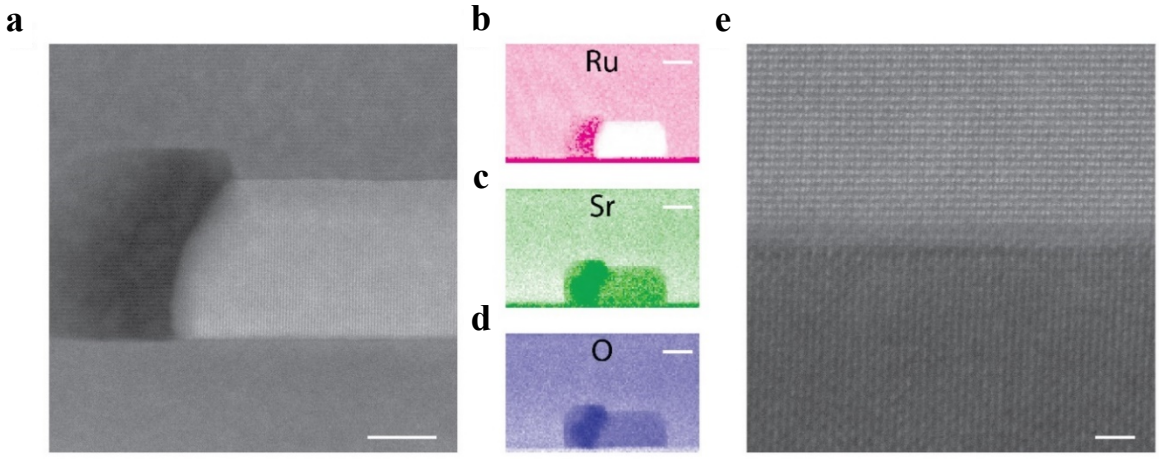

Figure 5.14 Structural characterization of a superconducting SRO_{214} thin-film near an interface inclusion. a, e, HR-STEM micrographs for a 66-nm-thick superconducting film (**a**) showing inclusions at the SRO_{214}/LSAT interface and a closer micrograph of the LSAT/Inclusion interface (**e**). **b-d,** EDX maps around the inclusion for Ru (**b**), Sr (**c**) and O (**d**). Scale bar in a, 10 nm, **b, c, d,** 20 nm, and **e,** 1 nm. Note that in (**b-d**), white regions indicate highest (relative) atomic content, and intense (pink, green, blue) colouring indicates the lack of the corresponding element.

From the analysis of the microstructure, it is worth noting that there is no evidence of stacking faults in the thin-films, as previously reported by other authors in the thin-film geometry. However, the non-superconducting thin-film might be linked to the presence of SRO_{113} impurity phase. This information together with the presence of an unidentified peak in the XRD analysis (see in **Figure 4.15a** peak labelled as "*") that could belong to another Ruddlesden-popper phase like SRO_{327}, SRO_{4310}, or RuO_2 motivated a further investigation of possible impurity phases. It is unlikely that the non-identified phase on the metallic thin-film corresponds to RuO_2 since no evidence of inclusions have been observed on the TEM micrographs and Ru inclusions are generally related to the enhancement of T_c rather than its suppression.

Therefore, we look for magnetic traces coming from SRO_{113}, SRO_{327} and SRO_{4310} phases. To do so, we study the temperature dependence of the magnetic moment $m(T)$ of the metallic thin-film (t = 15 nm) when applying an out-of-plane magnetic field (**Figure 5.15a**). To quantify the signal from the substrate, the data is compared with a control LSAT substrate exposed to the same growth conditions as the thin-film, but without depositing any material on it. The $m(T)$ data do not show any evidence of SRO_{113}, or SRO_{4310} since there is not a ferromagnetic transition at 160 K or 100 K[87] respectively. Regarding SRO_{327} impurity phase, no maximum in T at 16 K is observed, as the signal might be overlapped by the strong paramagnetic signal of

the LSAT below 20 K. We also recorded the $m(H)$ at 20K of the film and the control LSAT (**Figure 5.15a-inset**). When subtracting the LSAT momentum saturation, m_{sat}, to the thin-film, the resulting value is lower than $1e^{-6}$ emu, which is within the detection limits of the VSM-SQUID used for the measurements (in pure SRO_{327} single crystals, the intensity of the maximum in the momentum at 16 K is larger than $2e^{-2}$ emu). In the hypothetical case that there would be $1e^{-6}$ emu of SRO_{327}, knowing that the saturation magnetization of SRO_{327} is 194.27 emu·cm^{-3} and that the thin-film surface is 0.195 cm^2, the thickness of an SRO_{327} layer would be lower than 0.26 nm.

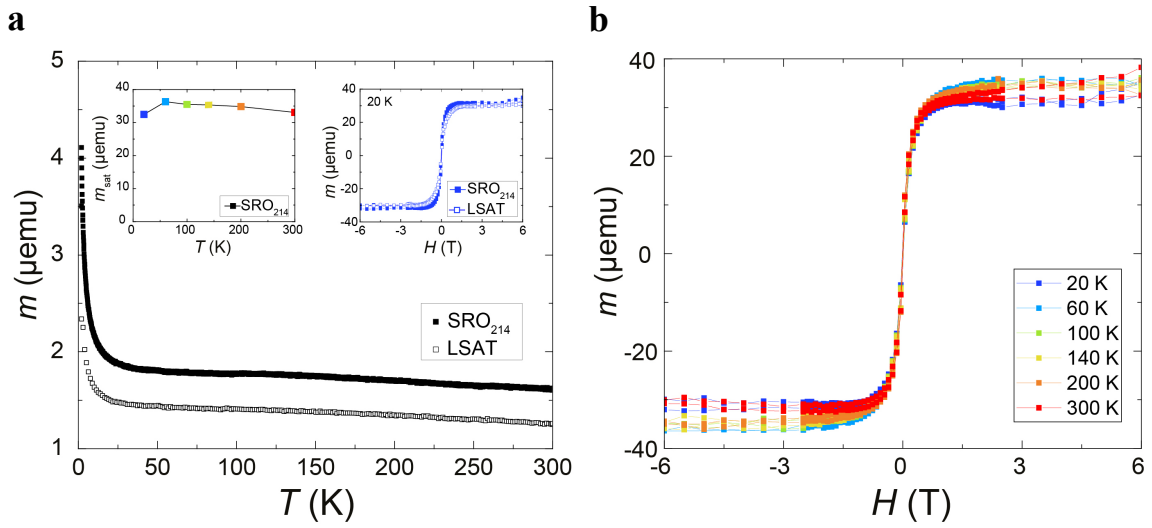

Figure 5.15 Magnetic characterisation of SRO_{214} thin-films. a,b Magnetic moment measurements using a superconducting quantum interference device with a vibrating sample magnetometer (SQUID-VSM) for a $t = 15$ nm SRO_{214} metallic thin-film and a control LSAT substrate, when applying an out-of-plane magnetic field. **a,** Magnetic moment versus T, showing no T_{Curie} of SRO_{113} (~ 160K), saturation moment versus T of the thin-film extracted from **b** (left inset) and moment versus magnetic field hysteresis loops at $T = 20$K of the thin-film and the control LSAT (right inset). **b,** Moment versus magnetic field hysteresis loops at a range of T (20-300K).

In the XRD characterization of the metallic thin-film ($t = 15$ nm), if the non-identified peak located between 40-50° (marked with an "*" in **Figure 4.15a**) is matched with the (0 0 10) diffraction plane of SRO_{327} phase, the thickness of a potential SRO_{327} layer could be calculated using the relative intensity ratio, RIR (see **Chapter 2**). In the mentioned case, the intensity of the SRO_{327} peak would correspond to a layer of 0.46 nm of SRO_{327}, which would produce a m_{sat} of $1.56e^{-6}$ emu; other examples are shown in **Table 5.1**.

Despite being able to identify the depleted region of the non-superconducting sample observed in TEM, with a combination of SRO_{327} and SrO, the presence of SRO_{327} cannot be attributed to the suppression of the T_c since this impurity phase is also present in superconducting samples (**Table 5.1**).

After confirming that impurities are not breaking the superconducting pairs on SRO_{214} thin-films, the focus is now on the study of linear and planar crystallographic defects as they could be another source of defects, at a smaller scale, that alter the long-range crystallographic order.

The *t*-dependence of tilt is studied on SRO_{214} thin-films by XRD (**Figure 5.16a**) from the $FWHM_{\omega}$ of the (0 0 *l*) diffraction planes. The instrumental broadening is subtracted from each diffraction peak (following **Chapter 2**) and the contribution of tilt from L_{ab} is separated (see **Figure 5.16a** inset for an example of t = 63 nm). Values of tilt extracted from SRO_{214} films with different t show that all films (superconducting or non-superconducting), except for one, have similar values of tilt. Therefore, tilt does not affect the electrical properties (see **Figure 5.16b**).

Table 5.1 Calculation of the thickness of a layer of SRO_{327} in SRO_{214} thin-films, based on the intensity of the diffracted peaks in a 2θ-ω scan using the RIR method.

Sample	SRO_{214} $I_{(0\,0\,6)}$ (counts)	SRO_{327} $I_{(0\,0\,10)}$ (counts)	Ratio (SRO_{327}/SRO_{214})	t_{total} (nm)	t_{SRO327} (nm)
		-	-	14	-
	7309.00	210.000	0.02873	15	0.41
	4835.00	109.000	0.02254	23	0.49
		-	-	30	-
		-	-	41	-
	87681.0	823.000	0.00938	61	0.55
		-	-	66	-
		-	-	101	-
	310069	209.000	0.00067	166	0.11
Reference	8333.29 (73395-ICSD)	8481.75 (192343-ICSD)	1.01781		

Similarly, the *t* dependence of twist is studied on SRO_{214} thin-films by XRD (**Figure 5.17a**) from the $FWHM_{\omega}$ of the (4 1 3) diffraction planes. In the represented values of twist, the instrumental contribution is subtracted (see **Chapter 2**) and the broadening due to L_{ab} is neglected since the calculated value, previously separated from the broadening due to tilt, is of the order of the micron metre size (reaching the resolution limit of the detector). The results show that the degree of twist (and hence the $FWHM_{\omega}$ - see **Figure 5.17 inset**) rapidly rises as t decreases below 50 nm, corresponding to the metallic thin-films that do not show a superconducting transition. Furthermore, **Figure 5.17b** demonstrates a direct correlation between twist and the suppression of superconductivity by a reduction of T_c (or increase of ρ_0 – see **Figure 5.17b** inset) when the degree of twist increases. Regarding the sample deposited with a laser repetition rate of 4 Hz (empty square), the twist is lower compared to other metallic films of similar thickness, inferring that the laser frequency might have a positive effect on the

reduction of this defect. However, further studies towards these lines are required to confirm that.

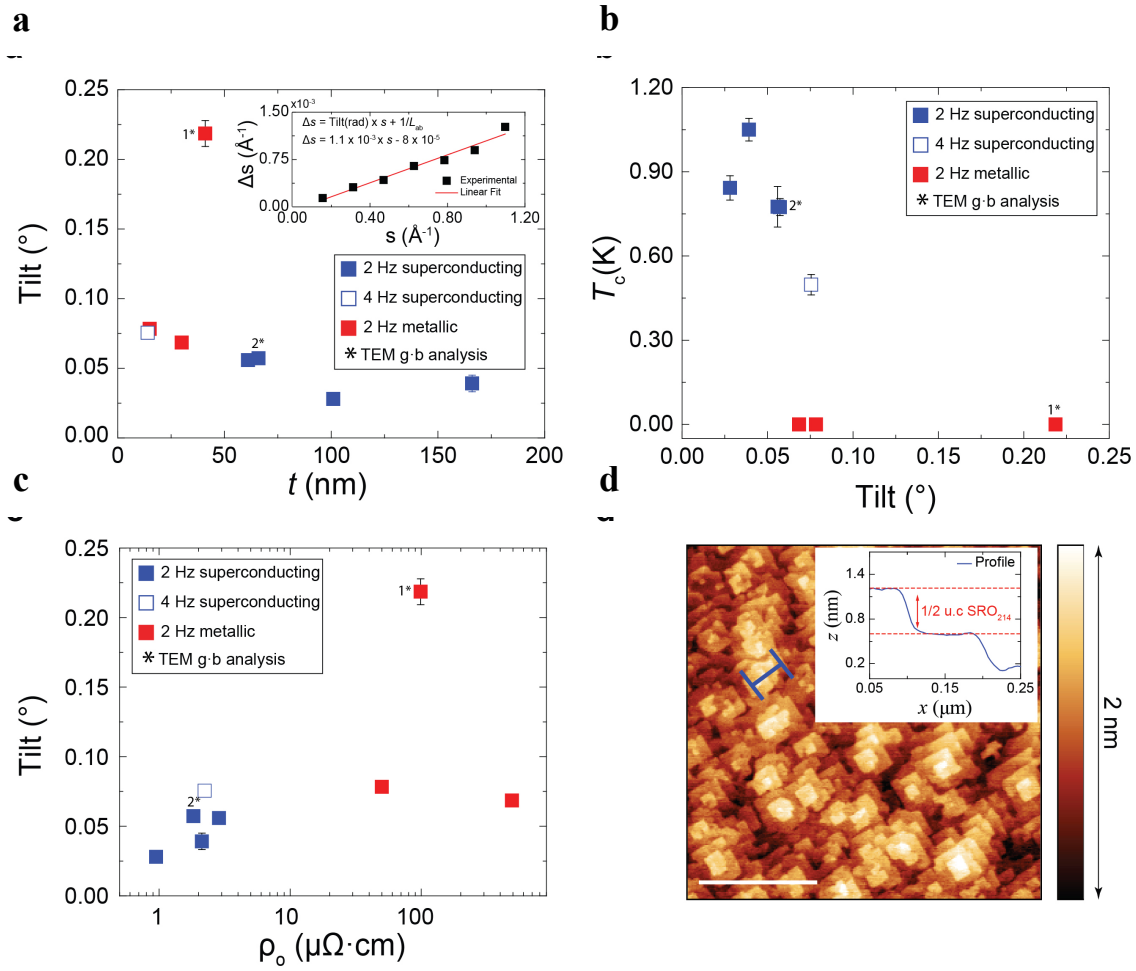

Figure 5.16 Tilt of SRO_{214} thin-films for different thickness and its correlation with electrical properties. a, Degree of tilt versus t. Contribution of tilt separated from the L_{ab} by measuring the $FWHM_{\omega}$ of the (0 0 l) planes. The former increases with $\vec{s}$ whereas the latter remains constant (see inset for t = 63 nm). **b,** T_c as a function of the degree of tilt and **c,** degree of twist versus residual resistivity showing no correlation. The samples marked with "*" in **a, b** and **c,** have been further studied by TEM g dot b analysis. **d,** AFM on a 3 x 3 μm^2 region of the surface of a t = 23 nm metallic thin-film showing the presence of screw dislocations and the extracted profile corresponding to the blue line (inset). Scale bar in **a,** 1 μm. Error bars in **b** represent the width of the superconducting transition.

The increase in twist with decreasing t (**Figure 5.17a**) indicates a higher concentration of dislocations with $\vec{b}$ in-plane at low t for non-superconducting films. As well, some dislocations with $\vec{b}$ out-of-plane are also expected since the degree of tilt in the films is non-zero; also corroborated by AFM topography images that show screw type dislocations on the surface of the thin-films (**Figure 5.16d**). To confirm the increase in the concentration of dislocations and determine their nature, $\vec{g} \cdot \vec{b}$ TEM analysis is conducted on the superconducting film (t = 66 nm) and the non-superconducting film (t = 41 nm) (previously studied by TEM).

The superconducting film shows a lower concentration of dislocations (**Figure 5.18a-f**) compared to the non-superconducting film (**Figure 5.18g-l**). The low density of dislocations present in the superconducting film is mainly formed by in-plane edge-like, with $\vec{u}$ in-plane and $\vec{b}$ out-of-plane (vertical orange arrow), as they are visible when $\vec{b} \parallel \vec{g}_{00l}$ (**Figure 5.18a-c**) and not visible when $\vec{b} \perp \vec{g}_{h00}$ (**Figure 5.18d-f**).

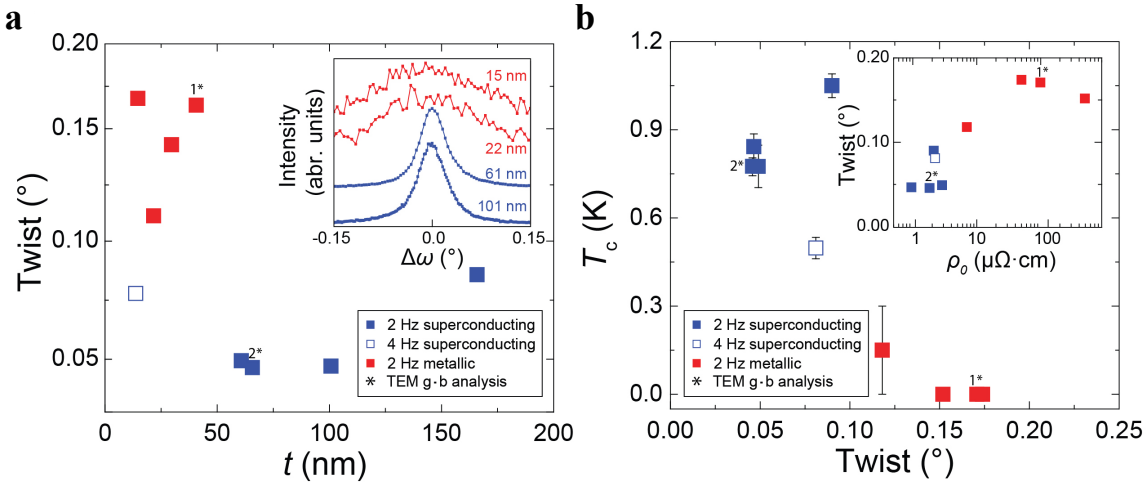

Figure 5.17 Twist of SRO_{214} thin-films for different thickness and its correlation with electrical properties. a, Degree of twist versus t extracted from the $FWHM_{\omega}$ of the (4 1 3) planes (inset curves offset for clarity). **b,** T_c as a function of the degree of twist, and degree of twist versus residual resistivity (inset) showing a correlation. The samples marked with "*" in **a** and **b**, have been further studied by TEM g dot b analysis. Error bars in **b** represent the width of the superconducting transition.

In contrast and consistent with the high degree of twist observed in non-superconducting films, the dislocations observed in the metallic thin-film are mostly in-plane and screw-like with both $\vec{u}$ and $\vec{b}$ in-plane (horizontal orange arrow), as they can only be resolved when $\vec{b} \parallel \vec{g}_{h00}$ (**Figure 5.18j-l**) and are extinct when $\vec{b} \perp \vec{g}_{00l}$ (**Figure 5.18g-i**). This result demonstrates that horizontal screw dislocations are a key defect that strongly suppresses superconductivity in SRO_{214}.

In both the superconducting and non-superconducting films, a few threading mixed dislocations, with both edge and screw components (tilted orange arrow) are resolved with both $\vec{g}_{00l}$ and $\vec{g}_{h00}$. The presence of threading dislocations with a screw component is consistent with the topographic images acquired using an atomic force microscope (**Figure 5.16d**).

To complete the structural analysis and since dislocations are linked to local variations of d, the values of $\mu\varepsilon$ are also calculated. Because $\mu\varepsilon$ widens the diffraction peaks in the same direction as L, first both contributions are separated to obtain the values of each variable.

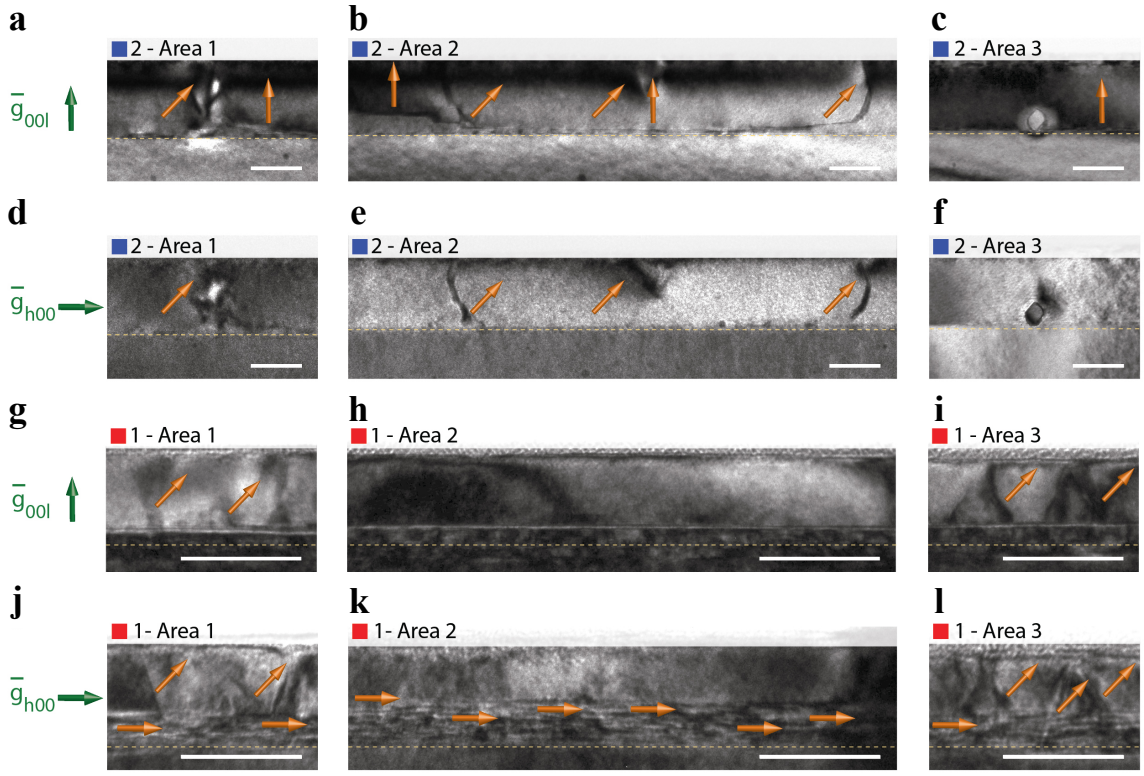

Figure 5.18 TEM g dot b analysis on SRO_{214} films. a-l, $\vec{g} \cdot \vec{b}$ analysis by bright field TEM showing dislocations on three areas of a lamella from superconducting (t = 66 nm) (**a-f**) and metallic (t = 41 nm) (g-l) SRO_{214} films (marked as "*" in **Figure 5.16** and **Figure 5.17**). The diffraction vectors $\vec{g}_{00l}$ and $\vec{g}_{h00}$ are indicated by green arrows and $\vec{b}$ by orange arrows (horizontal: in-plane edge dislocations, vertical: out-of-plane screw dislocations, tilted: mixed dislocation). The interface thin-film/substrate is marked with a yellow dotted line. Scale bar in **d-o,** 50 nm.

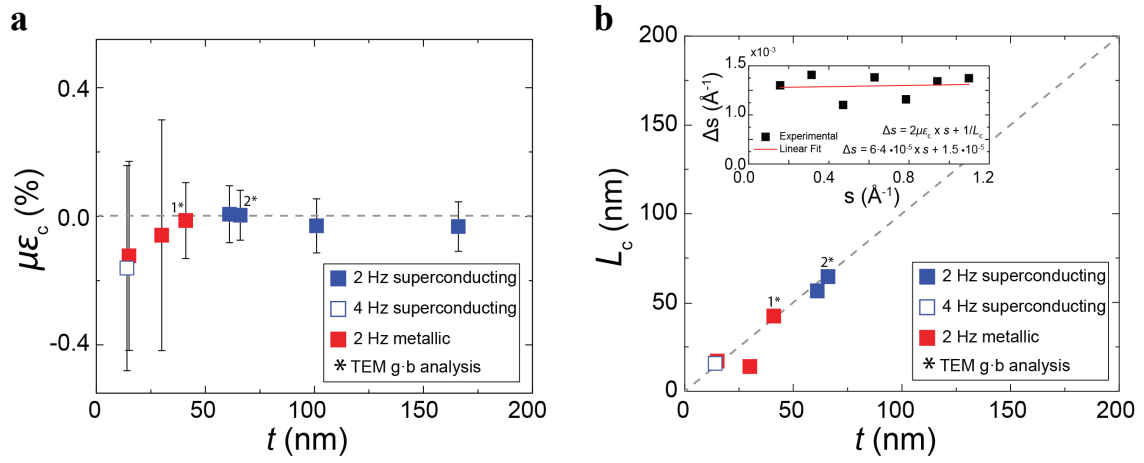

Figure 5.19 Microstrain and crystallite size out-of-plane of SRO_{214} thin-films. a,b, t dependence of $\mu\varepsilon_c$ (**a**) and L_c (**b**). Each contribution is separated from the total $FWHM_{2\theta-\omega}$ of (0 0 l) diffraction planes, by fitting the plotted data in reciprocal space units, as indicated in the example for t = 63 nm in the inset of **b**.

In the out-of-the plane direction, **Figure 5.19** depicts the values of $\mu\varepsilon_c$ and L_c for different t of SRO_{214} thin-films, calculated following the procedure shown in the example of the inset of **Figure 5.19b** for t = 63 nm. Negative values of $\mu\varepsilon_c$, which are not physically possible by

definition, together with the large error bars can be due to poor peak fittings and/or noisy data (due to insufficient time per step when collecting the data or the low number of steps). This prevents us from being able to identify if there is any correlation between $\mu\varepsilon_c$ and t, and subsequently with the electrical properties. Besides the presence of dislocations, L_c is very close to t, with modest variations, which as well could be related to the accumulated error in the measurements.

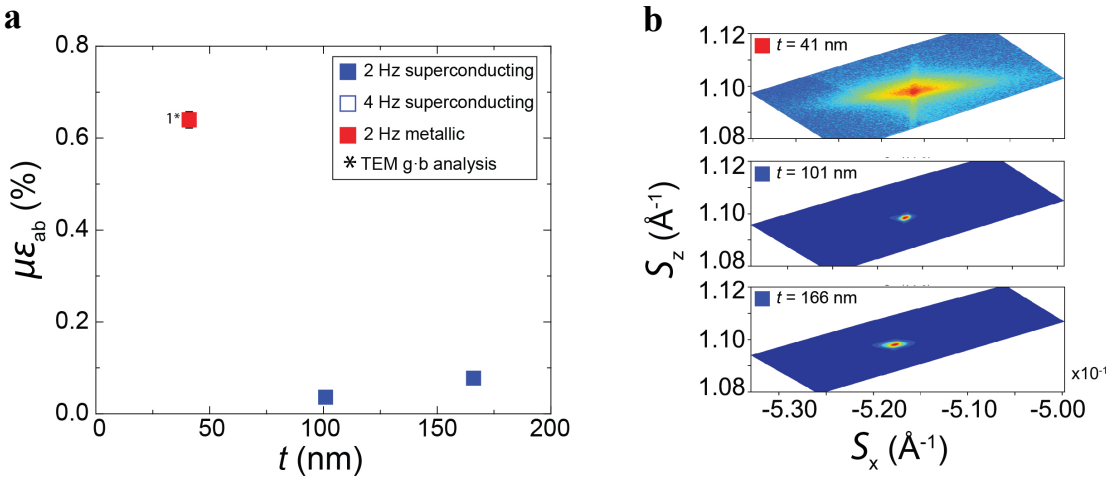

Figure 5.20 In-plane dependence of microstrain with the thickness of SRO_{214} thin-films and the RLP where the data has been extracted. a, Correlation between $\mu\varepsilon_{ab}$ and t, calculated from **b**, the reciprocal space maps of the (2 0 14) planes.

In the in-plane direction, $\mu\varepsilon_{ab}$ is extracted from the total broadening of the RLP (2 0 14), knowing the contribution from the degree of tilt for each t (**Figure 5.16a**) and neglecting the broadening due to L_{ab} (in the micro meter scale). We observe that the $\mu\varepsilon_{ab}$ is larger in the non-superconducting sample, which is in agreement with the higher concentration of dislocations and degree of twist. This can be visualized in the RLP (**Figure 5.16b**), in which the broadening in the S_x direction is affected by twist and $\mu\varepsilon_{ab}$, and in the Sz direction mainly by tilt and L_c, since and $\mu\varepsilon_c$ was almost zero.

However, from calculations of $\mu\varepsilon_{ab}$ on eight thin-films with different t, only the $\mu\varepsilon_{ab}$ of three samples can be provided (see **Figure 5.20a**). In the five remaining samples, the broadening due to tilt in the S_x direction, Δs_{Tilt_x}, is larger than the total broadening from the RLP of (2 0 14) planes ($\Delta s_x < \Delta s_{Tilt\_x}$), which is not physically possible (see **Figure 5.8** for clarity). This could be because the small amount of $\mu\varepsilon$ is easily affected by noise in the data (due to insufficient recording time) or inaccurate peak fit (due to the software limitations).

Finally, the values of in- and out-of-plane strain, ε_{ab} and ε_c respectively are calculated. From **Figure 5.21a**, it is concluded that there is no correlation between non-superconducting samples and the percent ε_{ab}, since ε_{ab} is close to zero except for two samples, following the good in-

plane matching with the LSAT (0.07 %). **Figure 5.21b** shows the values of ε_c calculated from two methods. One from the RLP (2 0 14) (as for the case of ε_{ab}) and other from the peak position of the (0 0 *l*) diffraction peaks in a 2θ-ω scan (which is more accurate since it considers error due to different diffracting angles). From the results, it can be infered that there is a larger distortion in the *c*-axis for thinner films (< 50 nm) compared to thicker films whose *c*-axis is close to bulk values. Based on the large out-of-plane mismatch between the SRO_{214} thin-film and the LSAT substrate (69.64 %), the first layers deposited have larger strain since they try to match the LSAT, whereas thicker thin-films are more relaxed with values close to SRO_{214} bulk. This might not affect directly the electrical properties since the current flows mainly in the in-plane direction.

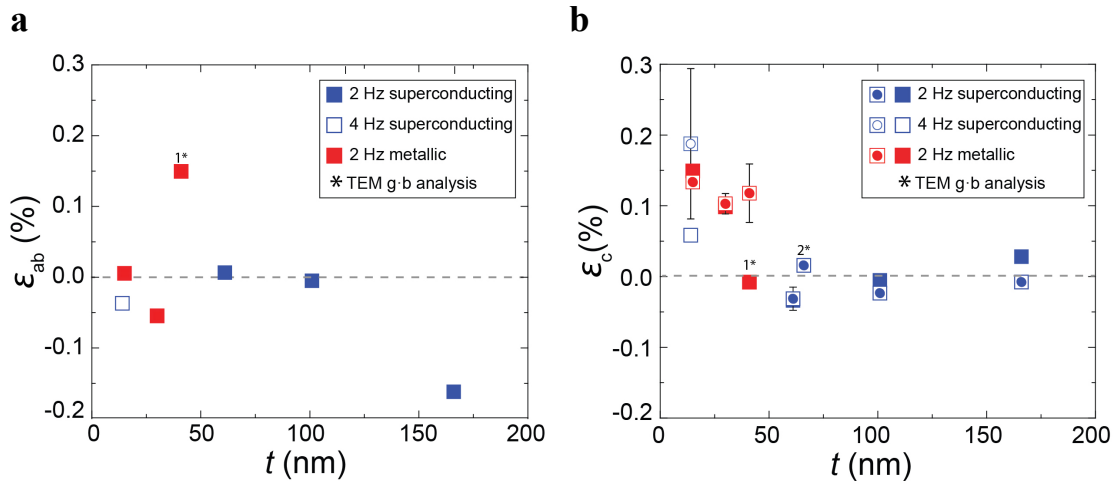

Figure 5.21 Strain in- and out-of-plane for different *t* of SRO_{214} thin-films. a, Strain in-plane, ε_{ab}, calculated from the RLP (2 0 14) and **b**, strain out-of-plane, ε_c, calculated from the RLP (2 0 14) and also by 2θ-ω scan of the (0 0 *l*) diffraction peaks (boxes with a circle).

5.5 Conclusions

We have systematically investigated the relationship between the structure and electrical properties of SRO_{214} thin-films grown on LSAT by pulsed laser deposition from a single crystal SRO_{327} target. To identify the nature of the structural defect that suppresses superconductivity on thin-films below 50 nm, bulk defects (impurities) are studied, followed by linear and planar defects (misorientations, dislocations, microstrain, and strain), as potential sources for superconductivity suppression.

Regarding different impurities, the analysis of the microstructure by TEM revealed that RuO_2 or Ru phases are not linked to the metallic sample. However, the non-superconducting sample has a depleted region free or Ru, meaning that the Ruddlesden-Popper phase of Sr_2RuO_4 might be separated into a phase rich in Sr and SRO_{113} or SRO_{327}. The magnetic moment

characteristic confirms that there is no SRO_{113}, and if there would be any SRO_{327}, the layer would have a thickness below 0.3 nm. We confirm that the un-labelled diffracted peak matches SRO_{327} composition and quantity. However, since this diffracted peak is also present in superconducting thin-films, the possibility of SRO_{327} phase suppressing the T_c is excluded.

At a smaller scale, small misorientations between crystallites, tilt and twist, are investigated. The results show a direct correlation between the degree of twist and the suppression of T_c (or equivalently, the enhancement of residual resistivity), which is also consistent with larger microstrain in-plane. No correlation with tilt (or microstrain out-of-plane) was observed. We confirm the presence of the dislocations in the microstructure and identify their nature by TEM g.b analysis. Additionally, it is observed that thinner thin-films have larger out-of-plane strain due to the large mismatch with the LSAT substrate.

Additionally, a faster laser repetition rate may reduce the degree of crystallographic twist. However, due to the lack of evidence to confirm the role of the laser frequency, we encourage further analysis of the influence of laser frequency in future research.

Therefore, based on the evidence provided, it is concluded that the absence of superconductivity in films thinner than 50 nm is correlated with the in-plane misorientation mosaic twist, linked to in-plane screw dislocations (and the consecutive in-plane microstrain), with the most defective region near the SRO_{214}/LSAT interface. And the possibility of impurities or strain responsible for the suppression of the superconducting transition is excluded.

Chapter 6

Conclusions and Future work

This work reviews the steps taken in the development of a reliable growth protocol to fabricate superconducting Sr_2RuO_4 thin films by pulsed laser deposition, and identifies the nature of the crystallographic defect responsible for the suppression of superconductivity. These results set an end to the lack of reproducibility encountered during the past 20 years, and opens the possibility to the fabrication of devices for a better understanding of the underlying physics of this unconventional superconductor.

The main conclusions extracted from this thesis are summarized as follows:

- Superconductivity is achieved on Sr_2RuO_4 thin films when the conventional $Sr_2Ru_{1.15}O_4$ poly-crystalline target is replaced with a $Sr_3Ru_2O_7$ single-crystal.
- The optimal growth conditions are obtained on films deposited on (0 0 1) LSAT substrate at 950˚C, with an O_2 pressure of 0.35 Pa, laser fluence of 1.0 J cm^{-2} with a repetition rate of 2 Hz.
- Investigation of the thickness dependence on the superconducting critical temperature reveals a critical thickness (~ 50 nm) below which thin films are partially or not superconducting (metallic).
- Magnetic characterization of the films confirms that the suppression of superconductivity is not related to impurities (as commonly observed in the literature for Sr_2RuO_4 single crystals) such as RuO_2, $SrRuO_3$, $Sr_3Ru_2O_7$ or $Sr_4Ru_3O_{10}$.

- The correlation between the analysis of defects performed by X-ray diffraction and the electrical properties, shows a connection between in-plane misorientation “twist” and the lack of superconductivity observed on thin films below the critical thickness.

- TEM g dot b analysis corroborates the results from X-ray diffraction, and identifies the nature of the dislocations associated to the larger degree of twist observed in metallic films, with in-plane screw dislocations.

- In contrast to observations in the literature in another unconventional superconductor (YBCO), the out-of-plane misorientation “tilt” does not suppress the superconductivity on Sr2RuO4 thin films.

- In addition, this work opens the possibility for further optimization of the growth of Sr_2RuO_4 thin films such as the investigation of the effect of the laser repetition rate. In this thesis it is observed on one thin film that doubling the laser repetition rate (4 Hz) reduces the degree of twist. If this correlation is confirmed, it would imply that superconductivity on Sr_2RuO_4 thin films can be achieved also below the critical thickness (> 50 nm).

- Further optimization of the growth conditions on alternative the substrate $Sr_2Ru_{0.98}Ti_{0.02}O_4$. Studying an alternative substrate with an improved out-of-plane mismatch can contribute to the reduction of defects on the film occurring at the interphase; commonly observed when using LSAT. Since this project already succeeded on the growth of metallic, single-phase Sr_2RuO_4 thin films on $Sr_2Ru_{0.98}Ti_{0.02}O_4$ substrates, we believe that with an additional refinement superconductivity could also be achieved on this alternative target.

- Investigating the growth of Sr_2RuO_4 thin films on the alternative substrate Sr_2TiO_4 crystals. In this work, the preparation of Sr_2TiO_4 crystals fabricated by Prof. Y. Maeno is presented. However, the challenge relies on the fact that the single crystalline regions, that make them ideal substrates for Sr_2RuO_4 based on the good lattice matching, have a reduced size.

After reflecting about the successful results on the optimization of the growth conditions achieved (**Chapter 4** and **5**), when going back to the initial work (**Chapter 3**), we consider that a few points should be included as learned experience:

- Electrical characterization using Au contacts. The initial electrical characterization of the films shown in **Chapter 3** is performed directly by placing the contacts on the surface. Based on the lack of homogeneity that the thin films have; the results are very

dependent on the location of the electrodes. This could have been avoided by depositing electrical contact as on the films on **Chapter 4** and **5**.

- Study of the laser fluence. As shown in **Chapter 4**, the laser fluence is one of the determinant parameters to achieve single phase of Sr_2RuO_4. Therefore, the investigation of the effect of the laser fluence on the thin films of **Chapter 3**, could have helped in the reduction of impurity phases.

- Control of the thickness. **Chapter 5** summarizes the effect of the thickness on the superconducting properties, highlighting the existence of a critical thickness (~ 50 nm) below which the superconductivity is suppressed. In **Chapter 3**, most of the films are deposited with a fix number of pulses, and with the main focus on the reduction of the impurity phases and its correlation with the electrical properties. A careful control over the thickness could have led to the observation of superconductivity if the films were thick enough.

Besides the growth optimization, it would be of interest to investigate the superconducting symmetry by performing experiments that were limited in the past by the use of single crystals. For instance, with measurements that are sensitive to the superconducting symmetry, such as Josephson junctions of Pb/SRO_{214}/Pb. Since Pb is a conventional superconductor (s-wave), when coupled to SRO_{214}, a drop in the critical current should be expected below the T_c of SRO_{214} due to the symmetry incompatibility. This experiment was performed by R. Jin *et al.*[38] and later re-investigated by R. Nakagawa *et al.*[10] However, in both cases, the Josephson junctions were fabricated with SRO_{214} single crystals that contained Ru inclusions (superconducting below 3 K) which could have interfered with the electrical contacts and affect the results. Therefore, we believe that it would be of interest to remove the variability of Ru by replacing the single crystal with SRO_{214} thin films.

COMMUNICATIONS MATERIALS

ARTICLE

https://doi.org/10.1038/s43246-020-0026-1 OPEN

Pair suppression caused by mosaic-twist defects in superconducting Sr_2RuO_4 thin-films prepared using pulsed laser deposition

Carla Maria Palomares Garcia [1], Angelo Di Bernardo [1], Graham Kimbell [1], Mary E. Vickers[1], Fabien C-P. Massabuau[1,2], Sachio Komori[1], Giorgio Divitini [1], Yuuki Yasui [3], Han Gyeol Lee[4,5], Jinkwon Kim[4,5], Bongju Kim[4,5], Mark G. Blamire [1], Antonio Vecchione[6], Rosalba Fittipaldi[6], Yoshiteru Maeno[3], Tae Won Noh [4,5] & Jason W. A. Robinson [1✉]

Sr_2RuO_4 (SRO_{214}) is a prototypical unconventional superconductor. However, since the discovery of its superconductivity a quarter of a century ago, the symmetry of the bulk and surface superconducting states in single crystal SRO_{214} remains controversial. Solving this problem is massively impeded by the fact that superconducting SRO_{214} is extremely challenging to achieve in thin-films as structural defects and impurities sensitively annihilate superconductivity. Here we report a protocol for the reliable growth of superconducting SRO_{214} thin-films by pulsed laser deposition and identify universal materials properties that are destructive to the superconducting state. We demonstrate that careful control of the starting material is essential in order to achieve superconductivity and use a single crystal target of $Sr_3Ru_2O_7$ (SRO_{327}). By systematically varying the SRO_{214} film thickness, we identify mosaic twist as the key in-plane defect that suppresses superconductivity. The results are central to the development of unconventional superconductivity.

[1] Department of Materials Science & Metallurgy, University of Cambridge, 27 Charles Babbage Road, Cambridge, United Kingdom. [2] Department of Physics, SUPA, University of Strathclyde, Strathclyde, United Kingdom. [3] Department of Physics, Graduate School of Science, Kyoto University, Kyoto 606-8502, Japan. [4] Center for Correlated Electron Systems, Institute for Basic Science (IBS), Seoul 08826, Republic of Korea. [5] Department of Physics and Astronomy, Seoul National University, Seoul 08826, Republic of Korea. [6] Consiglio Nazionale delle Ricerche, SPIN, Via G. Paolo II 132, I-84084 Fisciano, Italy. ✉email: jjr33@cam.ac.uk

The past decade has seen rapid developments in the understanding of unconventional superconductivity, particularly in proximity-coupled systems involving conventional *s*-wave superconductors in combination with magnetic materials and interfaces with strong spin-orbit coupling[1]. Highlights include the discovery of odd-frequency (*s*-wave) spin-triplet pairing at *s*-wave superconductor/ferromagnet interfaces[2–10], evidence for electron-composite particle-antiparticles in nanowire devices with spin-orbit coupling and superconductivity[11,12], and surface superconductivity in Au with Fermi-level tuning via a ferromagnetic dielectric[13].

Parallel research on intrinsic unconventional superconductivity in superfluid He and in compounds such as Sr_2RuO_4 (SRO_{214})[14,15] has also made dramatic advances. Single crystal SRO_{214} has a superconducting critical temperature[16] (T_c) of 1.5 K. Although the underlying nature of the superconducting state in SRO_{214} crystals remains highly controversial, the consensus from experiments and theory is that the pairing is unconventional and potentially chiral *p*-wave state with the *d*-vector perpendicular to the basal plane[17], which is even-frequency and conceptually different from the odd-frequency spin-triplet pairing induced at *s*-wave superconductor/ferromagnetic interfaces. Muon spin-relaxation measurements[18,19] on SRO_{214} show evidence for time-reversal symmetry breaking below T_c while early nuclear magnetic resonance spectroscopy[20,21] and polarized neutron scattering[22] experiments have demonstrated a constant in-plane spin susceptibility (Knight shift) below T_c. However, a constant out-of-plane spin susceptibility below T_c goes against a chiral *p*-wave state[17]. Furthermore, recent nuclear magnetic resonance spectroscopy on SRO_{214} crystals show that the Knight shift decays in the superconducting state in the "3 K phase" under uniaxial stress as well as in the "1.5 K phase" without stress[23], consistent with a *d*-wave or helical *p*-wave state.

Although there is a lack of experimental consistency in the underlying superconducting symmetry of SRO_{214}, unconventional pairing states are expected on the surface due to broken inversion symmetry, which raises the prospect of coupling different superconducting symmetries via proximity effects with *s*-wave or even *d*-wave superconductors. Nevertheless, developing a full understanding of the superconductivity in SRO_{214} including proximity-based experiments is fundamentally limited by the fact that thin-film growth of SRO_{214} has proven to be extremely challenging. A robust, reliable, growth protocol for SRO_{214} thin-films is therefore required in order to break the deadlock and enable detailed studies of the electron pairing in SRO_{214} and the mixing of different superconducting symmetries in hybrid Josephson junctions.

One of the key issues for growing superconducting films of SRO_{214} relates to the destructive nature of magnetic or non-magnetic impurities and structural defects. In thin-films, the concentration of impurities and structural defects tends to be high and superconductivity is suppressed or localized to pristine regions[24–27]. Currently, there exist only a few reports of superconducting SRO_{214} thin-films, but control continues to be severely limited because the underlying materials properties required for superconductivity remain poorly understood. The first successful report of a superconducting thin-film of SRO_{214} nearly a decade ago was fabricated by pulsed laser deposition from a stoichiometric (polycrystalline) target of SRO_{214} on (0 0 1) $(La_{0.3}Sr_{0.7})(Al_{0.65}Ta_{0.35})O_3$ (LSAT) single crystals, and required high-temperature layer-by-layer growth[28]. This work was later reproduced by our group[29] in one sample albeit with an extremely broad (1.6 K) superconducting transition and an elevated T_c of 1.9 K. This result indicated inhomogeneous superconductivity due to out-of-plane defects from stacking faults that create local strain, which locally enhances T_c. Recently, superconducting films of SRO_{214} have been grown by molecular beam epitaxy on LSAT with a T_c of 1.1 K using a Ru-rich flux during growth to reduce Ru loss[30]. The T_c was further enhanced to 1.9 K by depositing onto single terminated (1 1 0) $NdGaO_3$ due to the associated misfit strain[31].

In this article we set out to develop a protocol for the reliable growth of superconducting SRO_{214} thin-films by pulsed laser deposition and to establish and control key materials properties that are destructive for superconductivity. This is achieved using careful control of the starting material, which consists of a single crystal target of $Sr_3Ru_2O_7$ (SRO_{327}). We establish that mosaic twist is a universal structural (in-plane) defect that destroys superconductivity in SRO_{214}. This is clearly different from the planar defects (out-of-phase boundaries) reported by Krockenberger[28]. By controlling the degree of mosaic twist in the SRO_{214} films, and the associated dislocations that form at the SRO_{214}/substrate interface, we demonstrate a reliable protocol for depositing superconducting SRO_{214}.

Results

Growth optimization of SRO_{214} thin films. A single crystal target of SRO_{327} provides 33% Ru excess that compensates for Ru loss during the high-temperature growth of SRO_{214} which, in conjunction with fine-control of laser fluence[32] (see Supplementary Fig. 1 for results using a polycrystalline target of SRO_{214}), reduces the volume fraction of impurity phases present in the films. The single crystal target of SRO_{327} (see compositional analysis in Supplementary Fig. 2a) has a surface area of $3 \times 10\ mm^2$ and is mounted on a polycrystalline SRO_{214} holder (Fig. 1a). Laser alignment is optimized by focusing the laser spot (1.5 mm diameter) onto the SRO_{214} holder prior to ablating from the SRO_{327} target. During film growth, the rotation of the SRO_{327} target is fixed and the target carousel is twisted through an angle β to erode the SRO_{327} target along a line (Fig. 1b). All SRO_{214} films discussed in this paper are deposited onto heated (950°C) LSAT (0 0 1) as described in the Methods section. Most of the films are grown using a laser pulse frequency of 2 Hz with one sample grown at 4 Hz as discussed at the end of the paper. To minimise in-plane epitaxial strain, SRO_{214} (in-plane lattice constant = 0.3873 nm) is grown on LSAT (in-plane lattice constant = 0.387 nm) substrates, and a substrate miscut angle of less than 0.05° is used to reduce the concentration of out-of-plane stacking faults at step edges.

We first discuss the effect of varying oxygen pressure (P_{O2}) during growth. SRO_{214} films are grown using a fixed number of laser pulses (5000) at 2 Hz and laser fluence of $1.0\ J\ cm^{-2}$ to achieve a thickness (t) around 23 nm (depending on P_{O2}). Values of t are estimated by fitting thickness fringes to the (0 0 6) diffraction peak of SRO_{214} (see Supplementary Note 1 and Supplementary Fig. 3). In Fig. 1c we have plotted X-ray diffraction traces from three representative SRO_{214} films grown using 1.0 Pa, 0.35 Pa and 0.09 Pa of oxygen. For the $P_{O2} = 1.0$ Pa film, thickness fringes are barely visible on the $(0\ 0\ 6)_{214}$ peak and an SRO_{327} impurity phase is present (highlighted in green). The $P_{O2} = 0.35$ Pa film, however, shows no detectable evidence for SRO_{327} or other impurity phases and the $(0\ 0\ 6)_{214}$ peak shows clear fringes, indicating uniform growth. Reducing P_{O2} further to 0.09 Pa promotes secondary phases in the Ruddlesden-Popper series (indicated by magenta) such as SRO_{327}, SRO_{4310} or RuO_2. While thin films deposited above or below $P_{O2} = 0.35$ Pa show metallic behavior with no detectable evidence for superconductivity down to 300 mK, the $P_{O2} = 0.35$ Pa film shows a downturn in $R(T)$ below 0.5 K, consistent with the onset of incipient superconductivity (Supplementary Fig. 4a). The corresponding lattice parameters are $a = 0.3870(3)$ nm (from RSM on (2014)

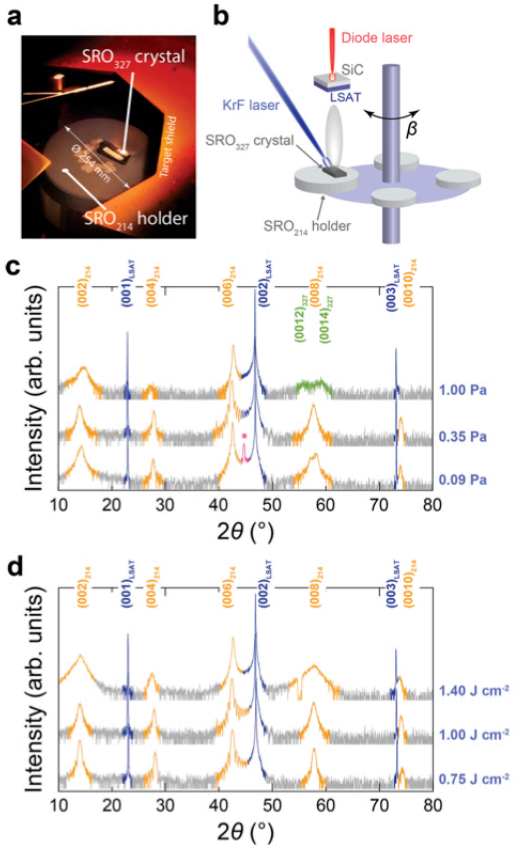

Fig. 1 Pulsed laser deposition setup and structural properties of Sr_2RuO_4 thin films. a A photograph showing a single crystal $Sr_3Ru_2O_7$ target mounted on a polycrystalline Sr_2RuO_4 holder. **b** A schematic illustration of the pulsed laser deposition setup, where the rotation of the target carousel is labelled "β" **c**, **d** X-ray diffraction traces for Sr_2RuO_4 grown at 950°C under different O_2 pressures (labelled) with a fixed fluence of 1.0 J cm^{-2} (**c**) and equivalent traces in which Sr_2RuO_4 is grown at 950°C using different laser fluences (labelled) with a fixed oxygen pressure of 0.35 Pa (**d**). The diffraction planes for Sr_2RuO_4 (orange) SRO_{327} (green), and $(La_{0.3}Sr_{0.7})(Al_{0.65}Ta_{0.35})O_3$ (LSAT) (blue). The peak marked "*" corresponds to the diffraction plane of the Ruddlesden-Popper series $(0\ 0\ 10)_{327}$, $(0\ 0\ 14)_{4310}$ or $(2\ 1\ 0)$ diffraction plane of RuO_2. The subindexes 214, 327 and 4310 refer to Sr_2RuO_4, $Sr_3Ru_2O_7$ and $Sr_4Ru_3O_{10}$, respectively.

plane) and $c = 1.2738(17)$ nm (from a 2θ-ω scan on the $(0\ 0\ l)$ peak positions after applying a correction for sample displacement).

Using $P_{O2} = 0.35$ Pa, we now discuss the effect of laser fluence on the structural and electrical properties of SRO_{214}. In Fig. 1d we have plotted X-ray diffraction traces from three films grown using laser fluences of 0.75 J cm^{-2}, 1.0 J m^{-2} and 1.4 J cm^{-2}, with a fixed number of laser pulses (5000). The traces show sharper peaks with decreasing laser fluence, indicating improved structural properties (vertical microstrain). The in-plane resistance versus temperature $R(T)$ for the 1.4 J cm^{-2} film saturates to a constant minimum below 10 K with no evidence for superconductivity down to 300 mK. In contrast to the 1 J cm^{-2} film, the 0.75 J cm^{-2} film shows sharper diffraction peaks, but a downturn in $R(T)$ is not observed, even down to 300 mK (Supplementary Fig. 4b). This is likely due to the lower laser fluence reducing Ru ablation from the SRO_{327} target[32] and hence, the SRO_{214} film is deficient in Ru, which prevents superconducting behaviour[29,30].

Characterization of superconducting properties. We now discuss electrical transport of SRO_{214} films versus t in the 15 nm to 166 nm range using optimized growth parameters (oxygen pressure of 0.35 Pa and fluence of 1.0 J cm^{-2}). For each film we investigate $R(T)$ and for those that show a superconducting transition, we define T_c as the temperature halfway through the resistive transition. In Fig. 2a we have plotted $T_c(t)$ where the vertical error bars represent the temperature width of the superconducting transition (See Supplementary Fig. 5). These data show a critical thickness for superconductivity of approximately 50 nm with T_c rising to 1.05 K for $t = 166$ nm (Fig. 2a). Although the largest T_c is lower than the T_c of bulk SRO_{214} single crystals (1.5 K[16]), T_c values are higher than previous reports for SRO_{214} films grown by pulsed laser deposition (Supplementary Fig. 6a).

In Fig. 2b we have plotted the t-dependence of the residual resistivity ratio (RRR), defined at the resistance at room temperature divided by the saturated minimum in resistance at low temperature before the onset of superconductivity. $RRR(t)$ broadly divides into two regimes: for $t < 50$ nm, RRR is low (<30) with metallic transport down to 300 mK (highlighted in red); for $t > 50$ nm, RRR rapidly increases with increasing t with superconducting transport at low temperature (highlighted in blue). The low $RRR(t)$ values in the metallic regime cannot be simply explained on the basis of a thin-film effect or t approaching the out-of-plane superconducting coherence length of SRO_{214} which we estimate to be ξ_c ~3–8 nm (see Fig. 2c and Supplementary Note 2). The metallic regime indicates a large density of defects due to impurity phases in conjunction with structural defects (e.g. mosaic tilt or mosaic twist), consistent with the high (low) values of residual resistivity (ρ_0) for the films with a low (high) RRR as shown in Fig. 2d. In the superconducting regime, RRR reaches 110 for $t = 100$ nm, which is high relative to equivalently-thick SRO_{214} films reported elsewhere (Supplementary Fig. 6b).

Analysis of the microstructure. To identify the underlying mechanisms which suppress superconducting behavior in SRO_{214} films, we have systematically investigated the potential presence of structural defects that may affect long-range crystal order. We first discuss scanning transmission electron microscopy (STEM), high resolution scanning transmission electron microscopy (HR-STEM) and energy-dispersive X-ray (EDX) maps acquired on a SRO_{214} superconducting film (Fig. 3a–f) and a metallic film (Fig. 3g–l) (see Methods). We compare STEM (Fig. 3a, g) and HR-STEM micrographs which demonstrate coherent c-axis growth (Fig. 3b, l). For those films that show a full superconducting transition, the micrographs reveal inclusions near the SRO_{214}/LSAT interface (Fig. 3a). These crystalline (Fig. 3f) inclusions are elemental Ru (Fig. 3c–e) or Ru oxide (Supplementary Fig. 7) and spaced over distances larger than ξ_{ab} and so should not directly affect T_c.

For the SRO_{214} films that do not show a full superconducting transition, STEM maps consistently reveal a 1–2-nm-thick region above LSAT (indicated with an arrow) that has mixed stoichiometry (Fig. 3g). STEM-EDX confirms that this region has the correct Sr atomic concentration for SRO_{214}, but is deficient in Ru and rich in O (Fig. 3i–k). This is further confirmed by HR-STEM on different areas of the film (Fig. 3h,l), which show atomic layers of decreased concentration of heavy atoms, and stoichiometric SRO_{214} layers above and below this region (Fig. 3g)

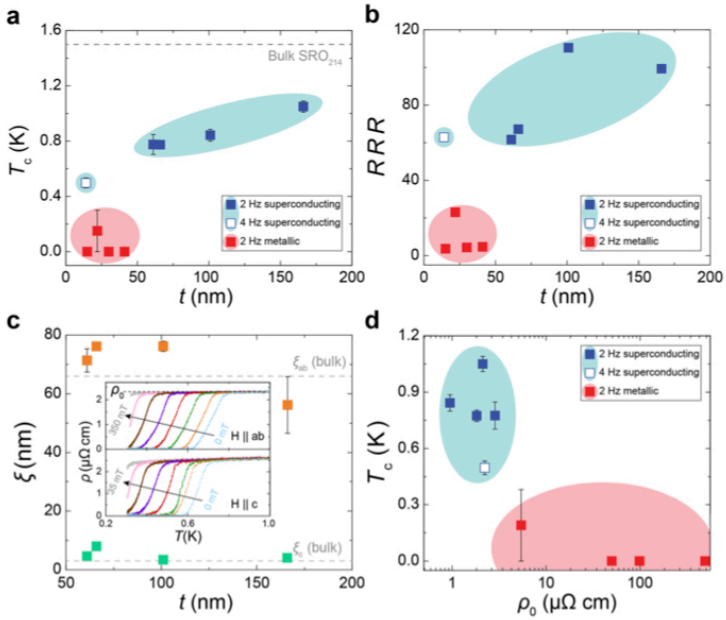

Fig. 2 Electronic transport properties of Sr_2RuO_4 films. a, **b** Thickness (t) dependence of the critical temperature T_c (**a**) and residual resistivity ratio *RRR* (**b**). Filled squares correspond to films grown with a laser frequency of 2 Hz and the hollow square at 4 Hz. **c** Superconducting coherence length in-plane ξ_{ab} (orange squares) and out-of-plane ξ_c (green squares) for multiple films versus t, determined from resistivity versus temperature measurements with a magnetic field applied along the ab-plane or the *c*-axis directions, respectively. **d** T_c versus residual resistivity ρ_0 for superconducting and metallic films marked as in (**a**) and (**b**). In all plots, background shading indicates a full superconducting transition (blue) or metallic (red) behaviour at low temperatures with or without incipient superconductivity.

(similar case observed in[33]). This depleted region most likely forms due to a separation of the Ruddlesden-Popper phase of SRO_{214} into layers of SRO_{113} or SRO_{327} [34] (ferromagnetic and paramagnetic, respectively, with a perovskite structure), and SrO (rock salt unit cell). In the oxidizing atmosphere used during growth, SrO can stabilize into SrO_2 leading to O-rich and Ru-deficient regions matching the results extracted from EDX at the interface.

We note that SRO_{113} and SRO_{327} impurities are an issue for SRO_{214} single crystals since the ferromagnetic exchange field of these phases can suppress superconductivity[26]. To investigate the presence of SRO_{113} as well as SRO_{327}, we have measured the temperature dependence of the magnetic moment $m(T)$ of the non-superconducting SRO_{214} films (Supplementary Fig. 8). We compare these data to a control sample of bare LSAT that has been exposed to matching conditions as SRO_{214}/LSAT films during growth but without SRO_{214} deposited on the LSAT. $m(T)$ shows no evidence for SRO_{113} since no ferromagnetic transition[35] is observed at or below the expected Curie temperature of 160 K or a maximum at 16 K due to SRO_{327} (Supplementary Fig. 8a). We also investigated magnetization hysteresis loops $m(H)$ at a range of temperatures (20–300 K) with the applied field (H) directed normal to the LSAT substrate. For all T investigated, m is constant and matches the moment of bare LSAT within an error of 1 μemu (Supplementary Fig. 8a inset and 8b). This rules out the presence of ferromagnetic SRO_{113} and would explain the XRD peak marked as "*" in Fig. 1c corresponding to SRO_{327}. Nevertheless the SRO_{327} is not consistently observed and its presence/absence does not correlate with superconductivity. The possible SRO_{327} phase would be concentrated at the SRO_{214}/LSAT interface in the initial growth, considering the thickness dependence of our superconducting films. Such intergrowth could be controlled later by changing the dynamic nature of PLD. Further studies are highly desirable. Additionally, since STEM-EDX confirms stoichiometric Ru content[36] on the SRO_{214} thin films (see example in Supplementary Fig. 2b), our study focuses on the analysis of structural defects that could alter the superconducting transition.

Degree of tilt and twist. Another potential source of crystallographic defects that may suppress superconductivity relate to misoriented crystalline regions. This can be visualized with the mosaic crystal model, in which the film is described as the combination of smaller crystallites (blocks), misoriented with respect to each other and the substrate. A rotation of these blocks about an axis parallel to the surface is known as mosaic tilt, and a rotation about an axis perpendicular to the surface is known as mosaic twist. Tilted and twisted blocks are separated by low-angle grain boundaries consisting of dislocations, which can be edge- or screw-like, with a Burgers vector (***b***) perpendicular or parallel to the dislocation line vector (***u***), respectively (see Supplementary Fig. 9), and cause local variations of interplanar distance (microstrain) at grain boundaries. Tilt can be measured from the full width half maximum in omega ($FWHM_\omega$) of the (0 0 l) diffracting planes by X-ray diffraction in a symmetric (coplanar) geometry. Values of tilt extracted from SRO_{214} films with different t show that all films (superconducting or non-superconducting), with the exception of one, have similar values of tilt. Tilt does not therefore affect the electrical properties SRO_{214} films (see Supplementary Fig. 10a–c).

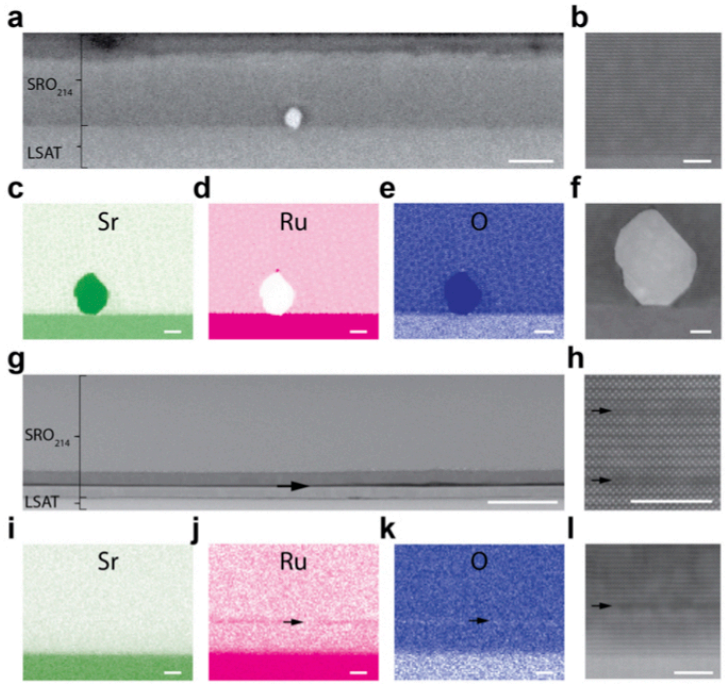

Fig. 3 Structural and chemical properties of Sr_2RuO_4 films. a–f Scanning transmission electron microscopy STEM micrographs of a superconducting film of a thickness $t = 66$ nm (**a**) showing inclusions at the $Sr_2RuO_4/(La_{0.3}Sr_{0.7})(Al_{0.65}Ta_{0.35})O_3$ (LSAT) interface and high resolution HR-STEM of an area close to the same interface in (**b**). EDX maps of the inclusions in **a** are shown in **c**–**e** for Sr (**c**), Ru (**d**) and O (**e**) with a HR-STEM micrograph of the inclusion in **f**. **g**–**l** STEM micrograph of a $t = 41$ nm metallic film (**g**) showing an interface layer of different stoichiometry (dark black line indicated with an arrow) to the rest of the film with corresponding energy-dispersive X-ray EDX maps for Sr (**i**), Ru (**j**) and O (**k**). **h**, **l** HR-STEM on an area of the Sr_2RuO_4 thin film (**h**) and $Sr_2RuO_4/(La_{0.3}Sr_{0.7})(Al_{0.65}Ta_{0.35})O_3$ interface (**l**) showing a decreased concentration of heavy atoms in some of the layers. **g**–**l** Depleted region indicated with arrows. The scale bars are **a**, 50 nm, **b**, **f**, **h**, **l** 5 nm, **c**, **d**, **e**, **l**, **j**, **k** 10 nm and **g**, 25 nm. Note that in (**c**–**e**) and (**i**–**k**), bright regions indicate higher atomic percent. The subindex 214 refers to Sr_2RuO_4 and LSAT corresponds to the substrate $(La_{0.3}Sr_{0.7})(Al_{0.65}Ta_{0.35})O_3$.

Twist can be measured using four different configurations: edge [by measuring the (h k 0) planes from the $FWHM_\omega$ with an offset in chi (χ_{offset}) of 90° (Fig. 4a)]; glancing angle in-plane; transmission; or skew geometry[37]. For our thin-film geometry we adopt the skew geometry (non-coplanar) configuration because the signal intensity is the strongest, and measure the $FWHM_\omega$ of the (4 1 3) diffracting planes, which provides a good estimate of twist due to the large χ_{offset} (>70°)[37,38]. The dependence of twist, $FWHM_\omega$ extracted from a pseudo-Voigt profile fit after the subtraction of the instrumental contribution (see Supplementary Note **3**), on t is shown on Fig. 4a. Since the in-plane crystallite size ($L_{||}$) is of the order of micrometres, its contribution to peak broadening is negligible (see Supplementary Fig. 10a). We observe that $FWHM_\omega$ (Fig. 4b inset), and hence the degree of twist, rapidly rises as t decreases below 50 nm, corresponding to the metallic films that do not show full superconducting transition (Fig. 4b). From Fig. 4c we demonstrate a direct correlation between twist and the suppression of superconductivity by a reduction (increase) of T_c (residual resistivity) when the degree of twist increases.

Identification of dislocations. The increase in twist with decreasing t (Fig. 4b) indicates a higher concentration of dislocations with $\boldsymbol{b}$ in-plane at low t for non-superconducting films. To confirm this and determine the nature of the dislocations, we have performed $\boldsymbol{g} \cdot \boldsymbol{b}$ TEM analysis, with $\boldsymbol{g}$ being the diffracted beam direction on a superconducting and non-superconducting film. In $\boldsymbol{g} \cdot \boldsymbol{b}$ TEM analysis, dislocations are in-contrast (visible) when $\boldsymbol{g} \cdot \boldsymbol{b} \neq 0$, but out-of-contrast (invisible) for $\boldsymbol{g} \cdot \boldsymbol{b} = 0$[39,40] as illustrated in Fig. 4a. Figure 4d–o shows $\boldsymbol{g} \cdot \boldsymbol{b}$ bright field TEM analysis performed on three different cross-sectional areas for the superconducting and non-superconducting films using two perpendicular diffraction vectors $\boldsymbol{g}_{00l}$ and $\boldsymbol{g}_{h00}$. The non-superconducting films shows a larger concentration of dislocations compared to the superconducting film. Furthermore, for the non-superconducting film the dislocations are mostly in-plane and screw-like with both $\boldsymbol{u}$ and $\boldsymbol{b}$ in- plane (horizontal orange arrow), as they can only be resolved when $\boldsymbol{b} \parallel \boldsymbol{g}_{h00}$ (Fig. 4d–f) and are extinct when $\boldsymbol{b} \perp \boldsymbol{g}_{00l}$ (Fig. 4g–i). These results are consistent with the high degree of twist observed in non-superconducting films and therefore demonstrate that horizontal screw dislocations are a key defect that strongly suppresses superconductivity in SRO_{214}. In contrast, the lower density of dislocations present in the superconducting film are in-plane edge-like with $\boldsymbol{u}$ in-plane and $\boldsymbol{b}$ out-of-plane (vertical orange arrow), as they are visible when $\boldsymbol{b} \parallel \boldsymbol{g}_{00l}$ (Fig. 4j–l) and not visible when $\boldsymbol{b} \perp \boldsymbol{g}_{h00}$ (Fig. 4m–o). In both the superconducting and non-superconducting films, a few threading mixed dislocations, with both edge and screw components (tilted orange arrow) are resolved with both $\boldsymbol{g}_{00l}$ and $\boldsymbol{g}_{h00}$. The presence of threading dislocations with a screw component is also revealed in topographic images acquired using an atomic force microscope (Supplementary Fig. 10d–g).

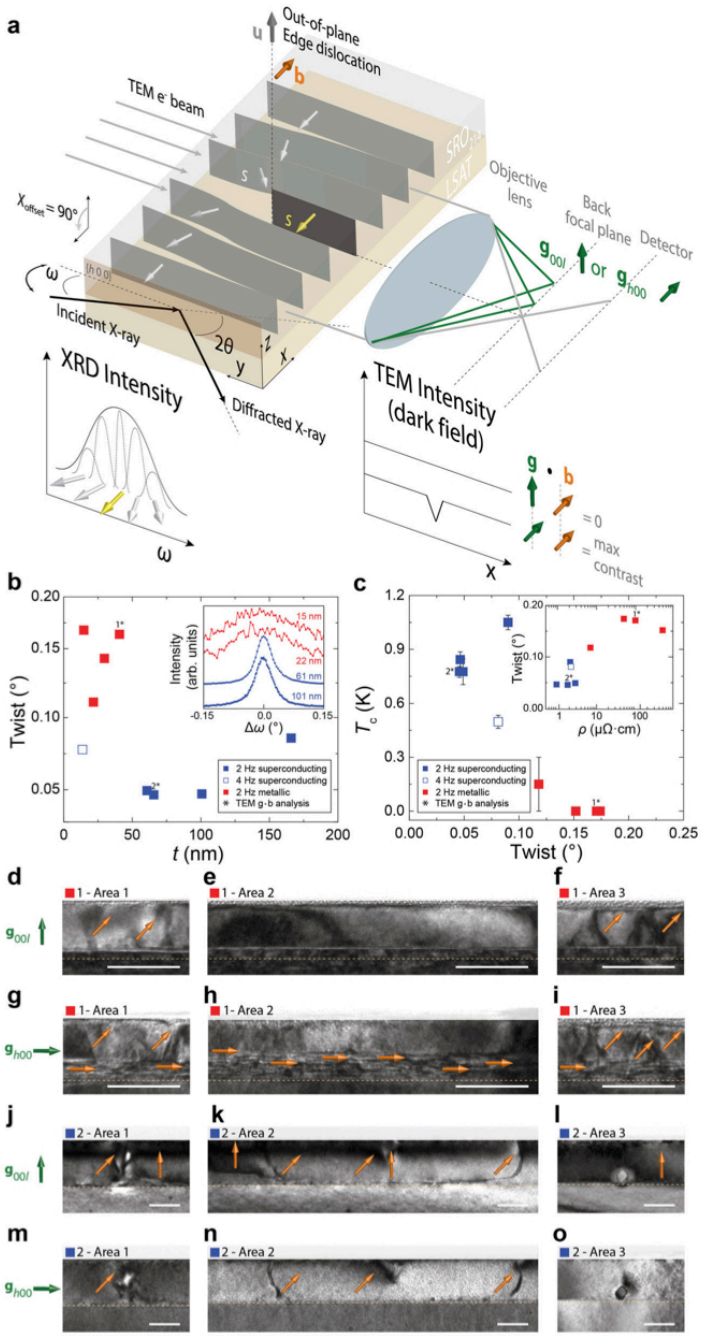

We note that, we cannot confirm that the white contrast in Fig. 3j located in the Ru-deficient layer (confirmed in Fig. 4g–i), is also dislocation related as it might be the result of a combination of features such as Ru-deficiency, interface effect and dislocations.

Finally, we note that the superconductivity in SRO_{214} can be further optimized by tuning additional growth parameters (not discussed in this paper) such as deposition frequency. We have tested the effect of doubling the laser pulse frequency to 4 Hz during SRO_{214} growth, while keeping the same growth conditions as for the rest of the study (oxygen pressure of 0.35 Pa, fluence of 1.0 J cm^{-2}, 950 °C), which has the effect of reducing the degree of twist (Fig. 4b) and the residual resistivity (Fig. 2d), and increasing T_c (Fig. 3a) and *RRR* (Fig. 3b), compared to equivalent films grown at 2 Hz.

Fig. 4 Nature of dislocations and their effect on superconductivity in Sr_2RuO_4 films. a An illustration of an edge dislocation with an out-of-plane line vector $\boldsymbol{u}$ (grey arrow) and Burgers vector $\boldsymbol{b}$ in-plane (orange arrow) on the (h 0 0) planes of SRO_{214}. The diagram also shows the X-ray diffraction setup in edge geometry (Tilt angle of the sample stage $\chi_{offset} = 90^\circ$) to measure the in-plane misorientation, twist, from the peak broadening in ω (angle between the X-ray incident beam and the diffracted planes) due to variations in the scattering direction (white and yellow arrows). Transmission electron microscopy TEM $\boldsymbol{g} \cdot \boldsymbol{b}$ analysis to reveal edge dislocations using bright field imaging with two perpendicular diffraction conditions ($\boldsymbol{g}_{00l}$ and $\boldsymbol{g}_{h00}$) is also shown. **b** Degree of twist versus thin-film thickness t, determined from the full width half maximum in ω $FWHM_\omega$ measured from χ_{offset} ~ 78° in skew symmetric on the (4 1 3) planes (inset curves are vertically offset for clarity). **c**, Superconducting critical temperature T_c versus and resistivity ρ versus twist (inset). **d**–**o** $\boldsymbol{g} \cdot \boldsymbol{b}$ analysis by bright field TEM showing dislocations on three areas of a lamella from metallic (**d**–**i**) and superconducting (**j**–**o**) SRO_{214} films (marked as three asterisks in **b** and **c**). The diffraction vectors $\boldsymbol{g}_{00l}$ and $\boldsymbol{g}_{h00}$ are indicated by green arrows and $\boldsymbol{b}$ by orange arrows: for in-plane edge dislocations the arrows are horizontal, for out-of-plane screw dislocations the arrows are vertical, and for mixed dislocation the arrows are tilted. The interface film/substrate interface is marked with a yellow dotted line. Scale bar in **d**–**o**, 50 nm.

Discussion

In conclusion, we have systematically investigated the structure-electrical-properties relationship of SRO_{214} thin-films grown on LSAT by pulsed laser deposition from a single crystal SRO_{327} target. The absence of superconductivity in films thinner than 50 nm is correlated with the in-plane misorientation mosaic twist, caused by in-plane screw dislocations, and with the most defective region near the SRO_{214}/LSAT interface. The application of single crystal SRO_{327} targets offers a robust reliable platform for the creation of superconducting SRO_{214} thin-films and will initiate experimental studies involving multilayer structures and devices based on this highly important superconducting oxide.

Methods

Substrate preparation and growth. SRO_{214} films are grown by pulsed laser deposition onto $5 \times 5 \times 0.5\,mm^3$ single crystal (0 0 1) $(LaAlO_3)_{0.3}$-$(Sr_2AlTaO_6)_{0.7}$ (LSAT) with miscut angles of less than 0.05°. Prior to loading into the pulsed laser deposition chamber, the LSAT substrates are ultrasonicated for 10 min in acetone followed by 10 min in isopropyl, and subsequently dried using nitrogen gas. The LSAT substrates are attached to a SiC crystal ($10 \times 10\,mm^2$) with Pt paste (Tanaka Kikinzoku Kogyo K.K.) and secured with clips onto the substrate holder. The LSAT substrates are pre-baked for 30 min at 250°C in vacuum in the load-lock chamber. In the main chamber, the LSAT is annealed in ultra-high vacuum (7.5e-6 Pa) for 30 min at 950°C to promote terrace formation, with a warming ramp rate of 50 °C min^{-1}. The SRO_{214} films are grown in different oxygen pressures and KrF excimer laser (LPXpro 210 F Coherent Inc. 248 nm) energies as discussed in the main paper with the LSAT substrate temperature maintained at 950°C using an infrared diode laser heater. The SRO_{214} films are deposited by ablating from a single crystal target of SRO_{327} at a repetition rate of 2 Hz for the majority of the samples prepared in this work (or 4 Hz for one film) and a substrate to target distance of 5 cm. Following film growth, the sample is cooled in oxygen at a rate of 50°C min^{-1}.

Target preparation. Single crystal targets of SRO_{327} are prepared by floating zone method as discussed in refs. [41,42]. These are cleaved in isopropyl and ultrasonicated for 10 min in acetone and then 10 min in isopropanol and subsequently dried using nitrogen gas. The cleaved crystals have a volume of approximately $3 \times 10 \times 0.5$ mm^3. The surfaces of the crystals are examined by optical microscopy with polarized light to confirm a low concentration of Ru and SRO_{113} surface impurities. The SRO_{327} target is attached to a holder (polycrystalline SRO_{214}) using Epoxy-Ag paste and cured for 30 min at 150°C. Prior to loading it into the pulsed laser deposition main chamber, the SRO_{327} target is baked for 30 min at 250°C in vacuum in the load-lock.

Transport and magnetic measurements. Electrical transport measurements are performed in a pulsed tube cryogen free physical property measurement system. Electrical resistance is measured using a current-bias four-point electrical setup with Au contact pads evaporated onto the SRO_{214} surface.

X-ray diffraction. X-ray diffraction data were acquired using a Panalytical Empyrean X-ray diffractometer, with a Cu_{Ka1} X-ray source and a hybrid two bounce primary monochromator.

Transmission electron microscopy. Samples for transmission electron microscopy are prepared using focused ion beam milling. Bright field transmission electron microscopy imaging for $\boldsymbol{g} \cdot \boldsymbol{b}$ analysis is performed using an FEI Tecnai Osiris at 200 kV. Compositional mapping is carried out using scanning transmission electron microscopy (STEM) – energy dispersed X-ray spectroscopy (EDX) in the same instrument, employing a Super-X detector with a total collection solid angle of 0.9 sr. High resolution STEM images are acquired on a probe-corrected FEI Titan operated at 300 kV.

Data availability

Supporting research data have been deposited in the University of Cambridge research repository and it is publicly available at https://doi.org/10.17863/CAM.48463.

Received: 26 November 2019; Accepted: 26 March 2020;
Published online: 06 May 2020

References

1. Linder, J. & Robinson, J. W. A. Superconducting spintronics. *Nat. Phys.* **11**, 307–315 (2015).
2. Robinson, J. W. A., Witt, J. D. S. & Blamire, M. G. Controlled injection of spin-triplet supercurrents into a strong ferromagnet. *Scienœ.* **329**, 59–61 (2010).
3. Khaire, T. S., Khasawneh, M. A., Pratt, W. P. & Birge, N. O. Observation of spin-triplet superconductivity in co-based josephson junctions. *Phys. Rev. Lett.* **104**, 137002 (2010).
4. Shibuya, K., Mi, S., Jia, C.-L., Meuffels, P. & Dittmann, R. Sr_2TiO_4 layered perovskite thin films grown by pulsed laser deposition. *Appl. Phys. Lett.* **92**, 241918 (2008).
5. Anwar, M. S., Veldhorst, M., Brinkman, A. & Aarts, J. Long range supercurrents in ferromagnetic CrO_2 using a multilayer contact structure. *Appl. Phys. Lett.* **100**, 052602 (2012).
6. Gingrich, E. C. et al. Spin-triplet supercurrent in Co/Ni multilayer Josephson junctions with perpendicular anisotropy. *Phys. Rev. B* **86**, 224506 (2012).
7. Di Bernardo, A. et al. Signature of magnetic-dependent gapless odd frequency states at superconductor/ferromagnet interfaces. *Nat. Commun.* **6**, 8053 (2015).
8. Di Bernardo, A. et al. Intrinsic paramagnetic Meissner effect due to s-wave odd-frequency superconductivity. *Phys. Rev. X* **5**, 041021 (2015).
9. Srivastava, A. et al. Magnetization control and transfer of spin-polarized cooper pairs into a half-metal manganite. *Phys. Rev. Appl.* **8**, 044008 (2017).
10. Jeon, K.-R. et al. Enhanced spin pumping into superconductors provides evidence for superconducting pure spin currents. *Nat. Mater.* **17**, 499–503 (2018).
11. Xu, H. Signatures of majorana fermions in topological superconductor nanowires. in *Extended Abstracts of the 2014 International Conference on Solid State Devices and Materials* (The Japan Society of Applied Physics, 2014).
12. Bommer, J. D. S. et al. Spin-orbit protection of induced superconductivity in majorana nanowires. *Phys. Rev. Lett.* **122**, 187702 (2019).
13. Wei, P., Manna, S., Eich, M., Lee, P. & Moodera, J. Superconductivity in the surface state of noble metal gold and its fermi level tuning by EuS dielectric. *Phys. Rev. Lett.* **122**, 247002 (2019).
14. Maeno, Y. et al. Superconductivity in a layered perovskite without copper. *Nature* **372**, 532–534 (1994).
15. Mackenzie, A. P., Scaffidi, T., Hicks, C. W. & Maeno, Y. Even odder after twenty-three years: the superconducting order parameter puzzle of Sr_2RuO_4. *npj Quantum Mater.* **2**, 40 (2017).
16. Barber, M. E., Gibbs, A. S., Maeno, Y., Mackenzie, A. P. & Hicks, C. W. Resistivity in the vicinity of a van Hove singularity: Sr_2RuO_4 under uniaxial pressure. *Phys. Rev. Lett.* **120**, 76602 (2018).
17. Kallin, C. Chiral p-wave order in Sr_2RuO_4. *Reports Prog. Phys.* **75**, 042501 (2012).
18. Luke, G. M. et al. Time-reversal symmetry breaking superconductivity in Sr_2RuO_4. *Nature* **394**, 558–561 (1998).
19. Xia, J., Maeno, Y., Beyersdorf, P. T., Fejer, M. M. & Kapitulnik, A. High resolution polar Kerr effect measurements of Sr_2RuO_4: evidence for broken

time-reversal symmetry in the superconducting state. *Phys. Rev. Lett.* **97**, 167002 (2006).
20. Ishida, K. et al. Spin-triplet superconductivity in Sr_2RuO_4 identified by ^{17}O Knight Shift. *Nature* **396**, 658–660 (1998).
21. Murakawa, H., Ishida, K., Kitagawa, K., Mao, Z. Q. & Maeno, Y. Measurement of the ^{101}Ru -knight shift of superconducting Sr_2RuO_4 in a parallel magnetic field. *Phys. Rev. Lett.* **93**, 167004 (2004).
22. Duffy, J. A. et al. Polarized-neutron scattering study of the cooper-pair moment in Sr_2RuO_4. *Phys. Rev. Lett.* **85**, 5412–5415 (2000).
23. Pustogow, A. et al. Constraints on the superconducting order parameter in Sr_2RuO_4 from oxygen-17 nuclear magnetic resonance. *Nature* **574**, 72–75 (2019).
24. Schlom, D. & Jia, Y. Searching for superconductivity in epitaxial films of copper-free layered oxides with the K_2NiF_4 structure. *Proc. SPIE* **3481**, 226–240 (1998).
25. Mackenzie, A. P. et al. Extremely strong dependence of superconductivity on disorder in Sr_2RuO_4. *Phys. Rev. Lett.* **80**, 161–164 (1998).
26. Kikugawa, N., Mackenzie, A. P. & Maeno, Y. Effects of in-plane impurity substitution in Sr_2RuO_4. *Phys. Soc. Jpn* **72**, 237–240 (2003).
27. Marshall, P. B., Kim, H., Ahadi, K. & Stemmer, S. Growth of strontium ruthenate films by hybrid molecular beam epitaxy. *APL Mater.* **5**, 096101 (2017).
28. Krockenberger, Y. et al. Growth of superconducting Sr_2RuO_4 thin films. *Appl. Phys. Lett.* **97**, 082502 (2010).
29. Cao, J. et al. Enhanced localized superconductivity in Sr_2RuO_4 thin film by pulsed laser deposition. *Supercond. Sci. Technol.* **29**, 095005 (2016).
30. Uchida, M. et al. Molecular beam epitaxy growth of superconducting Sr_2RuO_4 films. *APL Mater.* **5**, 106108 (2017).
31. Nair, H. P. et al. Demystifying the growth of superconducting Sr_2RuO_4 thin films. *APL Mater.* **6**, 101108 (2018).
32. Ohnishi, T. & Takada, K. Epitaxial thin-film growth of $SrRuO_3$, $Sr_3Ru_2O_7$, and Sr_2RuO_4 from a $SrRuO_3$ target by pulsed laser deposition. *Appl. Phys. Express* **4**, 025501 (2011).
33. Marshall, P. B., Ahadi, K., Kim, H. & Stemmer, S. Electron nematic fluid in a strained $Sr_3Ru_2O_7$ film. *Phys. Rev. B* **97**, 155160 (2018).
34. Ikeda, S.-I., Maeno, Y., Nakatsuji, S., Kosaka, M. & Uwatoko, Y. Ground state in $Sr_3Ru_2O_7$: Fermi liquid close to a ferromagnetic instability. *Phys. Rev. B* **62**, R6089–R6092 (2000).
35. Xia, J., Siemons, W., Koster, G., Beasley, M. R. & Kapitulnik, A. Critical thickness for itinerant ferromagnetism in ultrathin films of $SrRuO_3$. *Phys. Rev. B* **79**, 140407 (2009).
36. Kim, G. et al. Electronic and vibrational signatures of ruthenium vacancies in Sr2RuO4 thin films. *Phys. Rev. Mater.* **3**, 094802 (2019).
37. Moram, M. A. & Vickers, M. E. X-ray diffraction of III-nitrides. *Reports Prog. Phys.* **72**, 036502 (2009).
38. Lee, S. R. et al. Effect of threading dislocations on the Bragg peakwidths of GaN, AlGaN, and AlN heterolayers. *Appl. Phys. Lett.* **86**, 241904 (2005).
39. Williams, D. B. & Carter, C. B. *Transmission electron microscopy: a textbook for materials science*. (Springer, 2009).
40. Massabuau, F. C.-P., Bruckbauer, J., Trager-Cowan, C. & Oliver, R. A. *Characterisation and Control of Defects in Semiconductors*. (The Institution of Engineering and Technology, London, 2019).
41. Perry, R. S. & Maeno, Y. Systematic approach to the growth of high-quality single crystals of $Sr_3Ru_2O_7$. *J. Cryst. Growth* **271**, 134–141 (2004).
42. Maeno, Y. et al. Enhancement of Superconductivity of Sr_2RuO_4 to 3 K by Embedded Metallic Microdomains. *Phys. Rev. Lett.* **81**, 3765 (1998).

Acknowledgements

This work was supported by the EPSRC International Network grant no. EP/N017242/1 with the JSPS Core-to-Core Programme, JSPS KAKENHI Nos. JP15H05852, JP15K21717 and JP17H06136 and by the Institute for Basic Science in Korea grant no. IBS-R009-D1. We are grateful to Shingo Yonezawa for the useful discussion and Takuto Miyoshi and Eunkyo Ko for their contribution in the laboratory.

Author contributions

J.W.A.R. devised the original project and developed it with C.M.P.G. alongside T.W.N., Y.M. C.M.P.G. and J.W.A.R. analysed the data with support from A.D.B., G.K., A.V., Y.M. and T.W.N. Thin-films were fabricated by C.M.P.G. with support from A.D.B., H.G.L., S.K., J.K., B.K. and Y.Y. Electrical and magnetic properties were characterised by C.M.P.G. with the support of A.D.B., S.K. and G.K. Microstructural properties were characterised by X-ray diffraction by C.M.P.G. with support from M.E.V. and input from G.K. Transmission electron microscopy was performed by F.C-P.M and G.D. $Sr_3Ru_2O_7$ crystals were fabricated by Y.M. as well as by R.F. along with A.V. M.G.B. provided input into the growth of the thin films. All authors commented on the paper. C.M.P.G. and J.W.A.R. wrote the manuscript with input from A.D.B., G.K., S.K., M.E.V. and F.C-P.M.

Competing interests

The authors declare no competing interests.

Additional information

Supplementary information is available for this paper at https://doi.org/10.1038/s43246-020-0026-1.

Correspondence and requests for materials should be addressed to J.W.A.R.

Reprints and permission information is available at http://www.nature.com/reprints

Publisher's note Springer Nature remains neutral with regard to jurisdictional claims in published maps and institutional affiliations.

Bibliography

1. Maeno, Y. *et al.* Superconductivity in a layered perovskite without copper. *Nature* **372**, 532–534 (1994).

2. Maeno, Y., Rice, TM., Sigrist, M. The intriguing superconductivity of strontium ruthenate. *Phys. Today* **54**, 42–47 (2001).

3. Maeno, Y., Kittaka, S., Nomura, T., Yonezawa, S. & Ishida, K. Evaluation of Spin-Triplet Superconductivity in Sr_2RuO_4. *J. Phys. Soc. Japan* **81**, 011009 (2012).

4. Liu, Y. & Mao, Z. Unconventional superconductivity in Sr_2RuO_4. *Phys. C Supercond. its Appl.* **514**, 339–353 (2015).

5. Mackenzie, A. P., Scaffidi, T., Hicks, C. W. & Maeno, Y. Even odder after twenty-three years: the superconducting order parameter puzzle of Sr_2RuO_4. *npj Quantum Mater.* **2**, 40 (2017).

6. Mackenzie, A. P. *et al.* Extremely Strong Dependence of Superconductivity on Disorder in Sr_2RuO_4. *Phys. Rev. Lett.* **80**, 161–164 (1998).

7. Mckenzie, R. H. Sr_2RuO_4: an electronic analogue of ^{3}He? *J. Phys. Condens. Matter* **7**, 643–648 (1995).

8. Linder, J. & Robinson, J. W. A. Superconducting spintronics. *Nat. Phys.* **11**, 307–315 (2015).

9. Mao, Z. Q., Mori, Y. & Maeno, Y. Suppression of superconductivity in Sr_2RuO_4 caused by defects. *Phys. Rev. B - Condens. Matter Mater. Phys.* **60**, 610–614 (1999).

10. Nakagawa, R., Nakamura, T., Terashima, T., Yonezawa, S. & Maeno, Y. Superconducting properties of the Pb/Sr_2RuO_4/Pb proximity junction. *Phys. C Supercond. its Appl.* **470**, S744–S745 (2010).

11. Dahl, P. F. Kamerlingh Onnes and the Discovery of Superconductivity. *Istor. Stud. Phys. Sci.* **15**, 1–37 (1984).

12. Alireza, P. L. *et al.* Superconductivity up to 29 K in $SrFe_2As_2$ and $BaFe_2As_2$ at high pressures. *J. Phys. Condens. Matter* **21**, 012208 (2009).

13. Errea, I. *et al.* Quantum Crystal Structure in the 250 K Superconducting Lanthanum Hydride. 1–20 (2019).

14. Somayazulu, M. *et al.* Evidence for Superconductivity above 260 K in Lanthanum Superhydride at Megabar Pressures. *Phys. Rev. Lett.* **122**, 27001 (2019).

15. Ohnishi, T., Shibuya, K., Yamamoto, T. & Lippmaa, M. Defects and transport in complex oxide thin films. *J. Appl. Phys.* **103**, (2008).

16. Annett, J. F. *Superconductivity, Superfluids and Condensates*. (Oxford University Press, 2013).

17. Annett, J. F. Unconventional superconductivity. *Contemp. Phys.* **36**, 423–437 (1995).

18. Berezinskii, V. L. New model of the anisotropic phase of superfluid He3. *JETP Letters* **20**, 287–288 (1974).

19. Mackenzie, A. P. & Maeno, Y. The superconductivity of Sr_2RuO_4 and the physics of spin-triplet pairing. *Rev. Mod. Phys.* **75**, 657–712 (2003).

20. Robinson, J. W. A., Witt, J. D. S. & Blamire, M. G. Controlled Injection of Spin-Triplet Supercurrents into a Strong Ferromagnet. *Science (80-.).* **329**, 59–61 (2010).

21. Bergemann, C., Julian, S. R., Mackenzie, A. P., NishiZaki, S. & Maeno, Y. Detailed Topography of the Fermi Surface of Sr_2RuO_4. *Phys. Rev. Lett.* **84**, 2662–2665 (2000).

22. Kallin, C. Chiral p-wave order in Sr_2RuO_4. *Reports Prog. Phys.* **75**, 042501 (2012).

23. Mao, Z. Q., Maeno, Y. & Fukazawa, H. Crystal growth of Sr_2RuO_4. *Mater. Res. Bull.* **35**, 1813–1824 (2000).

24. Cox, D. E., Goldman, A. I., Subramanian, M. A., Gopalakrishnan, J. & Sleight, A. W. Neutron-powder-diffraction study of the structure and antiferromagnetic ordering in Pr_2CuO_4. *Phys. Rev. B* **40**, 6998–7004 (1989).

25. Ikeda, S.-I., Maeno, Y., Nakatsuji, S., Kosaka, M. & Uwatoko, Y. Ground state in $Sr_3Ru_2O_7$: Fermi liquid close to a ferromagnetic instability. *Phys. Rev. B* **62**, R6089–R6092 (2000).

26. Xia, J., Siemons, W., Koster, G., Beasley, M. R. & Kapitulnik, A. Critical thickness for itinerant ferromagnetism in ultrathin films of $SrRuO_3$. *Phys. Rev. B* **79**, 140407 (2009).

27. Luke, G. M. *et al.* Time-Reversal Symmetry Breaking Superconductivity in Sr_2RuO_4. *Nature* **394**, 558–561 (1998).

28. Xia, J., Maeno, Y., Beyersdorf, P. T., Fejer, M. M. & Kapitulnik, A. High Resolution Polar Kerr Effect Measurements of Sr_2RuO_4: Evidence for Broken Time-Reversal Symmetry in the Superconducting State. *Phys. Rev. Lett.* **97**, 167002 (2006).

29. Nishizaki, S., Maeno, Y., Farner, S., Ikeda, S. & Fujita, T. Pairing symmetry of superconducting Sr_2RuO_4 from specific heat measurements. *Phys. C Supercond. its Appl.* **282–287**, 1413–1414 (1997).

30. Ishida, K. *et al.* Spin-triplet superconductivity in Sr_2RuO_4 identified by ^{17}O Knight Shift. *Nature* **396**, 658–660 (1998).

31. Ishida, K. *et al.* NMR and NQR studies on superconducting Sr_2RuO_4. *J. Phys. Chem. Solids* **69**, 3108–3114 (2008).

32. Duffy, J. A. *et al.* Polarized-Neutron Scattering Study of the Cooper-Pair Moment in Sr_2RuO_4. *Phys. Rev. Lett.* **85**, 5412–5415 (2000).

33. Murakawa, H., Ishida, K., Kitagawa, K., Mao, Z. Q. & Maeno, Y. Measurement of the ^{101}Ru-Knight Shift of Superconducting Sr_2RuO_4 in a Parallel Magnetic Field. *Phys. Rev. Lett.* **93**, 167004 (2004).

34. Pustogow, A. *et al.* Constraints on the superconducting order parameter in Sr_2RuO_4 from oxygen-17 nuclear magnetic resonance. *Nature* **574**, 72–75 (2019).

35. Petsch, A. N. *et al.* Reduction of the spin susceptibility in the superconducting state of Sr_2RuO_4 observed by polarized neutron scattering.

36. Terrade, D., Gentile, P., Cuoco, M. & Manske, D. Proximity effects in a spin-triplet superconductor–ferromagnet heterostucture with a spin-active interface. *Phys. Rev. B* **88**, 054516 (2013).

37. Anwar, M. S. *et al.* triplet superconductivity into a ferromagnet in $Au/SrRuO_3/Sr_2RuO_4$ junctions. *Nat. Commun.* **7**, 13220 (2016).

38. Jin, R. *et al.* Observation of anomalous temperature dependence of the critical current in $Pb/Sr_2RuO_4/Pb$ junctions. *Phys. Rev. B* **59**, 4433–4438 (1999).

39. Sumiyama, A. *et al.* The Josephson effect in contacts between the spin-triplet superconductor Sr_2RuO_4 and conventional superconductors. *Phys. C Supercond. its Appl.* **367**, 129–132 (2002).

40. Saitoh, K. *et al.* High-supercurrent-density contacts and josephson effect of strontium ruthenate. *Appl. Phys. Express* **5**, (2012).

41. Matzdorf, R. *et al.* Ferromagnetism Stabilized by Lattice Distortion at the Surface of the p-Wave Superconductor Sr_2RuO_4. *Science (80-.).* **289**, 746–748 (2000).

42. Schlom, D. & Jia, Y. Searching for superconductivity in epitaxial films of copper-free layered oxides with the K_2NiF_4 structure. *Proc. SPIE* **3481**, 226–240 (1998).

43. Krockenberger, Y. *et al.* Growth of superconducting Sr_2RuO_4 thin films. *Appl. Phys. Lett.* **97**, 082502 (2010).

44. Cao, J. *et al.* Enhanced localized superconductivity in Sr_2RuO_4 thin film by pulsed laser deposition. *Supercond. Sci. Technol.* **29**, 1–6 (2016).

45. Marshall, P. B., Kim, H., Ahadi, K. & Stemmer, S. Growth of strontium ruthenate films by hybrid molecular beam epitaxy. *APL Mater.* **5**, 096101 (2017).

46. Uchida, M. *et al.* Molecular beam epitaxy growth of superconducting Sr_2RuO_4 films. *APL Mater.* **5**, 106108 (2017).

47. Nair, H. P. *et al.* Demystifying the growth of superconducting Sr_2RuO_4 thin films. *APL Mater.* **6**, 101108 (2018).

48. Uchida, M. *et al.* Characterization of Sr_2RuO_4 Josephson junctions made of epitaxial films. *Phys. Rev. B* **101**, 035107 (2020).

49. Lackner, J. M. *et al.* Pulsed laser deposition: a new technique for deposition of amorphous SiO_x thin films. *Surf. Coatings Technol.* **163–164**, 300–305 (2003).

50. Wiley, J. *Pulsed Laser Deposition of Thin Films*. (John Wiley & Sons, Inc., 2006). doi:10.1002/0470052120

51. Phillips, J. M. Substrate selection for high- temperature superconducting thin films. *J. Appl. Phys.* **79**, 1829–1848 (1996).

52. Kidd, P. *XRD of gallium nitride and related compounds: strain, composition and layer thickness*. (Panalytical: Almelo, Netherlands, 2009).

53. Cullity, B.D., Stock, S. R. *Elements of X-Ray Diffraction*. *FEBS Letters* (Pearson, 2014).

54. De, R. R. L., Albuquerque, D. A. C., Cruz, T. G. S., Yamaji, F. M. & Leite, F. L. Measurement of the Nanoscale Roughness by Atomic Force Microscopy: Basic Principles

and Applications. in *Atomic Force Microscopy - Imaging, Measuring and Manipulating Surfaces at the Atomic Scale* (ed. Dr. Victor Bellitto) (InTech, 2012). doi:10.5772/37583

55.: D.B. Williams, and C. B. C. *Transmission electron microscopy: a textbook for materials science*. (Springer, 2009).

56. Egerton, R. F. *Physical Principles of Electron Microscopy. An Introduction to TEM, SEM and AEM*. (Springer, 2005).

57. Design, Q. *Magnetic Property Measurement System, User's Manual*. *Measurement* (2016).

58. C.Mallika, O. M. S. Potentiometric determination of the thermodynamic stability of SrO-RuO_2 system. *J. Alloys Compd.* **191**, 219–222 (1993).

59. Madhavan, S., Schlom, D. G., Dabkowski, A., Dabkowska, H. A. & Liu, Y. Growth of epitaxial a-axis and c-axis oriented Sr_2RuO_4 films. *Appl. Phys. Lett.* **68**, 559–561 (1996).

60. Yoo, Y. Z. *et al.* Contribution of oxygen partial pressures investigated over a wide range to $SrRuO_3$ thin-film properties in laser deposition processing. *J. Appl. Phys.* **97**, (2005).

61. Kim, G. *et al.* Electronic and vibrational signatures of ruthenium vacancies in Sr_2RuO_4 thin films. *Phys. Rev. Mater.* **3**, 094802 (2019).

62. Kikugawa, N., Mackenzie, A. P. & Maeno, Y. Effects of in-plane impurity substitution in Sr_2RuO_4. *J. Phys. Soc. Japan* **72**, 237–240 (2003).

63. Bachelet, R., Ocal, C., Garzn, L., Fontcuberta, J. & Snchez, F. Conducted growth of $SrRuO_3$ nanodot arrays on self-ordered $La_{0.18}Sr_{0.82}Al_{0.59}Ta_{0.41}O_3$(001) surfaces. *Appl. Phys. Lett.* **99**, 2009–2012 (2011).

64. Ichi, S., Azuma, U., Shirakawa, N. & Nishihara, Y. Bulk single-crystal growth of strontium ruthenates by a floating-zone method. **239**, 787–791 (2002).

65. Perry, R. S. & Maeno, Y. Systematic approach to the growth of high-quality single crystals of $Sr_3Ru_2O_7$. *J. Cryst. Growth* **271**, 134–141 (2004).

66. Shibuya, K., Mi, S., Jia, C.-L., Meuffels, P. & Dittmann, R. Sr_2TiO_4 layered perovskite thin films grown by pulsed laser deposition. *Appl. Phys. Lett.* **92**, 241918 (2008).

67. Kwok, H. . *et al.* Correlation between plasma dynamics and thin film properties in pulsed laser deposition. *Appl. Surf. Sci.* **109–110**, 595–600 (1997).

68. Ohnishi, T. & Takada, K. Epitaxial Thin-Film Growth of $SrRuO_3$, $Sr_3Ru_2O_7$, and Sr_2RuO_4 from a $SrRuO_3$ Target by Pulsed Laser Deposition. *Appl. Phys. Express* **4**, 025501 (2011).

69. Klemenz, C. & Scheel, H. J. Flat $YBa_2Cu_3O_{7-x}$ layers for planar tunnel-device technology. *Phys. C Supercond.* **265**, 126–134 (1996).

70. Hawley, M., Raistrick, I. D., Beery, J. G. & Houlton, R. J. Growth Mechanism of Sputtered Films of $YBa_2Cu_3O_7$ Studied by Scanning Tunneling Microscopy. *Science (80-.).* **251**, 1587–1589 (1991).

71. Yamada, H. *et al.* Flux pinning centres correlated along the c-axis in PLD-YBCO films. *Supercond. Sci. Technol.* **17**, 58–64 (2004).

72. Norton, D. P., Lowndes, D. H., Zheng, X.-Y., Zhu, S. & Warmack, R. J. Scanning

tunneling microscopy of pulsed-laser-deposited $YBa_2Cu_3O_{7-\delta}$ epitaxial thin films: Surface microstructure and growth mechanism. *Phys. Rev. B* **44**, 9760–9763 (1991).

73. Pucher, K. *et al.* Transport, magnetic, thermodynamic, and optical properties in Ti-doped Sr_2RuO_4. *Phys. Rev. B* **65**, 104523 (2002).

74. Duijn, H.G.M, van Dijk, N.H, de Visser, A, Franse, J. J. . The influence of Gd and Ni impurities on the superconducting transition temperature of UPt_3. *Phys. B Condens. Matter* **223**–**224**, 44–46 (1996).

75. Maeno, Y. *et al.* Enhancement of Superconductivity of Sr_2RuO_4 to 3 K by Embedded Metallic Microdomains. *Phys. Rev. Lett.* **81**, 3765–3768 (1998).

76. Ying, Y. A. *et al.* Enhanced spin-triplet superconductivity near dislocations in Sr_2RuO_4. *Nat. Commun.* **4**, 2596 (2013).

77. Taniguchi, H., Nishimura, K., Goh, S. K., Yonezawa, S. & Maeno, Y. Higher-Tc Superconducting Phase in Sr_2RuO_4 Induced by In-Plane Uniaxial Pressure. *J. Phys. Soc. Japan* **84**, 014707 (2015).

78. Kittaka, S., Taniguchi, H., Yonezawa, S., Yaguchi, H. & Maeno, Y. Higher-Tc superconducting phase in Sr_2RuO_4 induced by uniaxial pressure. *Phys. Rev. B - Condens. Matter Mater. Phys.* **81**, 4–7 (2010).

79. Hicks, C. W. *et al.* Strong Increase of Tc of Sr2RuO4 Under Both Tensile and Compressive Strain. *Science (80-.).* **344**, 283–285 (2014).

80. Steppke, A. *et al.* Strong peak in Tc of Sr_2RuO_4 under uniaxial pressure. *Science (80-.).* **355**, eaaf9398 (2017).

81. Moram, M. A. & Vickers, M. E. X-ray diffraction of III-nitrides. *Reports Prog. Phys.* **72**, 036502 (2009).

82. Heinke, H., Kirchner, V., Einfeldt, S. & Hommel, D. X-ray diffraction analysis of the defect structure of epitaxial GaN. *Phys. Status Solidi Appl. Res.* **77**, 2145–2147 (2000).

83. Lee, S. R. *et al.* Effect of threading dislocations on the Bragg peakwidths of GaN, AlGaN, and AlN heterolayers. *Appl. Phys. Lett.* **86**, 241904 (2005).

84. Vickers, M. E. *et al.* In-plane imperfections in GaN studied by X-ray diffraction. *J. Phys. D. Appl. Phys.* **38**, A99–A104 (2005).

85. Ermrich Martin; Opper Detlef. *XRD for the Analyst*. (PaNalytical GmbH, 2013).

86. Wilson, A. J. C. Seherrer after Sixty Years: A Survey and Some New Results in the Determination of Crystallite Size. 102–113 (1978).

87. Xu, Z. *et al.* Magnetic, electrical transport, and thermoelectric properties of $Sr_4Ru_3O_{10}$: Evidence for a field-induced electronic phase transition at low temperatures. *Phys. Rev. B - Condens. Matter Mater. Phys.* **76**, 1–6 (2007).